

Superfluidity and Correlations in Systems of Indirect Excitons

DISSERTATION
ZUR ERLANGUNG DES DOKTORGRADES
DER MATHEMATISCH-NATURWISSENSCHAFTLICHEN FAKULTÄT
DER CHRISTIAN-ALBRECHTS-UNIVERSITÄT ZU KIEL
VORGELEGT VON

JENS BÖNING

KIEL, 2011

Referent: Prof. Dr. Michael Bonitz

Koreferent: Priv.-Doz. Dr. Alexei Filinov

Tag der mündlichen Prüfung: Mi, 22. Juni 2011

Zum Druck genehmigt: Mi, 22. Juni 2011

gez. Prof. Dr. Lutz Kipp, Dekan

Abstract

One of the fundamental aspects of electrical conductance in semiconductors is the existence of two types of charge carriers: *Electrons* living in the conduction band, and *holes* which are the gaps the excited electrons leave behind when excited from the valence band to the conduction band. While electrons and holes can recombine and extinguish each other, they may also enter a meta-stable bound state called *exciton*. It is similar to hydrogen, but significantly lighter since the hole's mass is comparable to that of the electron.

Electrons and holes are fermions, so an exciton is a composite boson. As such, the Pauli exclusion principle no longer applies enabling a large number of excitons to populate the same state below a critical temperature. The physics of such Bose-Einstein condensates is fascinating since it promotes the laws of quantum mechanics to macroscopic time and length scales. Condensates were first realized in dilute gases of alkali atoms after cooling methods improved enough to reach the 100 nK-range, but excitonic matter has a much higher critical temperature due to their much lighter mass.

Creating *indirect excitons* from spatially separated electrons and holes boosts their short lifetime by several orders of magnitude. Each indirect exciton features a dipole moment leading to a strong correlation in the many-body system. One of the intriguing consequences of strong correlations is that one may not only achieve condensation but also observe the crystallization of excitons.

This thesis constitutes a numerical investigation of a system composed of indirect excitons in order to explore the requirements for its crystallization among others. The predictions are based on first principle Path Integral Monte Carlo (PIMC) simulations. The main distinction of the present study over previous quantum Monte Carlo studies of similar systems is a more realistic model of the exciton interaction. Due to their composite nature, a simple dipole approximation of the exciton interaction fails if the excitons are too close. At this point, the exciton interaction is dominated by the Coulomb-like repulsion of its components. The derived improved model accounts for this effect and, additionally, incorporates effects encountered in realistic experimental setups. Here, semiconductor

heterostructures are used to create a planar quantum well where an electric field forces the electrons and holes to opposite walls.

It is shown that the resulting effective exciton interaction depends primarily on two parameters: The effective dipole moment and the mass ratio of electrons and holes. The interaction is much softer at small distances than the pure dipole interaction or the classical approximation for the exciton interaction.

The peculiar shape of the interaction makes a crucial difference for the exciton crystallization. The PIMC simulations of this model yield profound evidence for such a phase. Most notably, the phase diagram of indirect excitons exhibits two quantum phase transitions from solid to superfluid confining the solid phase to a finite density interval. At the low-density transition, the system crystallizes by compression. At the second high-density transition, the system melts by compression. The former is in agreement to the behavior of a system of polarized dipoles while the latter is the expected behavior of a Coulomb system. These two quantum transitions are influenced by the strength of the dipole moment. They coincide at a critical dipole moment below which the solid cannot exist. Both superfluid and solid exist only at low temperatures and, in both cases, the transition to a normalfluid gas of excitons is in accordance to existing studies.

Kurzbeschreibung

Hinweis: Diese Arbeit wurde in englisch verfasst. Die Kurzbeschreibung ist eine Übersetzung des englischen Originals von Seite iii

Ein zentraler Aspekt der elektrischen Leitung in Halbleitern ist die Existenz zweier Arten von Ladungsträgern: *Leitungselektronen* und *Löchern* – Fehlstellen im Valenzband, die von den ins Leitungsband angeregten Elektronen zurückgelassen werden. Leitungselektronen und Löcher rekombinieren unter gegenseitiger Vernichtung – sie können aber auch einen metastabilen gebundenen Zustand einnehmen, der als *Exziton* bekannt ist. Es ist vergleichbar mit einem Wasserstoffatom, ist aber wesentlich leichter, da die Masse eines Loches vergleichbar mit der eines Elektrons ist.

Ungebundene Elektronen und Löcher sind Fermionen, als Exziton sind bilden sie ein (zusammengesetztes) Boson. Als solches unterliegt ein Exziton nicht mehr dem Paulischen Ausschlussprinzip – daher ist es einer große Zahl von Exzitonen unterhalb einer kritischen Temperatur möglich den gleichen Zustand zu bevölkern. Die Physik solcher Bose-Einstein-Kondensate ist ein spannendes Gebiet, da es die im Kleinen gültigen quantenmechanischen Gesetze in unserer makroskopischen Welt erlebbar macht. Die ersten Kondensate in verdünnten Gases von Alkali-Atomen konnten experimentell realisiert werden, nachdem man die Kühlmethoden hinreichend verbesserte, um die nötigen Temperaturen im 100 nK-Bereich zu erreichen. Exzitonen hingegen haben eine weitaus höhere kritische Temperatur aufgrund der im Vergleich sehr viel kleineren Masse.

Wenn man *indirekte Exzitonen* aus räumlich getrennten Elektronen und Löchern kreiert, erhöht sich dessen kurze Lebensdauer um mehrere Größenordnungen. Ein indirektes Exziton hat zudem ein Dipolmoment, das zu starken Korrelationen innerhalb des Vielteilchen-Systems führt. Eine faszinierende Konsequenz starker Korrelationen ist, dass es nicht nur die Bose-Einstein-Kondensation, sondern auch die Kristallisation von Exzitonen ermöglicht.

Die vorliegende Dissertation behandelt die numerische Untersuchung eines Systems indirekter Exzitonen mit dem vorrangigen Ziel, die Voraussetzungen für eine Kristallbildung zu erforschen. Die Vorhersagen stützen sich auf *first principle*

Pfadintegral Monte-Carlo (PIMC) Simulationen. Der Hauptunterschied zu älteren Quanten Monte-Carlo Untersuchungen ähnlicher Systeme ist ein realistischeres Modell der Exziton-Exziton Wechselwirkung. Aufgrund der zusammengesetzten Natur eines Exzitons versagt eine simple Dipol-Dipol Näherung auf kurzen Abständen. In diesem Bereich ist die Wechselwirkung von der Coulomb-Abstoßung seiner Komponenten geprägt. Das verbesserte Modell berücksichtigt nicht nur diesen Umstand, sondern involviert Effekte wie sie in einem realistischen Experiment vorliegen. In einem solchen nutzt man Halbleiter-Heterostrukturen zur Erzeugung eines planaren Quantentopfes, bei dem ein zusätzliches elektrisches Feld für die räumliche Trennung von Elektronen und Löchern sorgt.

Es zeigt sich, dass die resultierende effektive Exziton-Exziton Wechselwirkung hauptsächlich von zwei Parametern abhängt, dem Dipolmoment und des Massenverhältnissen von Elektronen und Löchern. Die Wechselwirkung ist viel schwächer auf kurzen Distanzen im Vergleich zur Dipol-Dipol Wechselwirkung oder der klassischen Näherung für die Exziton-Exziton Wechselwirkung.

Die besondere Form der Wechselwirkung ist es auch der entscheidende Faktor bei der Kristallisation von Exzitononen, dessen Existenz durch PIMC Simulationen belegt wird. Eine bemerkenswerte Eigenart des Phasendiagramms ist das Auftreten von zwei isothermalen Übergängen aus der festen in die suprafluide Phase, die die feste Phase in einen beschränkten Dichtebereich einschließen – bei niedrigen Dichten kristallisiert das System bei Kompression, bei hohen Dichten schmilzt es bei Kompression. Ersteres stimmt mit dem Verhalten in System mit Dipol-Dipol Wechselwirkung überein, während das zweite Verhalten von Coulomb Systemen zu erwarten ist. Die genaue Punkt der Phasenübergänge wird vom Dipolmoment beeinflusst. Bei einem kritischen Dipolmoment stimmen beide überein, so dass die feste Phase bei schwächeren Dipolmomenten nicht existiert. Sowohl suprafluide als feste Phase treten nur bei niedrigen Temperaturen auf, der Übergang zu einer normalfluiden Gasphase verhält sich entsprechend bekannter Untersuchungen und Gesetzmäßigkeiten.

Contents

ABSTRACT	iii
KURZBESCHREIBUNG	v
CONTENTS	vii
LIST OF FIGURES	xi
LIST OF TABLES	xiii
1 INTRODUCTION	1
1.1 What is Quantum Coherence?	1
1.2 Why Excitons?	2
1.3 Condensation in Short-Lived Systems	3
1.4 Correlations and Phase Transitions	4
1.5 What is in This Work?	5
1.6 Outline	6
I Theoretical Background	7
2 THE DENSITY MATRIX	9
2.1 Density Matrix in Coordinate Representation	10
2.2 Properties	12
2.2.1 Equation of Motion	12
2.2.2 Bloch Equation	12
2.2.3 Convolution	13
2.3 Exact Density Matrices	13
2.3.1 Free Particles	13
2.3.2 Harmonic Oscillator Potential	14
2.4 Approximations	14

2.4.1	Primitive Approximation	14
2.4.2	Semiclassical Approximation	15
2.4.3	Adiabatic Approximation	15
2.4.4	Expansion	16
3	PHASE TRANSITIONS IN 2D SYSTEMS	19
3.1	Spontaneous Symmetry Breaking	19
3.2	The Importance of Order Parameters	20
3.3	Absence of Long-Range Order	22
3.4	The Kosterlitz-Thouless Transition	23
3.5	Melting	25
II	Methods	27
4	MATRIX SQUARING	29
4.1	Reduction of Complexity	29
4.2	Matrix Squaring	33
4.2.1	Implementation	34
4.3	Beyond Matrix Squaring	36
5	PATH-INTEGRAL MONTE-CARLO	37
5.1	Discrete Imaginary-Time Path-Integrals	37
5.1.1	Notation and Classical Interpretation	38
5.1.2	High-Temperature Approximation	40
5.2	Action	40
5.3	Monte-Carlo Sampling	42
5.3.1	Staging	46
5.3.2	Bisectioning	47
5.3.3	Whole-Chain Displacement	48
5.3.4	Permutation Sampling	49
5.4	Worm-Algorithm	49
5.4.1	Open/Close	52
5.4.2	Insert/Remove	52
5.4.3	Advance/Recede	53
5.4.4	Swap	54
5.5	Estimators	54
III	Indirect Excitons	61
6	MODELING THE INTERACTION OF INDIRECT EXCITONS	63
6.1	Model	63

6.2	The Classical Approximation	67
6.3	The Quantum Well Problem	68
6.3.1	Electron and Hole Density Distributions	69
6.3.2	Estimating the Dipole Moment	73
6.3.3	The Effective in-Plane Interactions	77
6.3.4	Application	80
6.4	The in-Plane Problem	84
6.4.1	The Exciton Density Distribution	85
6.4.2	The Effective Exciton Interaction	86
6.4.3	Application	89
7	CRYSTALLIZATION OF INDIRECT EXCITONS	93
7.1	Model	93
7.2	Simulation Results	96
7.2.1	Normalfluid-Solid Transition	99
7.2.2	Superfluid-Normalfluid Transition	101
7.2.3	Superfluid-Solid Transition	102
7.3	Phase Diagram	103
8	CONCLUSION	107
8.1	An Effective Interaction for Indirect Excitons	107
8.2	Conditions for the Crystallization of Indirect Excitons	108
	APPENDICES	111
A	GENERIC REDUCED UNITS	113
B	DIELECTRIC RESPONSE AND SUSCEPTIBILITY OF THE 2D COULOMB GAS	117
C	NOTES ON THE PAIR DENSITY MATRIX	121
C.1	Inter-Action Derivatives	121
C.2	Sum of States for the Coulomb Potential	122
D	NOTES ON MONTE-CARLO SAMPLING	125
D.1	Asymmetric Kinetic Energy Links	125
D.2	Multilevel Sampling	126
	BIBLIOGRAPHY	129
	LIST OF OWN PUBLICATIONS	141
	Publications in Peer Reviewed Journals and Book Chapters	141
	Selected Contributions to International Conferences	141

Contents

CURRICULUM VITAE	143
DANKSAGUNG	145
SELBSTÄNDIGKEITSERKLÄRUNG	147

List of Figures

1.1	Illustration of indirect excitons	3
3.1	Spin vortices in the XY-model.	24
5.1	Path-Integral visualization of 3 1D-particles	39
5.2	End-point action of the harmonic potential	43
5.3	Path-Integral visualization of a worm	51
6.1	Classical approximation of the indirect exciton interaction	68
6.2	Temperature dependence of the effective out-of-plane trapping potential	70
6.3	Temperature dependence of the out-of-plane density distribution . . .	72
6.4	Out-of-plane density distribution with respect to trapping strength and electric field strength	74
6.5	Dependence of the effective dipole moment on the effective electric field strength	76
6.6	Effective dipole moment in the full parametric space	77
6.7	Density-density correlations for a mass symmetric pair of particles . .	79
6.8	Effective in-plane interactions for a mass symmetric pair of particles .	80
6.9	Dipole moments in a AlGaAs/GaAs quantum well	81
6.10	Effective in-plane interactions in a AlGaAs/GaAs quantum well . . .	83
6.11	Radial in-plane density distributions of the single-exciton	85
6.12	Effective in-plane exciton-exciton interaction	89
6.13	Effective exciton interaction in a ZnSse/ZnSe well	90
6.14	Comparison of the effective exciton potential in ZnSe and GaAs semi- conductors	91
7.1	Effective exciton interaction V_{XX} in a ZnSe quantum well for varying strengths of the dipole moment d	97
7.2	Constant density freezing of indirect excitons	98
7.3	Isothermal freezing and melting of indirect excitons	98
7.4	Translational and bond-order correlation functions for thermal melting	99

7.5	Superfluid fraction across isothermal transitions	102
7.6	Phase diagram of 2D indirect excitons	104
7.7	Critical dipole moment of the exciton crystal	106

List of Tables

3.1	Existence of long-range order in the n -vector model in d dimensions .	22
3.2	Predictions of the KTHNY theory for 2D melting	26
6.1	Parameters for semiconductor quantum wells	92
7.1	Effective electron atomic units	95

Introduction

Ex duobus unum – electron and hole bound into an exciton, shedding their fermionic origins and entering the world of bosons. Quantum coherence of bosonic particles makes the quantum mechanical nature of our world palpable. It promotes the governing laws to macroscopic time- and length scales and, hence, is one of the most sought achievements of experimental and theoretical studies.

1.1 What is Quantum Coherence?

The quantum mechanical representation of an individual particle is a wavefunction whose amplitude and phase depend on the state it describes. While the Pauli principle forbids fermions to occupy the same single-particle state, no such restriction is imposed on bosonic particles [1]. Indeed, Einstein predicted in 1924 [2] that at low temperatures, a finite fraction of a system's bosons would spontaneously populate the same quantum state. In the resulting highly ordered many-body state, now known as *Bose-Einstein condensate (BEC)*, the behavior of the whole system is dictated by the constructively amplified single-particle wavefunction. The possibility to form interference patterns constitutes one of the main tools for an experimental detection of a BEC [3].

Bose-Einstein condensation can be seen as an example of – and typically used synonymously for – a more general concept: the spontaneous emergence of quantum phase coherence [4]. Phase coherence is expressed by wavefunctions coherent over distances much longer than the separation between individual particles and may be quantified by a spatial correlation function. Long-range phase coherence also provides the basis for macroscopic quantum phenomena [5, 6] – among the most spectacular rank: superconductivity, the loss of electrical resistivity [7], and superfluidity, the loss of mechanical friction [8].

Superfluidity was discovered in liquid ^4He in 1938 by two groups simultane-

ously, Kapitza in Moscow [9] and Allen and Misener in Cambridge [10]. Three years later, Lev Landau published a remarkably simple phenomenological explanation which is still used today. In his two-fluid theory, only a part of the system's mass density is superfluid. Bogoliubov later demonstrated that its properties arise from a macroscopically occupied state in a weakly interacting Bose system [11]. Interestingly, the superfluid fraction and the condensate fraction are not identical. A schism resolved by the modern theory linking superfluidity to the phase coherence and while the amplitude of the wavefunction characterizes the condensate density [5, 6].

1.2 Why Excitons?

It took over 70 years until improved cooling techniques allowed the first direct experimental observation of BECs in trapped dilute gases of alkali atoms [12–14]. Since then, observation of BECs in cold trapped gases have been reported for a multitude of elements [15] and extended to dipolar Bose gases [16, 17], BECs in long-lived metastable states [18, 19], optical lattices [20, 21] which can show a wide array of different phases [22], and many others, e.g. [23, 24].

The common denominator for BEC experiments in dilute atomic vapors is their strong demand for very low temperatures, e.g. 170 nK in the case of rubidium atoms [12]. A rule of thumb is that the thermal wavelength of the bosons must be comparable to the typical length scale in the system, i.e. the mean free distance or the size of the system [25]. Since the thermal wavelength depends on the particle mass, the critical temperature scales anti-proportional with the particles' mass.

In the search for high-temperature condensates, much effort has been devoted to finding BECs in systems of solid-state quasiparticles whose mass can be several orders of magnitude lighter than that of atomic matter. A budding candidate can be found in semiconductors which offer two distinct types of charge carriers: *Electrons* living in the conductance band, and *holes* which are the gaps in the conductance band left behind by the excited electrons. Due to their opposite charge, electrons and holes are attracted to one another and may recombine under emission of a photon. However, they may also enter a meta-stable bound state called *exciton*. It is similar to hydrogen, but significantly lighter since the hole's mass is comparable to that of the electron [26].

Electrons and holes are fermions, so an exciton is a composite boson and can, thus, undergo Bose-Einstein condensation. While early claims of exciton BECs in three-dimensional semiconductors [27, 28] left some questions unanswered [29], BECs in two-dimensional systems of electron bilayers in a quantizing magnetic field, e.g. [30, 31], and of indirect excitons [32, 33] were confirmed.

Beyond excitons, condensates of even lighter particles like polaritons which are bound exciton-photon states in microcavities with a mass comparable to pho-

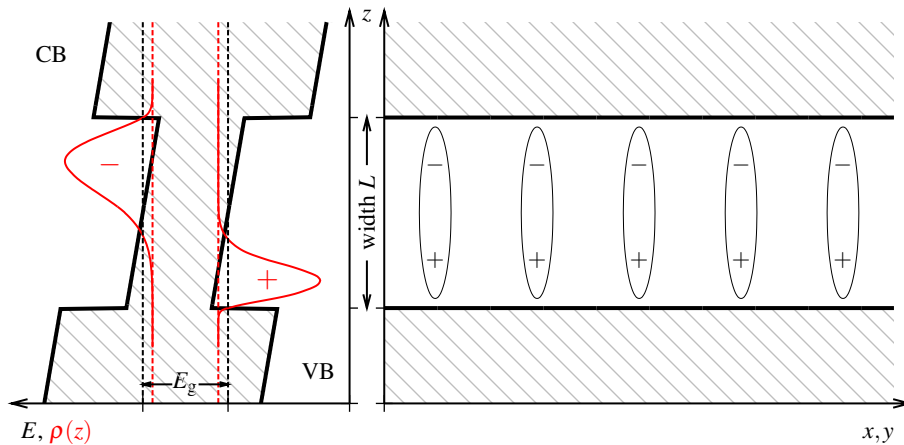


Figure 1.1 Illustration of indirect excitons in a wide quantum well setup. White areas in the left-hand panel are the allowed energy bands labeled “valance band” (VB) and “conductance band” (CB), the shaded area in between is the forbidden band gap. An electric field in z -direction shears the bands and causes a separation of the electron (-) and the hole (+) density distribution (red curves). Bound electron-hole states, the “excitons”, have a lower energy with respect to free electrons and holes and effectively occupy states within the band gap. The right-hand panel illustrates the picture of excitons (ellipses) as polarized dipoles in a 2D plane.

tons, [34–36] and magnons which condensate at room-temperature, [37] have been observed. There are even claims to a BEC of phonons [38], and, very recently, of microcavity photons [39]. Evidence for superfluidity has been found in many of these systems, e.g. for atomic vapors [40, 41], excitons [31], and polaritons [42, 43].

1.3 Condensation in Short-Lived Systems

Quasiparticle condensates provoke some interesting questions regarding their finite lifetime – there is no particle conservation in such systems. Usually, experiments operate in a pumped quasi-equilibrium state [37, 44].

If the bosons live longer than they need to interact, thermalization and, hence, condensation is certainly possible [45–47]. Indeed, atoms in optical traps evaporate or form molecules. They have a finite lifetime, but this does not prevent their condensation. Quasiparticles are lighter and faster, so the timescales are much shorter, but the situation is the same. Indeed, a picosecond lifetime of polaritons seems sufficient to observe condensation [35].

Optically generated excitons exist only for a rather short time which constitutes a major hurdle for their condensation [28, 48]. However, their lifetime

depends on the overlap of electron and hole wavefunction. Spatially separated *indirect excitons* live more than three orders of magnitude longer than direct excitons [49]. Such situations are created in semiconductor heterostructures – a composite of two materials with similar lattice constants where a layer of one type is sandwiched in the other. If the middle layer has a smaller band gap than the surrounding material, it creates a *quantum well* (QW) confining excitons to a two-dimensional plane. An additional electric field perpendicular to the plane forces the excitons' components, electrons and holes, to opposite walls establishing the desired spatial separation [50, 51]. An alternative setup is the creation of two spatially separated quantum wells in appropriately doped semiconductor heterostructures where each QW holds only one particle species [32, 33, 52].

1.4 Correlations and Phase Transitions

Many of the systems in which BECs have been realized, are effectively two-dimensional, e.g. [32, 35, 37, 52] to name a few of the above. Two-dimensional BECs raise issues of their own, since the Mermin-Wagner theorem rigidly rules out true long-range correlations [53, 54]. While the correlation length may not be infinite, however, its asymptotic decay can still change spontaneously. This gives rise to a special class of phase transitions covered by the Berezinskii-Kosterlitz-Thouless scenario [55, 56]. Indeed, spontaneous quantum coherence can occur in two-dimensional systems just as well as in three dimensions which has long been shown in films of liquid helium [57].

Obviously, indirect excitons in bilayer setups constitute a two-dimensional system. In a first approximation, one can expect them to interact like system of parallel dipoles. It is known that in optical lattices, one can create strongly correlated dipolar gases up to the point where the system crystallizes [17]. A key requirement for crystallization is a sufficiently strong interaction which exceeds the kinetic energy by a certain threshold. The ratio of average interaction to average kinetic energy is measured by a *coupling parameter* of which two variants exist for any given particle interaction, typically denoted as (cf. [58], see also Eqs. (7.2) and (7.3))

$$\Gamma = \frac{\langle V \rangle}{\langle T \rangle_{\text{cl}}}, \quad r = \frac{\langle V \rangle}{\langle T \rangle_{\text{qm}}}, \quad (1.1)$$

where $\langle T \rangle_{\text{cl}} \propto k_{\text{B}}T$ is the classical expectation and where $\langle T \rangle_{\text{qm}}$ is the constant (zero-point) quantum mechanical expectation of the kinetic energy. One can show that if the particle interaction scales with an integer power of the particle spacing, i.e., $V(\mathbf{r}) \propto |\mathbf{r}|^n$, there exist *universal* values at which the system crystallizes [58]. For a two-dimensional system with dipole-dipole interaction, the critical values are $\Gamma_{\text{d}}^{\text{cr}} = 62 \pm 4$ [59] and $r_{\text{d}}^{\text{cr}} = 18 \pm 4$ [60–62].

A particularly appealing property is that the dipole moment of indirect excitons can be controlled by tuning the layer separation [33, 50, 51], so the interaction can be made quite strong. Furthermore, one can control the density of the exciton gas with the design of the semiconductor heterostructure [63] or by using an inhomogeneous electric field (Quantum Stark Effect) [50]. The existence of indirect exciton crystals has long been speculated about [64, 65].

1.5 What is in This Work?

Indirect excitons offer a number of attractive features: a strong dipole-type interaction, the suppression of biexciton or trion formation [66, 67], the comparatively long radiative life time [49] and the external controllability of the density and dipole moment [33, 50, 51]. This thesis constitutes a numerical investigation of a system composed of indirect excitons in a setup as illustrated in Fig. 1.1. The aim is to explore the requirements for the exciton crystallization and the onset of spontaneous quantum coherence. The predictions are based on first principle Path Integral Monte Carlo (PIMC) simulations.

There exist quantum Monte Carlo studies which predict crystallization in related model systems such as electron-hole bilayers, e.g. [68, 69], or two-dimensional dipole systems, e.g. [60, 61, 70]. The main distinction of the present study is a more realistic model of the inter-exciton interaction. Due to their composite nature, the dipole approximation of the exciton interaction fails if the excitons are too close. At this point, the exciton interaction is dominated by the Coulomb-like repulsion of its components. The improved model incorporates this effect and, additionally, takes the out-of-plane finite quantum well width and the asymmetric masses of electrons and holes into account.

The resulting interaction is more Coulomb-like and much softer at small distances which makes a crucial difference for the exciton crystallization. The important point is that the quantum dipole coupling parameter and the quantum Coulomb coupling parameter scale contrarily with density – the former decreases when the latter increases [58, 71]. Consequently, the predicted solid phase can only exist in a finite density interval and melts both by relaxation and by compression. This effect is a direct consequence of the peculiar shape of the interaction potential. These two quantum transitions are influenced by the strength of the dipole moment. There exists a critical dipole moment below which the solid cannot exist.

1.6 Outline

Part I. Theoretical background. The key quantity for an investigation of thermodynamic properties is the density matrix. Its definition and properties are laid out in Ch. 2. Also covered are important analytical cases and approximations used in later chapters. Chapter 3 provides a short introduction of the peculiarities of phase transitions in two dimensions. It explains the origin and the universal properties of Kosterlitz-Thouless transitions found in such systems.

Part II. Methods. Numerical methods enter the stage where analytical approximations of the density matrix fail. Two different approaches are presented: The direct computation with the matrix squaring method in Ch. 4 and the powerful Path-Integral Monte-Carlo (PIMC) method in Ch. 5. The former is a valuable tool to compute quasi-exact two-particle density matrices for spherical potentials. PIMC is the main tool to study many-body systems. It combines the path-integral representation of the partition function with Monte-Carlo sampling of the accessible parameter space in a canonical ensemble. The Worm Algorithm which constitutes an extension to the grand-canonical and off-diagonal parameter space, is also presented.

Part III. Indirect Excitons. Chapter 6 discusses the mapping of a bilayer electron-hole system to a two-dimensional excitonic system with an effective interaction. The resulting non-trivial form of the interaction is the origin of the peculiar partition of the excitonic parameter space which is explored with PIMC simulations in Ch. 7. Here, the central result of this thesis is presented: The full phase-diagram and the limiting critical parameters of an exciton solid.

PART I

Theoretical Background

The Density Matrix

A quantum many-body state which can be described by single ket-vector ($| \rangle$) is called a *pure state*. While the Schrödinger equation of the corresponding many-body system determines the possible pure states the system can occupy (and their evolution with time), one needs additional boundary or initial conditions to select a particular state. Otherwise the state is unknown and cannot be represented by single ket-vector. One can, however, use statistical means to describe such a *mixed state*.

The concept of statistical mixture of pure states is provided by a *statistical ensemble*. The ensemble consists of a large (up to infinitely many) number of mental copies of the system in question, each of which represents a possible state the system might be in. In such an ensemble, the mixed state is described by the *density operator* which reads

$$\hat{\rho} = \sum_j p_j |j\rangle \langle j| , \quad (2.1)$$

where the coefficients p_j are non-negative and add up to one. Each p_j determines the fraction of the ensemble being in the pure state $|j\rangle$. If the system were in a *pure ensemble*, all p_j save one would be zero and the system again is described by a pure state. An example is the system at absolute zero where the sole surviving state is the (many-body) ground state (if non-degenerate).

At finite temperatures, one needs additional input how each pure state contributes to the mixed state, i.e. how to define the p_j . In a *canonical ensemble* – with fixed particle number N , volume V , and temperature T – and in thermal equilibrium, the probability to find the ensemble in state $|j\rangle$ is given by the *Boltzmann factor* $e^{-\beta E_j}/Z$, where $\beta = 1/k_B T$ is the inverse temperature and Z is the partition function. Naturally, it is assumed that $|j\rangle$ is an eigenfunction of \hat{H} , i.e. $\hat{H}|j\rangle = E_j|j\rangle$ and E_j is the corresponding energy eigenvalue. The density operator $\hat{\rho}$ then takes a similar expression as the distribution of states $P(E)$ for

classical systems,

$$P(E) = \frac{1}{Z} e^{-\beta E}, \quad \hat{\rho} = \frac{1}{Z} \sum_j e^{-\beta E_j} |j\rangle \langle j| = \frac{1}{Z} e^{-\beta \hat{H}}, \quad (2.2)$$

where the partition function is

$$Z = \sum_j e^{-\beta E_j}. \quad (2.3)$$

With Eq. (2.2), the *equilibrium expectation* of an operator \hat{A} is simply

$$\langle \hat{A} \rangle = \frac{1}{Z} \sum_j \langle j | \hat{A} | j \rangle e^{-\beta E_j}. \quad (2.4)$$

In operator notation, the last two expressions can be written more simply as

$$\langle \hat{A} \rangle = \frac{1}{Z} \text{Tr}(\hat{\rho} \hat{A}), \quad Z = \text{Tr} \hat{\rho}, \quad (2.5)$$

where “Tr” denotes the trace and the *unnormalized density operator* is introduced as

$$\hat{\rho} = e^{-\beta \hat{H}}. \quad (2.6)$$

By *density operator* one commonly refers to the definition (2.6) which is *not* normalized by the partition function. Unless explicitly mentioned, this work follows this convention.

2.1 Density Matrix in Coordinate Representation

In Eq. (2.2), the trace over states may be evaluated in any basis. Doing so in energy eigenfunctions leads back to Eqs. (2.3) and (2.4). This work however, almost exclusively uses a *coordinate basis* where all particles are labeled. The coordinate representation of the density operator is called *density matrix* and reads

$$\rho(R, R'; \beta) = \langle R | \hat{\rho} | R' \rangle = \sum_j \phi_j^*(R) \phi_j(R') e^{-\beta E_j}, \quad (2.7)$$

with $R = \{\mathbf{r}_1, \dots, \mathbf{r}_N\}$ where \mathbf{r}_j denotes the position of the j^{th} particle. If space has dimension d , then R is a dN -dimensional vector and the density matrix $\rho(R, R'; \beta)$ is a function of $2dN + 1$ variables.

The main reason for choosing this basis is that all elements of the density matrix are non-negative and can be interpreted as a probability. In particular, the diagonal element $\rho(R, R; \beta)$ determines the conjoint probability of each particle j

being at position \mathbf{r}_j . The transition probability from R to R' is given by the off-diagonal element $\rho(R, R'; \beta)$.

Inserting Eq. (2.7) in Eq. (2.5), the canonical expectation of \hat{A} becomes

$$\langle \hat{A} \rangle = \frac{1}{Z} \int dR dR' \rho(R, R'; \beta) \langle R' | \hat{A} | R \rangle , \quad (2.8)$$

and the partition function is given by

$$Z = \int dR \rho(R, R; \beta) . \quad (2.9)$$

If \hat{A} is diagonal in coordinate representation, i.e. $\langle R | \hat{A} | R' \rangle = A(R) \delta(R - R')$, then Eq. (2.8) simplifies to

$$\langle \hat{A} \rangle = \frac{1}{Z} \int dR \rho(R, R; \beta) A(R) . \quad (2.10)$$

Labeling particles implies that they can be distinguished which is *not* the case. When writing the density matrix in coordinate representation, the indistinguishability of particles must be taken into account explicitly. Depending on the particle nature, only totally symmetric eigenfunctions $\phi_j^S(R)$ (Bosons) or totally antisymmetric eigenfunctions $\phi_j^A(R)$ (Fermions) contribute to the density matrix, respectively. Totally (anti)-symmetric eigenfunctions obey

$$\phi_j^S(PR) = \phi_j^S(R) , \quad \phi_j^A(PR) = \text{sgn}(P) \phi_j^A(R) , \quad (2.11)$$

where P is a permutation of particle labels, i.e. $PR = \{\mathbf{r}_{P_1}, \dots, \mathbf{r}_{P_N}\}$, and $\text{sgn}(P)$ the *parity* of the permutation. The parity $\text{sgn}(P)$ is positive (negative) if the N -particle permutation can be decomposed into an even (odd) number of pair permutations. If the Hamiltonian is symmetric under particle exchange, all states are either even or odd with respect to a given permutation. Then, the (*anti*)-symmetrization operator $\hat{P}_{S/A}$

$$\hat{P}_S \phi(R) = \frac{1}{N!} \sum_{P \in S_N} \phi(PR) , \quad \hat{P}_A \phi(R) = \frac{1}{N!} \sum_{P \in S_N} \text{sgn}(P) \phi(PR) , \quad (2.12)$$

where the sum is taken over all possible N -particle permutations S_N , will project out Bose (Fermi) states. Applying Eq. (2.12) to the density matrix of distinguishable particles $\rho(R, R'; \beta)$ [Eq. (2.7)] yields [72]

$$\rho_S(R, R'; \beta) = \frac{1}{N!} \sum_{P \in S_N} \rho(R, PR'; \beta) , \quad (2.13)$$

$$\rho_A(R, R'; \beta) = \frac{1}{N!} \sum_{P \in S_N} \text{sgn}(P) \rho(R, PR'; \beta) , \quad (2.14)$$

where $\rho_S(R, R'; \beta)$ is the bosonic density matrix and $\rho_A(R, R'; \beta)$ is the fermionic density matrix. Note that one can apply the permutation to the first argument of ρ , the last argument, or both without changing the result.

The canonical expectation of \hat{A} becomes, in a bosonic system,

$$\langle \hat{A} \rangle_S = \frac{1}{Z_S} \frac{1}{N!} \sum_{P \in S_N} \int dR dR' \rho(R, PR'; \beta) \langle R | \hat{A} | R' \rangle , \quad (2.15)$$

$$Z_S = \frac{1}{N!} \sum_{P \in S_N} \int dR \rho(R, PR; \beta) , \quad (2.16)$$

and in a fermionic system,

$$\langle \hat{A} \rangle_A = \frac{1}{Z_A} \frac{1}{N!} \sum_{P \in S_N} \int dR dR' \text{sgn}(P) \rho(R, PR'; \beta) \langle R | \hat{A} | R' \rangle , \quad (2.17)$$

$$Z_A = \frac{1}{N!} \sum_{P \in S_N} \int dR \text{sgn}(P) \rho(R, PR; \beta) . \quad (2.18)$$

If \hat{A} is diagonal in coordinate representation, the integration over R' drops out as in Eq. (2.10), but the expectation $\langle \hat{A} \rangle$ still depends on off-diagonal elements of the density matrix. Then, however, only on those elements which correspond to the transition probabilities of permuting particles.

2.2 Properties

2.2.1 Equation of Motion

The equation of motion for the density operator $\hat{\varrho}$ is called *von Neumann equation* and reads (see e.g. [73])

$$i\hbar \frac{\partial \hat{\varrho}}{\partial t} = [\hat{H}, \hat{\varrho}] . \quad (2.19)$$

It describes how $\hat{\varrho}$ evolves in time, just as the Schrödinger equation does for pure states. Both formalisms are equivalent.

2.2.2 Bloch Equation

The density operator $\hat{\rho}$ satisfies the *Bloch equation* (see e.g. [72, 73])

$$-\frac{\partial \hat{\rho}}{\partial \beta} = \hat{H} \hat{\rho} , \quad \hat{\rho}_0 = 1 , \quad (2.20)$$

which is a linear partial differential equation of 2nd order with the given initial condition. Its validity can easily be proven choosing any representation of the

density operator – a convenient choice is the energy representation where $\hat{\rho}$ is diagonal.

For the density matrix $\rho(R, R'; \beta)$, the Bloch equation (2.20) becomes

$$-\frac{\partial}{\partial \beta} \rho(R, R'; \beta) = \hat{H}_R \rho(R, R'; \beta), \quad \rho(R, R'; 0) = \delta(R - R'), \quad (2.21)$$

where the subscript R on \hat{H}_R indicates that \hat{H}_R operates on R in $\rho(R, R'; \beta)$. An alternative choice of R' is equally valid due to the symmetry of the density matrix $\rho(R, R'; \beta) = \rho(R', R; \beta)$.

2.2.3 Convolution

By its very definition, the density operator has the following simple group property: The product of two density operators is a density operator, i.e.

$$e^{-(\beta_1 + \beta_2)\hat{H}} = e^{-\beta_1\hat{H}} e^{-\beta_2\hat{H}}. \quad (2.22)$$

Equation (2.23) takes the form of a *convolution* for the density matrix

$$\rho(R, R'; \beta_1 + \beta_2) = \int dR'' \rho(R, R''; \beta_1) \rho(R'', R'; \beta_2). \quad (2.23)$$

2.3 Exact Density Matrices

In general, an explicit analytical expression for the full N -particle density matrix is unknown. But there are two notable exceptions: The free particle density matrix $\rho_0(R, R'; \beta)$ and the density matrix for system of harmonically trapped particles $\rho^{\text{harm}}(R, R'; \beta)$.

2.3.1 Free Particles

The Hamiltonian for a system of N non-interacting particles \hat{H}^{free} can be written as a sum of single-particle Hamiltonians, i.e.

$$\hat{H}^{\text{free}} = - \sum_{j=1}^N \lambda \nabla_{\mathbf{r}_j}^2, \quad (2.24)$$

With the product ansatz

$$\rho_0(R, R'; \beta) = \prod_{j=1}^N \rho_0(\mathbf{r}_j, \mathbf{r}'_j; \beta), \quad (2.25)$$

the Bloch equation (2.21) for \hat{H}^{free} separates into N differential equations of the form

$$\frac{\partial}{\partial \beta} \rho_0(\mathbf{r}, \mathbf{r}'; \beta) = \lambda \nabla_{\mathbf{r}}^2 \rho_0(\mathbf{r}, \mathbf{r}'; \beta), \quad \rho_0(\mathbf{r}, \mathbf{r}'; 0) = \delta(\mathbf{r} - \mathbf{r}'), \quad (2.26)$$

which is a parabolic partial differential equation, also known as *heat equation* or *diffusion equation* with a diffusion constant λ . Its fundamental solution is given by

$$\rho_0(\mathbf{r}, \mathbf{r}'; \beta) = \mathcal{G}_d(\mathbf{r} - \mathbf{r}'; \sqrt{2\lambda\beta}) = (4\pi\lambda\beta)^{-d/2} \exp\left[-\frac{1}{4\lambda\beta} |\mathbf{r} - \mathbf{r}'|^2\right]. \quad (2.27)$$

A normalized Gaussian converges to the Dirac- δ distribution when taking to the limit $\beta \rightarrow 0$. Hence, $\rho_0(\mathbf{r}, \mathbf{r}'; \beta)$ already satisfies the initial condition of the Bloch equation, $\lim_{\beta \rightarrow 0} \rho(\mathbf{r}, \mathbf{r}'; \beta) = \delta(\mathbf{r} - \mathbf{r}')$. Insertion of Eq. (2.27) into Eq. (2.25) yields the full N -particle density matrix.

2.3.2 Harmonic Oscillator Potential

The density matrix of the harmonic oscillator potential is known exactly [72]. It reads for a single particle

$$\rho^{\text{harm}}(\mathbf{r}, \mathbf{r}'; \beta) = (2\pi l_0^2 \sinh(2f))^{-d/2} \exp\left[-\frac{(\mathbf{r} + \mathbf{r}')^2}{4l_0^2 \coth f} - \frac{(\mathbf{r} - \mathbf{r}')^2}{4l_0^2 \tanh f}\right], \quad (2.28)$$

with $f = \lambda\beta/l_0^2$ and the harmonic oscillator length $l_0 = \sqrt{\hbar/(m\omega)}$. The many-body density matrix simply factorizes into a product of (2.28).

2.4 Approximations

2.4.1 Primitive Approximation

Consider the Baker-Campbell-Hausdorff operator identity (See, e.g., [74])

$$e^{-\beta(\hat{A}+\hat{B})+\frac{\beta^2}{2}[\hat{A},\hat{B}]} = e^{-\beta\hat{A}} e^{-\beta\hat{B}}, \quad (2.29)$$

which is exact if $[\hat{A}, [\hat{A}, \hat{B}]] = 0$, or otherwise neglects contributions of order $\mathcal{O}(\beta^3)$. As the commutator term on the left-hand side contributes with β^2 , it becomes smaller than all other terms in the limit $\beta \rightarrow 0$. If one identifies β with the (inverse) temperature, the commutator term of the identity can be neglected in the high temperature limit. Applied to the Hamiltonian, $\hat{H} = \hat{T} + \hat{V}$, where \hat{T} is

the kinetic operator and \hat{V} is the potential operator, this is known as the *primitive approximation*,

$$e^{-\beta(\hat{T}+\hat{V})} \approx e^{-\beta\hat{T}} e^{-\beta\hat{V}} . \quad (2.30)$$

Hence, one can approximate the exact density operator by the product of the density matrices for \hat{T} and \hat{V} alone.

In coordinate representation, the matrix elements for the potential operator are diagonal. Its density matrix, written in a symmetric form, reads

$$\langle R|e^{-\beta\hat{V}}|R'\rangle = \exp\left[-\frac{\beta}{2}(V(R) + V(R'))\right] \delta(R - R') . \quad (2.31)$$

The density matrix for the kinetic operator \hat{T} is the free particle density matrix $\rho_0(R, R'; \beta)$ [Eqs. (2.25)]. Hence, the full N -particle density matrix in primitive approximation is given by

$$\rho^{\text{prim}}(R, R'; \beta) = (4\pi\lambda\beta)^{-dN/2} \exp\left[-\frac{1}{4\lambda\beta}|R - R'|^2 - \frac{\beta}{2}(V(R) + V(R'))\right] , \quad (2.32)$$

or, when using the definition of the free particle density matrix [Eq. (2.27)]

$$\rho^{\text{prim}}(R, R'; \beta) = \rho_0(R, R'; \beta) \exp\left[-\frac{\beta}{2}(V(R) + V(R'))\right] . \quad (2.33)$$

2.4.2 Semiclassical Approximation

One can find an improved approximation of the density matrix with the standard WKB method [75]. The resulting *semiclassical approximation* is given by

$$\rho^{\text{semi}}(R, R'; \beta) = \rho_0(R, R'; \beta) \prod_{j=1}^N \exp\left[-\frac{\beta}{|\mathbf{r}_j - \mathbf{r}'_j|} \int_{\mathbf{r}_j}^{\mathbf{r}'_j} d\mathbf{r}'' V(\mathbf{r}'')\right] . \quad (2.34)$$

On the diagonal, the semiclassical approximation recovers the primitive approximation.

2.4.3 Adiabatic Approximation

In the *adiabatic approximation* it is assumed that the density matrix may be separated into two or more factors. In contrast to the exact methods discussed in Sec. 2.3, where the Hamiltonian may be reduced exactly by such a separation, here a small remainder is neglected.

Suppose that the full coordinate vector R is separated into two sets, s_1 and s_2 . Then, the Hamiltonian can be written in terms of each with an additional coupling term, i.e.

$$\begin{aligned}\hat{H} &= \hat{H}_1 + \hat{H}_2 + \hat{W}_{12} \\ &= T_1(s_1) + V_1(s_1) + T_2(s_2) + V_2(s_2) + W_{12}(s_1, s_2) .\end{aligned}\quad (2.35)$$

If the dynamics of the sub-system H_1 take place on a much slower time scale than that of H_2 , one may attempt to factorize the density matrix into a “slow” and a “fast” contribution using the ansatz

$$\rho^{\text{adiabatic}}(s_1, s_2, s'_1, s'_2; \beta) = \rho^{\text{slow}}(s_1, s'_1; \beta) \rho^{\text{fast}}(s_2, s'_2; \beta) ,\quad (2.36)$$

which yields upon insertion into the Bloch equation

$$\begin{aligned}\rho^{\text{fast}}(s_2, s'_2; \beta) \left[\frac{\partial}{\partial \beta} + T_1(s_1) + V_1(s_1) \right] \rho^{\text{slow}}(s_1, s'_1; \beta) \\ + \rho^{\text{slow}}(s_1, s'_1; \beta) \left[\frac{\partial}{\partial \beta} + T_2(s_2) + V_2(s_2) \right] \rho^{\text{fast}}(s_2, s'_2; \beta) \\ = W_{12}(s_1, s_2) \rho^{\text{slow}}(s_1, s'_1; \beta) \rho^{\text{fast}}(s_2, s'_2; \beta) .\end{aligned}\quad (2.37)$$

Due to the interaction between fast and slow coordinates, the right-hand side is non-zero and the problem does not separate exactly. However, if one assumes that the system *adiabatically* adapts to any change of $\rho^{\text{fast}}(s_2, s'_2; \beta)$, one can solve the Bloch equation for \hat{H}_2 individually. Inserting this solution back into the equation above cancels the second term and leaves the averaged Bloch equation

$$-\frac{\partial}{\partial \beta} \rho^{\text{slow}}(s_1, s'_1; \beta) = \left[\hat{H}_1 + \hat{W}_1 \right] \rho^{\text{slow}}(s_1, s'_1; \beta) ,\quad (2.38)$$

where the fast contributions are absorbed into the smoothed potential

$$W_1(s_1) = \frac{\int ds_2 ds'_2 W_{12}(s_1, s_2) \rho^{\text{fast}}(s_2, s'_2; \beta)}{\int ds_2 ds'_2 \rho^{\text{fast}}(s_2, s'_2; \beta)} .\quad (2.39)$$

In other words, the slow sub-system does not interact explicitly with the fast sub-system but with the a mean field generated by the latter.

2.4.4 Expansion

Explicit analytical expressions for the N -body density matrix $\rho(R, R'; \beta)$ only exist for non-interacting systems where the density matrix factorizes into single particle contributions [cf. Sec. 2.3]. For other systems, one could still attempt such a factorization obtaining the approximation

$$\rho^{(N)}(R, R'; \beta) \approx \left[\prod_{i=1}^N \rho^{(1)}(\mathbf{r}_i, \mathbf{r}'_i; \beta) \right] .\quad (2.40)$$

This density matrix does not take any two-body contributions into account and, thus, fails at the description of interacting systems. A better approximation would try to include two-body contributions, i.e.

$$\rho^{(N)}(R, R'; \beta) \approx \left[\prod_{i=1}^N \rho^{(1)}(\mathbf{r}_i, \mathbf{r}'_i; \beta) \right] \times \left[\prod_{i < j}^N \frac{\rho^{(2)}(\mathbf{r}_i, \mathbf{r}_j, \mathbf{r}'_i, \mathbf{r}'_j; \beta)}{\rho^{(1)}(\mathbf{r}_i, \mathbf{r}'_i; \beta) \rho^{(1)}(\mathbf{r}_j, \mathbf{r}'_j; \beta)} \right] \quad (2.41)$$

One can easily check that this construction is exact for any pair of particles by setting $N = 2$.

Equation (2.41) yields accurate results for thermal expectation values if the interaction is dominated by two-particle collisions. This assumption fails at low temperatures, but is certainly valid at sufficiently high temperatures. Even here, the quality of $\rho^{(N)}(R, R'; \beta)$ depends on the accuracy of the pair density matrix $\rho^{(2)}(\mathbf{r}_1, \mathbf{r}_2, \mathbf{r}'_1, \mathbf{r}'_2; \beta)$.

Phase Transitions in 2D Systems

This chapter discusses the peculiarities of phase transitions in two-dimensional systems. It is by no means comprehensive, but aims to highlight the differences to phase transitions in 3D.

3.1 Spontaneous Symmetry Breaking

The concept of symmetry breaking is inherently tied to phase transitions. For example (see [54]): Crystals, by their very lattice structure, break the translational symmetry encountered in fluids. Ferromagnets are not invariant under rotations in spin space. Less obvious types of symmetry breaking occur in other quantum systems, such as superfluids and superconductors, where a breaking of gauge invariance occurs.

For systems in thermodynamic equilibrium, the expectation of an operator \hat{A} is given by its trace when weighted by the density operator $\hat{\rho} = \exp(-\beta\mathcal{H})$, where – using the grand-canonical ensemble – $\mathcal{H} \equiv \hat{H} - \mu\hat{N}$ is the (grand-canonical) Hamiltonian. Taken to the thermodynamic limit \lim_{th} , i.e. the limit for $V \rightarrow \infty$ and $N \rightarrow \infty$ with N/V constant, one must formally calculate

$$\langle \hat{A} \rangle \equiv \lim_{\text{th}} \text{Tr}(\hat{\rho}\hat{A}) = \lim_{\text{th}} \text{Tr} \left(e^{-\beta\mathcal{H}} \hat{A} \right) . \quad (3.1)$$

The occurrence of a phase transition in the system is related to the failure of one of the phases to exhibit a certain symmetry property of the underlying Hamiltonian \mathcal{H} : If \mathcal{H} displays a continuous symmetry \mathcal{S} it commutes with the generators $\Gamma_i^{\mathcal{S}}$ of the corresponding symmetry group, i.e.

$$[\mathcal{H}, \Gamma_i^{\mathcal{S}}]_- = 0 . \quad (3.2)$$

Now, even if some operator \hat{B} is not invariant under the transformations of \mathcal{S} , the thermal average of the commutator vanishes,

$$[\hat{B}, \Gamma_i^{\mathcal{S}}]_- \neq 0, \quad \langle [\hat{B}, \Gamma_i^{\mathcal{S}}]_- \rangle = 0, \quad (3.3)$$

which can be readily shown with (3.1) using the cyclic invariance of the trace.

However, it turns out that under certain conditions such averages may be unstable with respect to an infinitesimal perturbation $\lambda \hat{H}'$ of the Hamiltonian. To this end, Bogoliubov has devised a method in terms of *quasi-averages* defined as [76]

$$\langle \hat{A} \rangle_{\text{q}} \equiv \lim_{\lambda \rightarrow 0^+} \lim_{\text{th}} \text{Tr} \left(e^{-\beta \mathcal{H}_\lambda} \hat{A} \right), \quad \mathcal{H}_\lambda \equiv \hat{H} + \lambda \hat{H}' - \mu \hat{N}. \quad (3.4)$$

In those instances where the perturbative part \hat{H}' does not commute with \mathcal{S} , the quasi-average does not vanish,

$$\langle [\hat{B}, \Gamma_i^{\mathcal{S}}]_- \rangle_{\text{q}} = \lim_{\lambda \rightarrow 0^+} \text{Tr} \left(e^{-\beta \mathcal{H}_\lambda} [\hat{B}, \Gamma_i^{\mathcal{S}}]_- \right) \neq 0. \quad (3.5)$$

Obviously, the outcome depends on the nature of the perturbation. Physically, the degeneracy imposed on the system by the underlying symmetry is lifted by an external perturbation. The symmetry is *spontaneously broken* if infinitesimal perturbations are sufficient. This can be shown by non-vanishing quasi-averages for cases with continuous symmetry.

3.2 The Importance of Order Parameters

In the theory of phase transitions, one can identify a quantity Φ of the system in question whose thermal (quasi-)average vanishes on one side of the transition, but has a finite value on the other side, i.e.,

$$\langle \Phi \rangle_{\text{q}} = 0, \quad \text{for } T > T_{\text{cr}}, \quad (3.6)$$

$$\langle \Phi \rangle_{\text{q}} \neq 0, \quad \text{for } T < T_{\text{cr}}. \quad (3.7)$$

Such a quantity is called *order parameter*. Φ can be defined in microscopic terms from a *local order parameter* ϕ , i.e. as $\Phi \propto \sum_i \phi_i$ in a many-body system or as $\Phi \propto \int d^d \mathbf{r} \phi(\mathbf{r})$ in a continuum model. The occurrence of phase transitions can be understood from long-range correlations of the local order. The essential quantity to investigate is the *correlation function* g defined as thermal average of local order correlations, i.e.,

$$g_{ij} = \langle \phi_i \phi_j \rangle, \quad g(\mathbf{r}, \mathbf{r}') = \langle \phi(\mathbf{r}) \phi(\mathbf{r}') \rangle, \quad (3.8)$$

respectively. A non-vanishing Φ implies the existence of *long-range order*, i.e.

$$\lim_{|i-j| \rightarrow \infty} g_{ij} \neq 0, \quad \lim_{|\mathbf{r}-\mathbf{r}'| \rightarrow \infty} g(\mathbf{r}, \mathbf{r}') \neq 0. \quad (3.9)$$

In the disordered phase, the order correlations decay exponentially.

Second order phase transitions are continuous and the order parameter is zero at the critical point T_{cr} . Hence, one can try to expand the free energy in terms of the (local) order parameter in vicinity of T_{cr} . This is the main idea of the standard Ginzburg-Landau ansatz which describes fluctuation of the equilibrium order, i.e.,

$$\mathcal{F}(T, V_0, \phi) \approx F_0(T) + \int d^d \mathbf{r} A(\nabla \phi)^2 + a(T - T_{\text{cr}})\phi^2 + u\phi^4 - V_0\phi, \quad (3.10)$$

with the expansion coefficients A , a and u which depend on the underlying system, the external field V_0 coupling to the order parameter, the equilibrium free energy $F(T, V_0) = \mathcal{F}(T, V_0, \Phi(T, V_0))$ and $F_0(T) \equiv F(T, 0)$.

The driving mechanism for a transition is the spatial divergence of local perturbations. When the critical point is approached from the high-temperature disordered phase, isolated ordered domains grow until they encompass the whole system. Coming from the other phase, diverging fluctuations around the equilibrium order eventually dominate and destroy the order. Near the critical point, the system's physics are governed by long-range correlations of either perturbations. This *critical behavior* is characterized by the *correlation length* ξ , i.e., the decay constant of the correlation function (3.8). A related quantity is the *susceptibility* χ , i.e. the response of the (local) order parameter to an external field, $\phi = \chi V_0$. At the critical point, an infinitesimal field V_0 is sufficient to cause a large scale change of the order. In other words, the susceptibility diverges, $\chi \rightarrow \infty$.

An intriguing consequence of critical behavior is its independence of the actual – typically short-range – particle interactions: The expansion (3.10) emphasizes similarities of phase transitions which actually appear in very different systems. Because of these similarities, the essential properties of a phase transition like the singularity type of the susceptibility χ or the correlation length ξ , solely depend on the system dimensionality d and the degrees of freedom n of the order parameter. Systems with the same d and n fall into the same *universality class*. For example, the macroscopic wave-function of a Bose gas is complex and, thus, has two independent components ($n = 2$). A typical $n = 3$ case is the magnetization of ferromagnets.

3.3 Absence of Long-Range Order

Bogoliubov is noted for having established a rigorous relation between two operators \hat{A} and \hat{B} and the Hamiltonian \hat{H} of a physical system [11, 77]:

$$|\langle [\hat{B}, \hat{A}]_- \rangle|^2 \leq \frac{\beta}{2} \langle [\hat{A}, \hat{A}^\dagger]_+ \rangle \langle [\hat{B}^\dagger, [\hat{H}, \hat{B}]_-]_- \rangle, \quad (3.11)$$

where $\beta = 1/(k_B T)$ is the inverse temperature and $\langle \cdot \rangle$ denotes thermal averaging as defined in (3.1) or (3.4), respectively. The inequality is a quite strong statement, as it holds for essentially arbitrary \hat{A} and \hat{B} .

The Bogoliubov inequality (3.11) can serve to *exclude* phase transitions depending on the nature of the system's Hamiltonian. The general idea can be traced to Hohenberg [78], but notably Mermin and Wagner are credited for establishing a method for a rigorous proof [53]. The paradigmatic procedure can be outlined as follows: The general idea is to use the Bogoliubov inequality (3.11) to find an upper bound f for the order parameter Φ in question:

$$\Phi \leq f(V_0, \Phi). \quad (3.12)$$

The bound will normally depend on the external field V_0 that couples to the order parameter, and (implicitly) on the order parameter itself. If the assumption of a non-vanishing order parameter $\Phi \neq 0$ leads to a violation of (3.12) in the limit of a vanishing perturbation $V_0 \rightarrow 0$, the assumption must be dropped. This leaves the conclusion that $V_0 \rightarrow 0$ implies $\Phi \rightarrow 0$, so a phase transition cannot occur at any finite temperature.

Mermin and Wagner themselves applied the proof to show that the Heisenberg model does not show spontaneous magnetization for $d \leq 2$ [53]. The Heisenberg model is the $n = 3$ case of the general n -vector model. In classical mechanics, the latter places n -component, unit length, classical spins \mathbf{s}_i on the vertices of a d -dimensional lattice. With a next-neighbor coupling strength J , the interaction of the n -vector model is given by

$$W = -J \sum_{\{i,j\}} \mathbf{s}_i \cdot \mathbf{s}_j, \quad (3.13)$$

Table 3.1 Existence of long-range order in the n -vector model. The 2D XY model is peculiar insofar as it shows a phase transition, but no long-range order. The Ising model is included here although it does not have a continuous symmetry.

Dimension (d)	Ising ($n = 1$)	XY ($n = 2$)	Heisenberg ($n = 3$)
1D	no	no	no
2D	yes	(no)	no
3D	yes	yes	yes

where the sum runs over all pairs of neighboring spins $\{i, j\}$ and \cdot denotes the standard Euclidean inner product. Compare this to the Hamiltonian of the quantum Heisenberg model, i.e.

$$\hat{H}_{\text{Heisenberg}} = -J \sum_{\{i,j\}} (\hat{S}_i^+ \hat{S}_j^- + \hat{S}_i^z \hat{S}_j^z) - b \sum_i e^{-i\mathbf{K}\cdot\mathbf{r}_i} S_i^z, \quad (3.14)$$

where the second term is due to the interaction with an external magnetic field B_0 coupling with $b = g_J \mu_B B_0 / \hbar$.

The n -vector model is the reference for a system with continuous symmetry whose order parameter has n degrees of freedom. Hence, a “successful” proof implies that *all* systems which fall into the same universality class fail to show (long-range) order. Such proofs have been applied to many systems (for a recent survey see [54]). The findings are summarized in Tab. 3.1. The implication of Mermin-Wagner’s theorem is quite severe for 2D systems: It rules out spontaneous magnetization, superconductivity, superfluidity, and solids which all fall into the so-called XY class [54].

3.4 The Kosterlitz-Thouless Transition

Despite the above reasoning, there is a strikingly simple argument for the existence of a phase transition in the XY-model. It is based on the free energy needed for the creation of a particular spin pattern around a singular point. Such a topological defect is called *vortex* and disrupts the long-range spin-ordering. Two examples for vortices are shown in Fig. 3.1.

In harmonic approximation for the spin-spin interaction, the energy cost per spin falls off as $J/2(1/r)^2$ with distance r from the vortex core [79]. As there are $2\pi r dr$ spins at any distance, the energy E_{vortex} of a vortex is given by

$$E_{\text{vortex}}(L) - E_{\text{core}} = J\pi \int_{r_c}^L dr r^{-1} = J\pi \ln \frac{L}{r_c}. \quad (3.15)$$

The integral is bounded by the system size L to large distances and some (chosen but fixed) cutoff radius r_c to smaller distances where the harmonic approximation fails [cf. Fig 3.1]. The vortex energy associated to this core region is denoted as E_{core} and is unknown but finite. The number of possible locations of such a vortex is approximately $(L/r_c)^2$. This yields an entropic contribution of $S_{\text{vortex}} = 2k_B \ln(L/r_c)$ which diverges logarithmically with the system size like the vortex energy (3.15). Neglecting the core energy E_{core} , the total free energy change for the creation of a vortex reads

$$F_{\text{vortex}} = E_{\text{vortex}} - TS_{\text{vortex}} = J\pi \ln \frac{L}{r_c} - 2k_B T \ln \frac{L}{r_c}, \quad (3.16)$$

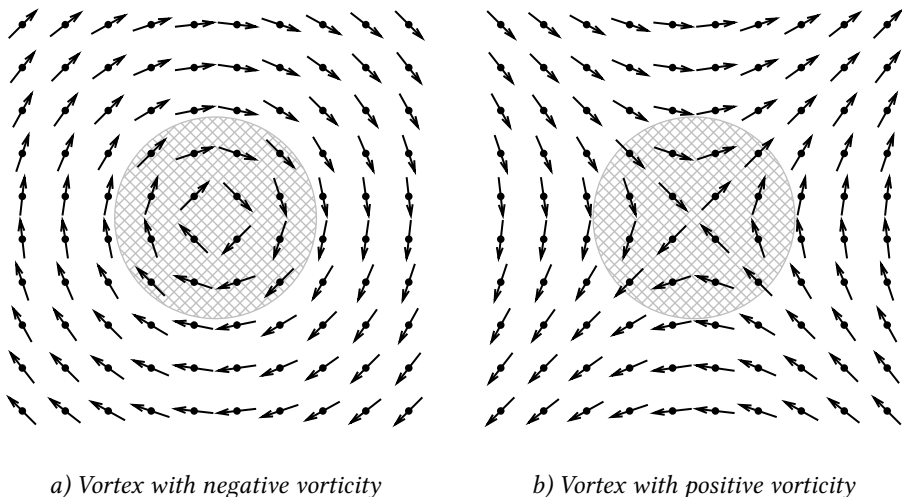


Figure 3.1 Two examples for a spin vortex in the lattice XY-model. Dots denote lattice points at which the spins are affixed. The shaded area denotes some arbitrary, yet finite core region where the harmonic approximation for the next-neighbor interaction fails.

which becomes favorable for $F < 0$. This calculations predicts a critical temperature

$$k_B T_{\text{cr}} = J \frac{\pi}{2}, \quad (3.17)$$

where the system crosses from a vortex-free phase to a disordered phase in which vortices are abound. Although further investigations reject this particular physical picture, a vortex driven phase transition does exist and the estimate (3.17) for T_{cr} is only modified to a small degree.

A vortex is a topological defect of the XY-model. The concept of a vortex driven transition was first discussed by Berezinskii [55] and fully developed by Kosterlitz and Thouless [56]. With the harmonic approximation for the spin-spin interaction, the reduced Hamiltonian for a system of vortices is given by [79]

$$H_{\text{vortex}} = E_{\text{core}} \sum_i q_i^2 - \pi K \sum_{i < j} q_i q_j \ln \left| \frac{\mathbf{r}_i - \mathbf{r}_j}{r_c} \right|, \quad 0 = \sum_i q_i, \quad (3.18)$$

which resembles the Hamiltonian for the 2D two-component Coulomb gas with the *vorticities* $q_i = \pm 1$ as particle charges and E_{core} acting as the chemical potential. Both the core energy and the coupling constant K are assumed to be temperature dependent. Since the creation of a single vortex leads to an infinite energy contribution [cf. Eq. (3.15)], only the creation of vortex-antivortex pairs is possible. In the language of the 2D Coulomb gas, the system is neutral with no surplus charges.

The analogy to a Coulomb system provides an intuitive view on the *Kosterlitz-Thouless transition* (KT): The system changes from a state with bound charges to a plasma. Or, when translated to the original spin model, the driving mechanism is the unbinding of bound pairs of vortices with opposite vorticities. The presence of such *vortex dipoles* or unbound free vortices acts analogously to a dielectric – the bare Coulomb interaction $V_0(r)$ between two test vortices with opposing signs is modified due to polarization or screening of the background. Hence, the dielectric response $\epsilon(k)$ is the key quantity for the description near the critical point T_{cr} [cf. Appx B].

The spin-spin correlation function in the presence of a vortex dipoles does not show long-range order (which is strictly forbidden according to the Mermin-Wagner theorem), but shows algebraic decay instead [79]. Usually, algebraic decay (with a decay exponent η) of correlation functions is a signature of phase transitions at the critical point. In the present case, critical point-like behavior extends over the whole low-temperature region of the phase diagram. Such a phase in which the correlation function exhibits algebraic decay, or *quasi long-range order*, is known as *critical phase*. Here, the decay exponent $\eta(T)$ is temperature dependent.

The KT theory is a renormalization-group treatment of the screening effects [80, 81]. The theory predicts a continuous melting transition from a phase characterized by quasi long-range order to a disordered phase. However, the coupling constant K renormalizes to a *universal* limiting value at the critical point and then jump discontinuously to zero. The critical temperature is the same as that predicted by the simple discussion above [Eq. (3.17)] when the coupling constant is replaced by its renormalized value [79].

The concept can be applied to both the lattice and the continuum version of the XY-model. The latter quite naturally applies to superfluids where vortices appear as (quantized) disruptions of the superfluid velocity field. Here, the critical temperature is given by the condition [82]

$$k_{\text{B}}T_{\text{cr}} = \frac{\pi}{2} \frac{\hbar^2}{m^2} n_{\text{s}} , \quad (3.19)$$

where n_{s} is the superfluid density at the critical point for $T \rightarrow T_{\text{cr}}^-$. Above T_{cr} , the superfluid density is zero. This prediction has been confirmed both experimentally, e.g. [57], and with Monte-Carlo studies, e.g. [83].

3.5 Melting

The Kosterlitz-Thouless transition of the XY-model strongly implies that 2D solids with quasi long-range translational order exist. Applying a defect-unbinding theory to melting, however, has its own complications. Two-dimensional particle

systems are characterized by *two* different order parameters, translational and orientational order. Consequently, there are two different types of topological defects, *dislocations*, i.e. at the end of an extra (or missing) row of particles stuck partway in the crystal, and *disclinations*, i.e. particles with more (or less) than 6 neighbors. The implications were considered independently by Halperin and Nelson [84, 85] and by Young [86]. The KTHNY theory of melting has been reviewed several times, a good overview can be found in [79].

Here, only the basic implications for the melting transition are sketched. As noted above, each type of topological defect has a “positive” and a “negative” charge and, thus, can bind in a “neutral” pair. Considering the two different types, only disclinations disrupt orientational order. KT theory then predicts a transition driven by the unbinding of disclination pairs. Below the critical point T_i , there is a phase with quasi long-range orientational order. Dislocations, on the other hand, disrupt translational order, so there exists a phase quasi long-range orientational order below a critical point T_m in which dislocations only occur in pairs.

Since dislocations may be viewed as a pair of disclinations, dislocations pairs are also bound pairs (quartets) of disclinations. Such quartets imply true long-range orientational order and $T_i > T_m$. Hence, KTHNY theory predicts a sequence of two continuous transitions from solid over an intermediate phase called *hexatic* to liquid. These findings are summarized in Tab. 3.2.

Table 3.2 Predictions of the KTHNY theory for 2D melting [79].

Phase	Solid	Hexatic	Fluid
Dislocations	Pairs	Free	Free
Disclinations	Quartets	Pairs	Free
Translational order	Quasi Long-Range	Short-Range	Short-Range
Orientalional order	Long-Range	Quasi Long-Range	Short-Range

PART II

Methods

Matrix Squaring

Explicit analytical expressions for the N -body density matrix $\rho(R, R'; \beta)$ only exist for non-interacting systems where the density matrix factorizes into single particle contributions [cf. Sec. 2.3]. In interacting systems, no closed analytical expressions for $\rho(R, R'; \beta)$ exist, but an approximation in terms of pair density matrices $\rho^{(2)}(\mathbf{r}_1, \mathbf{r}_2, \mathbf{r}'_1, \mathbf{r}'_2; \beta)$ is accurate at high temperatures [Sec. 2.4.4].

Constructing an accurate expression for the pair density matrix is far from trivial, however, as $\rho^{(2)}(\mathbf{r}_1, \mathbf{r}_2, \mathbf{r}'_1, \mathbf{r}'_2; \beta)$ is still a function of $4d + 1$ variables. Fortunately, most interaction potentials only depend on the pair distance $r_{12} = |\mathbf{r}_1 - \mathbf{r}_2|$. Under these circumstances, an efficient numerical procedure, called *Matrix Squaring*, exists which is capable of computing the pair density matrix at any temperature to a high degree of accuracy.

This chapter explains how a spherical potential reduces the complexity of the problem and how Matrix Squaring can be used to numerically compute the remaining density matrix. The method itself was developed by Storer [87] for attractive Coulomb forces and later applied to Lennard-Jones like interactions by Klemm and Storer [88]. Here it is presented in a general way with some extensions from [89].

4.1 Reduction of Complexity

Consider the two-particle Hamiltonian

$$\hat{h}_2^{\text{pair}} = -\frac{\hbar^2}{2m_1} \nabla_{\mathbf{r}_1}^2 - \frac{\hbar^2}{2m_2} \nabla_{\mathbf{r}_2}^2 + W(|\mathbf{r}_1 - \mathbf{r}_2|) , \quad (4.1)$$

where W is the pair interaction potential which only depends on the particle separation. This Hamiltonian can be rewritten with center-of-mass (cm) \mathbf{R} and relative

(rel) $\mathbf{r} = \mathbf{r}_1 - \mathbf{r}_2$ coordinates, i.e.

$$\hat{h}_2^{\text{pair}} = -\frac{\hbar^2}{2M} \nabla_{\mathbf{R}}^2 - \frac{\hbar^2}{2\mu} \nabla_{\mathbf{r}}^2 + W(|\mathbf{r}|) , \quad (4.2)$$

where $M = m_1 + m_2$ is the total mass and $\mu^{-1} = m_1^{-1} + m_2^{-1}$ is the reduced mass. The Bloch equation (2.21) for this Hamiltonian separates with the ansatz

$$\rho_2(\mathbf{r}_1, \mathbf{r}_2, \mathbf{r}'_1, \mathbf{r}'_2; \beta) = \rho_1^{\text{cm}}(\mathbf{R}, \mathbf{R}'; \beta) \rho_1^{\text{rel}}(\mathbf{r}, \mathbf{r}'; \beta) , \quad (4.3)$$

for the pair density matrix, yielding

$$\frac{\partial}{\partial \beta} \rho_1^{\text{cm}}(\mathbf{R}, \mathbf{R}'; \beta) = \frac{\hbar^2}{2M} \nabla_{\mathbf{R}}^2 \rho_1^{\text{cm}}(\mathbf{R}, \mathbf{R}'; \beta) , \quad (4.4)$$

$$\frac{\partial}{\partial \beta} \rho_1^{\text{rel}}(\mathbf{r}, \mathbf{r}'; \beta) = \left[\frac{\hbar^2}{2\mu} \nabla_{\mathbf{r}}^2 - W(|\mathbf{r}|) \right] \rho_1^{\text{rel}}(\mathbf{r}, \mathbf{r}'; \beta) . \quad (4.5)$$

Hence, the Bloch equation for $\rho_2(\mathbf{r}_1, \mathbf{r}_2, \mathbf{r}'_1, \mathbf{r}'_2; \beta)$ can be solved if both single particle density matrices independently satisfy these single particle Bloch equations. The initial condition splits into two separate conditions, $\rho_1^{\text{cm}}(\mathbf{R}, \mathbf{R}'; 0) = \delta(\mathbf{R} - \mathbf{R}')$ and $\rho_1^{\text{rel}}(\mathbf{r}, \mathbf{r}'; 0) = \delta(\mathbf{r} - \mathbf{r}')$.

Equation (4.4) is the known free particle problem considered in Sec. 2.3.1. Its solution can be noted down immediately [see Eq. (2.27)]:

$$\rho_1^{\text{cm}}(\mathbf{R}, \mathbf{R}'; \beta) = \left(\frac{M}{2\pi\hbar^2\beta} \right)^{d/2} \exp \left[-\frac{M}{2\hbar^2\beta} |\mathbf{R} - \mathbf{R}'|^2 \right] . \quad (4.6)$$

The relative particle problem (4.5) corresponds to the problem of a single particle in a spherical trap, i.e. a potential which only depends on the particle's distance to the trap center. In such cases, the Bloch equation can be solved by separating the variables by splitting off the angular variables. The procedure varies slightly with respect to the dimension of space d . For $d = 3$, one employs the spherical coordinate system (r, θ, ϕ) and considers the ansatz

$$\rho_1^{\text{rel}}(\mathbf{r}, \mathbf{r}'; \beta) = \frac{\rho^{\text{rad}}(r, r'; \beta)}{r r'} h(\theta, \phi, \theta', \phi') . \quad (4.7)$$

to separate the angular dependence from the radial density matrix $\rho^{\text{rad}}(r, r'; \beta)$. Some algebra shows that $\rho_1^{\text{rel}}(\mathbf{r}, \mathbf{r}'; \beta)$ solves the Bloch equation if and only if $\rho^{\text{rad}}(r, r'; \beta)$ and $h(\theta, \phi, \theta', \phi')$ individually satisfy

$$-\frac{\partial}{\partial \beta} \rho^{\text{rad}}(r, r'; \beta) = \left[-\frac{\hbar^2}{2\mu} \frac{\partial^2}{\partial r^2} + \frac{\hbar^2}{2\mu} \frac{l(l+1)}{r^2} + V(r) \right] \rho^{\text{rad}}(r, r'; \beta) , \quad (4.8)$$

$$0 = \left[-\nabla_{\theta, \phi}^2 + l(l+1) \right] h_l(\theta, \phi, \theta', \phi') , \quad (4.9)$$

with $l(l+1)$ with $l \in \mathbb{N}_0$ enumerating all possible solutions. These equations can be written for either the primed or unprimed coordinates due to the symmetry of the density matrix.

The general solution to the angular equation (4.9) are given by the usual *spherical harmonics* $Y_{lm}(\theta, \phi)$ with $|m| \leq l$ [90]. From these, the symmetrized angular contribution to the density matrix can be constructed as [87]

$$h_l(\theta, \phi, \theta', \phi') = \sum_{l=-m}^m Y_{lm}^*(\theta, \phi) Y_{lm}(\theta', \phi') = \frac{2l+1}{4\pi} P_l(\cos \alpha), \quad (4.10)$$

where the second step leverages the addition theorem for spherical harmonics to simplify the expression introducing the *Legendre polynomials* $P_l(x)$ with α as the in-plane angle between \mathbf{r} and \mathbf{r}' .

In the 2D case, one starts with the ansatz

$$\rho_1^{\text{rel}}(\mathbf{r}, \mathbf{r}'; \beta) = \frac{\rho^{\text{rad}}(r, r'; \beta)}{\sqrt{rr'}} h(\phi, \phi'). \quad (4.11)$$

One obtains the similar expressions as Eqs. (4.8) and (4.9), but with $l^2 + 1/4$ instead of $l(l+1)$ and the full integer range for l , i.e. $l \in \mathbb{Z}$. The angular solutions are given by

$$h_l(\phi, \phi') = \left(\frac{e^{-il\phi}}{\sqrt{2\pi}} \right)^* \left(\frac{e^{-il\phi'}}{\sqrt{2\pi}} \right) = \frac{1}{2\pi} e^{il\alpha} \quad (4.12)$$

where $\alpha = \phi - \phi'$ is the in-plane angle between \mathbf{r} and \mathbf{r}' .

Equation (4.8) for the radial density matrix has the form of a 1D Bloch equation, i.e.

$$-\frac{\partial}{\partial \beta} \rho_l^{\text{rad}}(r, r'; \beta) = \left[-\lambda_\mu \frac{\partial^2}{\partial r^2} + W_l^{\text{eff}}(r) \right] \rho_l^{\text{rad}}(r, r'; \beta), \quad (4.13)$$

with the quantumness $\lambda_\mu = \hbar^2/(2\mu)$ and the effective potential

$$W_l^{\text{eff}}(r) \equiv W(r) + \frac{\lambda_\mu}{r^2} \times \begin{cases} 0, & (1\text{D}), \\ l^2 + \frac{1}{4}, & (2\text{D}), \\ l(l+1), & (3\text{D}). \end{cases} \quad (4.14)$$

The second term is the usual effective contribution from the angular momentum quantized by l . Obviously, this part is missing in 1D. Equation (4.13) is the furthest point one can reach without specific knowledge of the potential. Finding solutions for $\rho_l^{\text{rad}}(r, r'; \beta)$ is what *Matrix Squaring* is about. This method is discussed in the next section.

In summary, the solution for the relative single-particle density matrix can be constructed from a partial wave expansion (not applicable to the 1D case), i.e.

$$(1D) \quad \rho_1^{\text{rel}}(\mathbf{r}, \mathbf{r}'; \beta) = \rho^{\text{rad}}(r, r'; \beta), \quad (4.15)$$

$$(2D) \quad \rho_1^{\text{rel}}(\mathbf{r}, \mathbf{r}'; \beta) = \frac{1}{2\pi\sqrt{rr'}} \sum_{l=-\infty}^{\infty} \rho_l^{\text{rad}}(r, r'; \beta) e^{il\alpha} \\ = \frac{1}{2\pi\sqrt{rr'}} \sum_{l=0}^{\infty} (2 - \delta_{0l}) \rho_l^{\text{rad}}(r, r'; \beta) T_l(\cos \alpha), \quad (4.16)$$

$$(3D) \quad \rho_1^{\text{rel}}(\mathbf{r}, \mathbf{r}'; \beta) = \frac{1}{4\pi rr'} \sum_{l=0}^{\infty} (2l + 1) \rho_l^{\text{rad}}(r, r'; \beta) P_l(\cos \alpha), \quad (4.17)$$

where $\rho_l^{\text{rad}}(r, r'; \beta)$ satisfies the 1D-Bloch equation with an effective Hamiltonian as given in Eq. (4.13). The T_l are the *Chebyshev polynomials* and the P_l are the *Legendre polynomials*. For both polynomials exist recurrence relations:

$$T_{l+1}(x) = 2x T_l(x) - T_{l-1}(x), \quad T_0(x) = 1, \quad T_1(x) = x, \quad (4.18)$$

$$(l + 1) P_{l+1}(x) = (2l + 1)x P_l(x) - l P_{l-1}(x), \quad P_0(x) = 1, \quad P_1(x) = x, \quad (4.19)$$

which simplify the numerical evaluation, e.g., by employing the *Clenshaw algorithm* [91, 92].

Equation (4.13) has an analytic solution for free particles, corresponding to the coefficients of a partial wave expansion of the free particle density matrix [Eq. (2.27)]. It can be compactly written as

$$\rho_l^0(r, r'; \beta) = \sqrt{\frac{1}{4\pi\lambda_\mu\beta}} \exp\left[-\frac{(r-r')^2}{4\lambda_\mu\beta}\right] \mathcal{I}_l\left(\frac{rr'}{2\lambda_\mu\beta}\right) \\ = \mathcal{G}_1(r-r'; \sqrt{2\lambda_\mu\beta}) \mathcal{I}_l\left(\frac{rr'}{2\lambda_\mu\beta}\right), \quad (4.20)$$

by introducing the scaled modified Bessel-functions

$$\mathcal{I}_l(x) = \sqrt{2\pi x} e^{-x} I_{l-1+\frac{d}{2}}(x) = \begin{cases} \sqrt{2\pi x} e^{-x} I_l(x), & d = 2, \\ 2x e^{-x} i_l(x), & d = 3, \end{cases} \quad (4.21)$$

where $I_l(x)$ and $i_l(x)$ denote the *modified Bessel functions* [93, Ch. 10.1] and *modified spherical Bessel functions* [93, Ch. 10.2], respectively. They are related by $i_l(x) = \sqrt{\pi/(2x)} I_{l+1/2}(x)$.

4.2 Matrix Squaring

The main idea of the *Matrix Squaring* method developed by Storer[87] centers around the convolution property of the density matrix [Eq. (2.23)]. Written in coordinate representation it reads

$$\rho(R, R'; 2\beta) = \int dR'' \rho(R, R''; \beta) \rho(R'', R'; \beta). \quad (4.22)$$

The message is that the density matrix at a any given temperature can be obtained by squaring the density matrices at twice the temperature. In theory, one should be able to derive the low temperature density matrix by iteratively squaring its high-temperature equivalent for which good approximations are available as the system behaves quasi classical.

In practice, one has to solve a key issue. A direct evaluation of Eq. (4.22) involves the computation of a dN -dimensional integral. If $\rho(R, R''; \beta)$ is tabulated on a grid with M points for each variable, the computational cost for a single integration is of order $\mathcal{O}(M^{dN})$ – and in order to determine the full 2β -density matrix, Eq. (4.22) must be repetitively evaluated for all of its M^{2dN} grid points. This kills any hope for a general application.

However, it is demonstrated in the previous section 4.1 that the pair density matrix $\rho^{(2)}(\mathbf{r}_1, \mathbf{r}_2, \mathbf{r}'_1, \mathbf{r}'_2; \beta)$ for a pair potential of the form $W(|\mathbf{r}_1 - \mathbf{r}_2|)$ factorizes into a center-of-mass and a relative density matrix, the latter of which can be expanded in partial waves. General analytical expressions for all ingredients are known but for the expansion coefficients $\rho_l^{\text{rad}}(r, r'; \beta)$. Because $\rho_l^{\text{rad}}(r, r'; \beta)$ satisfies a Bloch-equation (4.13), each coefficient is a density matrix in its own right. Thus, it also inherits all other applicable properties discussed in Ch. 2. In particular, the convolution property [Eq. (4.22)] for the radial density matrix $\rho_l^{\text{rad}}(r, r'; \beta)$ reads

$$\rho_l^{\text{rad}}(r, r'; 2\beta) = \int_0^\infty dr'' \rho_l^{\text{rad}}(r, r''; \beta) \rho_l^{\text{rad}}(r'', r'; \beta), \quad (4.23)$$

for each integer $l \geq 0$.

In contrast to Eq. (4.22), this equation requires the evaluation of only a one-dimensional integral with the computational cost of $\mathcal{O}(M)$. In theory, however, one now needs infinitely many integrations – one for each partial wave coefficient. In practice, a limited number l_{max} of partial waves is sufficient for the convergence to the relative density matrix, *especially* at low temperatures and small distances. Hence, the cost to compute the relative density matrix $\rho^{\text{rel}}(\mathbf{r}, \mathbf{r}'; \beta)$, when starting from its high-temperature partial wave expansion $\rho_l^{\text{rad}}(r, r'; 2^{-s}\beta)$, $s \in \mathbb{N}$ by iteratively using Eq. (4.23), is of the order $\mathcal{O}(sl_{\text{max}}M^3)$.

4.2.1 Implementation

For an efficient implementation of Matrix Squaring, one must ponder the following items:

- A good high temperature approximation is needed. This determines the number of iterations or *squarings* s needed to be reach the destined temperature β .
- A suitable integration scheme must be chosen. This requires to invest some thought on the discretization of the coordinate axis, i.e. how many points M are needed and up to which cutoff value r_{cut} .
- The question of how many partial waves l_{max} are necessary must be addressed.

Higher values for the parameters s , M , r_{cut} , and l_{max} improves the convergence to the sought $\rho^{\text{rel}}(\mathbf{r}, \mathbf{r}'; \beta)$, but also increases the run-time. The optimal values balance program execution and convergence and can be determined by simple trial and error. The next section goes into more detail when discussing the application of matrix squaring to some examples. Important for the actual implementation is the initial high temperature approximation, the internal representation and the integration.

As for the initialization, any high-temperature approximation presented in Sec. 2.4 will do. Better approximations allow to reduce the starting temperature of the matrix squaring while retaining the same accuracy. A convenient choice is the semiclassical approximation [Eq. (2.34)] which reads in partial wave expansion,

$$\rho_l^{\text{semi}}(r, r'; \beta) = \rho_l^0(r, r'; \beta) \exp \left[-\frac{\beta}{r - r'} \int_r^{r'} dr'' W(r'') \right], \quad (4.24)$$

where $\rho_l^{\text{free}}(r, r'; \beta)$ is defined in Eq. (4.20). This form justifies an alternative definition of the radial density matrix as

$$\rho_l^{\text{rad}}(r, r'; \beta) = \mathcal{G}_1(r - r'; \sqrt{2\lambda_\mu\beta}) \tilde{\rho}_l(r, r'; \beta), \quad (4.25)$$

where the common free-particle density matrix is factored out. The semiclassical approximation (4.24) is recovered for $\tilde{\rho}_l(r, r'; \beta) = \tilde{\rho}_l^{\text{semi}}(r, r'; \beta)$ with

$$\tilde{\rho}_l^{\text{semi}}(r, r'; \beta) \equiv \mathcal{I}_l \left(\frac{rr'}{2\lambda\beta} \right) \exp \left[-\frac{\beta}{r - r'} \int_r^{r'} dr'' W(r'') \right]. \quad (4.26)$$

The free-particle density matrix can be pulled out of the convolution integral (4.23) leaving

$$\tilde{\rho}_l(r, r'; 2\beta) = \frac{1}{\sqrt{\pi}} \int_{-\frac{a}{\sigma}}^{\infty} dz e^{-z^2} \tilde{\rho}_l(r, q + \sigma z; \beta) \tilde{\rho}_l(q + \sigma z, r'; \beta), \quad (4.27)$$

with the midpoint $q = (r + r')/2$ and the variance $\sigma^2 = 2\lambda_\mu\beta$.

For the integration scheme, the simplest choice is the trapezoidal integration coupled with a $M \times M$ square lattice representation of the density matrix (up to the cutoff r_{cut}). Then, Equation (4.23) literally corresponds to the squaring of a matrix. It is worth noting that above run-time estimation of $\mathcal{O}(M^3)$ for computing a single squared density matrix corresponds to the run-time of straightforward *naïve square matrix multiplication*. However, there exist *fast matrix multiplication* methods which perform better, like the original *Strassen algorithm* [94] with $\mathcal{O}(M^{\log_2 7}) \approx \mathcal{O}(M^{2.807})$ or the currently best-performing *Coppersmith–Winograd algorithm* [95] with $\mathcal{O}(M^{2.376})$. Such algorithms are readily available from standard Linear Algebra libraries.

Unfortunately, there is a catch for such an integration scheme. The density matrix is sharply peaked at the diagonal at high temperatures, but quite smooth at low temperatures. A qualitative measure for the spread from the diagonal is given by the variance of the free-particle density matrix $\sigma \propto \sqrt{\beta}$. Supposedly, an adequately tabulated density matrix needs a constant number of points per σ in off-diagonal direction. This implies that any fixed linear grid wastes most points at high temperatures and is far too dense at low ones: Even if just M points were sufficient at the initial temperature, a total of $M^{s/2}$ points is needed to achieve the necessary accuracy after s squarings. A square grid even requires M^s points, although the spacing of points on diagonal does – by itself – not scale with temperature.

In conclusion, the advantage in processing time which efficient matrix multiplication algorithms offer, cannot overcome the burden of the then necessary square grid. A much better efficiency is achieved with a slower integration method on smaller grids. According to above considerations, the grid must either be expanded on each squaring or its points spaced on a logarithmic scale.

The integration method can be freely chosen. Considering the convolution in Eq. (4.25), a natural choice [89] is the *Gauss-Hermite quadrature* [96, Ch. 4.6] applicable for integrals of the type

$$\int_{-\infty}^{\infty} dx e^{-x^2} f(x) = \sum_{i=1}^n w_i^{(n)} f(x_i^{(n)}) + R_n[f(x)], \quad (4.28)$$

where n is the order of the approximation, the x_i are the roots of the n -th Hermite polynomial $H_n(x)$ and the w_i are the weights with which the function value at this point contributes to the integral. They are given by [93, Ch. 25.4]

$$\{x_i^{(n)}\} = \{x \mid H_n(x) = 0\}, \quad w_i^{(n)} = \frac{2^{n-1}n!}{n^2} \sqrt{\pi} [H_{n-1}(x_i^{(n)})]^{-2}. \quad (4.29)$$

For any order n , the roots and their weights can be precomputed and tabulated.

An analytical expression of the remainder R_n is available [93, Ch. 25.4]; if $f(x)$ is a polynomial of n -th order, the Gauss-Hermite approximation of $n/2$ or

higher orders yields the exact result. Hence, Gauss-Hermite quadrature works well for polynomial integrands.

In the present case, the integrand of Eq. (4.25) has three separate peaks at $z = 0$, $z = (r-q)/\sigma$ and $z = (r'+q)/\sigma$ and each decays exponentially. Consequently, Gauss-Hermite quadrature should not be applied within the interval $\sigma z \in [-q, q]$ which severely limits its usefulness. In summary, one should not try too hard to find the optimal quadrature – the standard Simpson rule applied on this interval already accounts for all dominant contributions to the integral.

4.3 Beyond Matrix Squaring

There are at least two other methods for the numerical computation of pair density matrices. The first is simply an application of the *Path-Integral Monte Carlo* method introduced in the next chapter. The other is a direct computation from the sum of states (2.7). This is only possible if closed forms for bound states and continuum states of the system in question exist. The notable example here is the Coulomb potential [97] (see also Appx. C).

Matrix Squaring itself is related to the general mathematical problem considering the computation of the exponential of a matrix. Many methods have been proposed in the past and Matrix Squaring is one of the few methods preferable regarding the computational stability and efficiency [98]. Note that it can also be applied to compute derivatives of the density matrix. Some examples can be found in Appx. C.

Path-Integral Monte-Carlo

Richard Feynman introduced the path integral representation of the quantum system in 1948 which generalizes the action principle of classical mechanics. Within this theory, each quantum particle is considered as a series of positions forming a closed trajectory in space. The particle propagates along this trajectory obeying a law similar to the classical action. The physics of the system itself are derived from an functional integration over all possible paths, see [72, 74].

However, the explicit calculation of physical observables is somewhere limited, as huge amounts of computational time are needed in order to perform the integration. The combination with Monte Carlo integration method remedies this issue and constitutes the *path integral Monte Carlo (PIMC)* method [89]. It is suited for statistical investigations of a quantum system at any finite temperature. In principle, all errors due to necessary approximations can be made arbitrarily small, which makes PIMC a powerful numerical method based on first principles [99].

5.1 Discrete Imaginary-Time Path-Integrals

As with matrix squaring, path-integral Monte-Carlo (PIMC) leverages the convolution property of the density matrix [Eq. (2.23)], although to a quite different end.

Recall the original product property of the density operator as laid out in Sec. 2.2.3. Obviously, if the product of two density operators is a density operator, so is the product of any higher number than two, i.e. one has the property

$$\hat{\rho}(\beta) = e^{-\beta\hat{H}} = \left[e^{-\beta/M\hat{H}} \right]^M = [\hat{\rho}(\beta/M)]^M, \quad (5.1)$$

for any $M \in \mathbb{N}$. Written in coordinate representation with labeled particles, above equation leads to the *discrete imaginary time path-integral representation* of the

density matrix of distinguishable particles

$$\rho(R, R'; \beta) = \int dR_1 dR_2 \dots dR_{M-1} \rho(R, R_1; \tau) \rho(R_1, R_2; \tau) \dots \rho(R_{M-1}, R'; \tau), \quad (5.2)$$

with the *imaginary time step* $\tau = \beta/M$. The term *imaginary time* reflects the picture of the density operator resembling an imaginary-time propagator.

In the limit $M \rightarrow \infty$, above representation corresponds to the path-integral interpretation of quantum mechanics introduced by Feynman [72, 74]. However, Equation (5.2) is exact for *any* M as long as the exact density matrix is inserted in the r.h.s..

For a given physical system, one is typically not interested in the full N -particle density matrix directly, but in measurable quantities or, more generally, the partition function Z . Written in path-integral representation, the partition function of a system of N bosons reads [cf. (2.16)]

$$Z = \frac{1}{N!} \sum_{P \in S_N} \int dR_0 \dots dR_{M-1} \rho(R_0, R_1; \tau) \dots \rho(R_{M-1}, PR_0; \tau). \quad (5.3)$$

In the following, the shortcut $R_M \equiv PR_0$ is used frequently. A similar expression for the fermionic Z is found when using Eq. (2.18) instead. If neither quantum statistics have a large impact on the partition function, one has $\rho(R, PR'; \beta) = \rho(R, R'; \beta) \delta(R' - PR')$ and the sum over all permutations drops out. Such distinguishable particles are also called *boltzmannons*.

5.1.1 Notation and Classical Interpretation

The path-integral representation shares striking similarities with classical polymers and the commonly used notation reflects this fact.

The sequence of all coordinates in a specific configuration s is called the *path*, $s = \{R_0, R_1, \dots, R_{M-1}, R_M\}$, with $R_0 \equiv R$ and $R_M \equiv PR$. A single R_α , the α^{th} *time slice*, is associated with the imaginary time $\alpha\tau$. As already introduced, R_α represents the dN coordinates of N particles, $R_\alpha = \{\mathbf{r}_{1,\alpha}, \dots, \mathbf{r}_{N,\alpha}\}$, the position $\mathbf{r}_{j,\alpha}$ of the j^{th} particle on the α^{th} time-slice is called *bead*.

An individual particle can be thought to propagate in the discretized imaginary time interval $[0; M\tau]$ following a *trajectory* or *world-line* of beads. In conventional PIMC, one considers only paths which are periodic on the $\beta = M\tau$ -interval. Coupled with the physical indistinguishability of particles (expressed by $R_0 \equiv R$ and $R_M \equiv PR$), the $(M-1)^{\text{th}}$ bead of each trajectory links to zeroth bead of either the same, or another trajectory. The picture of the configuration space is that of closed loops on the $(d+1)$ -dimensional surface of a $(d+2)$ -dimensional β -cylinder which is divided into M equidistant imaginary time hyperplanes, the time-slices. A trajectory which winds l times around the β -cylinder

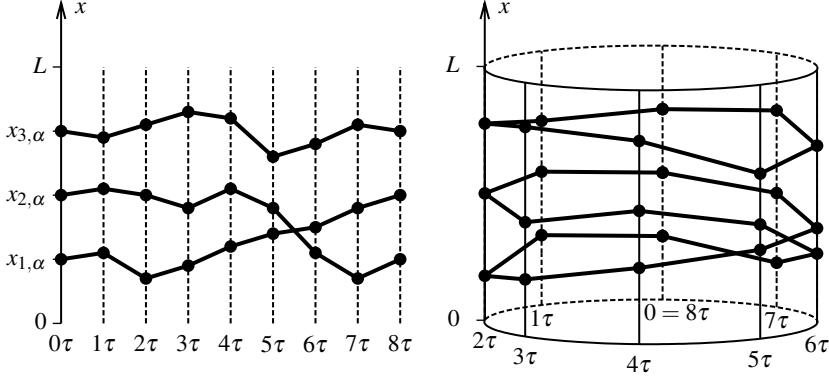


Figure 5.1 World-lines of 3 1D-particles. Left-hand panel represents a single configuration (path) with $M = 8$ time-slices (vertical lines). The beads (black dots) on the first and last time-slice are the same, but the single-particle trajectories (black lines, with 8 links each) do not necessarily end on their initial values. The righthand panel illustrates the physical picture more clearly – neither time-slice is the first due to the β -periodicity, but an imaginary time order is still imposed. One cannot distinguish the trajectories of particles 1 and 2, only the number of exchange cycles is known and how many particles are involved in each.

before closing on the initial position, represents l particles involved in the same exchange cycle.

The α^{th} link is the pair of time-slices $(R_{\alpha-1}, R_{\alpha})$ connected with the density matrix $\rho(R_{\alpha-1}, R_{\alpha}; \tau)$. One defines the *action* of the link as

$$S_{\alpha} \equiv S(R_{\alpha-1}, R_{\alpha}; \tau) = -\ln [\rho(R_{\alpha-1}, R_{\alpha}; \tau)] , \quad (5.4)$$

where $\rho(R_{\alpha-1}, R_{\alpha}; \tau)$ denotes the exact density matrix. It is beneficial to factor out known contributions from the exact link-action before applying some approximation. To this end, one defines the *kinetic action* as

$$K_{\alpha} \equiv K(R_{\alpha-1}, R_{\alpha}; \tau) = -\frac{dN}{2} \ln(4\pi\lambda\tau) + \frac{(R_{\alpha-1} - R_{\alpha})^2}{4\lambda\tau} , \quad (5.5)$$

with the quantumness $\lambda = \hbar^2/(2m)$. Equation (5.5) follows directly from inserting the free-particle density matrix [Eq. (2.27)] into Eq. (5.4). The *inter-action* is the remainder

$$U_{\alpha} \equiv U(R_{\alpha-1}, R_{\alpha}; \tau) = S_{\alpha} - K_{\alpha} . \quad (5.6)$$

With “action” one frequently refers to U , but of course the complete action includes kinetic contributions.

Using above definitions, the path-integral representation of the density matrix can be expressed in term of the action. The two following are among the most common

$$\rho(R_0, R_M; \beta) = \int dR_1 \dots dR_{M-1} e^{-\sum_{\alpha=1}^M S_{\alpha}} \quad (5.7)$$

$$= \int dR_1 \dots dR_{M-1} \prod_{\alpha=1}^M \rho_0(R_{\alpha-1}, R_{\alpha}; \tau) e^{-U_{\alpha}} . \quad (5.8)$$

5.1.2 High-Temperature Approximation

At the first glance, the usefulness of Eq. (5.3) is elusive as one has to solve a dNM -dimensional integration for each of the $N!$ possible permutations. However, such high-dimensional integrals can be very efficiently evaluated with *Monte-Carlo* methods [100]. Using high-temperature approximations for $\rho(R, R'; \tau)$ [Sec. 2.4] on the r.h.s of Eq. (5.2) one has the basic components of the *Path-Integral Monte-Carlo* (PIMC) method [89].

The problem of approximating the high-temperature density matrix is equivalent to finding an expression for the inter-action U . For example, the primitive approximation of commuting kinetic and potential operators implies for U :

$$U_{\alpha}^{\text{prim}} = \frac{\tau}{2} [V(R_{\alpha-1}) + V(R_{\alpha})] , \quad (5.9)$$

with $V(R) = \langle R | \hat{V} | R \rangle$. As discussed in Sec. 2.4.1, the primitive approximation neglects the commutator $[\hat{T}, \hat{V}]$ from the operator identity (2.29). As a result, the error of U^{prim} is proportional to τ^2 . The error vanishes in the limit $M \rightarrow \infty$ from U^{prim} , but in the infinite product (5.8), the infinitesimal errors might build up to finite error. According to the Trotter theorem [101], however, the identity

$$e^{-\beta(\hat{T}+\hat{V})} = \lim_{M \rightarrow \infty} \left[e^{-\tau\hat{T}} e^{-\tau\hat{V}} \right]^M , \quad (5.10)$$

holds as long as the operators \hat{T} , \hat{V} , and $\hat{T} + \hat{V}$ are self-adjoint and make sense separately. This is the case for Hamiltonians describing existing physical systems.

5.2 Action

With the primitive action as valid high-temperature approximation, one has all ingredients to r.h.s of Eq. (5.3) and could start evaluating the integral [Sec. 5.3]. With a better approximation, however, the number of time-slices needed to achieve the same overall error can be significantly reduced.

Section 2.4 lists several high-temperature approximations for the N -particle density matrix. In particular, Sec. 2.4.4 shows how to construct $\rho(R, R'; \beta)$ from

two-body density matrices. If the pair potential only depends on the relative distance, i.e. $W(\mathbf{r}_1, \mathbf{r}_2) = W(\mathbf{r}_{12})$ with $\mathbf{r}_{12} = \mathbf{r}_1 - \mathbf{r}_2$, Equation (2.41) can be rewritten for the inter-action as

$$U^{\text{pair}}(R, R'; \tau) = \sum_j^N u_1(\mathbf{r}_j, \mathbf{r}'_j; \tau) + \sum_{j < k}^N u_2(\mathbf{r}_{jk}, \mathbf{r}'_{jk}; \tau), \quad (5.11)$$

where $u_1(\mathbf{r}_j, \mathbf{r}'_j; \tau)$ is the exact action for the j^{th} particle and $u_2(\mathbf{r}_{jk}, \mathbf{r}'_{jk}; \tau)$ the exact action for the particles j and k . Note that u_2 is effectively a single-particle action due to the initial assumption. U^{pair} is exact for a pair of particles and neglects only 3 and higher-body correlations in general. This approach was first suggested by Barker [102] and is now commonly referred to as *pair action* approximation [89, 99].

The pair action is only useful if u_1 and u_2 are known. However, the underlying external or pair potential are often spherical, i.e. $V(\mathbf{r}) = V(|\mathbf{r}|)$ and $W(\mathbf{r}) = W(|\mathbf{r}|)$. Then, one may expand the corresponding density matrix in terms of partial waves [cf. 4.1]. The expansion coefficients only depend on the radial distance from the potential center. If given in such form, the action can be computed from the expansion with

$$u(\mathbf{r}, \mathbf{r}'; \tau) = \frac{d-1}{2} \ln \left(\frac{rr'}{\pi\lambda\beta} \right) + \frac{rr'}{2\lambda\beta} (\cos \alpha - 1) - \ln \left[\frac{1}{\pi} \sum_{l=0}^{\infty} c_l \tilde{\rho}_l(r, r'; \tau) F_l(\cos \alpha) \right], \quad (5.12)$$

where u denotes either u_1 or u_2 , the expansion coefficients are $c_l^{2\text{D}} = 2 - \delta_{l0}$ or $c_l^{3\text{D}} = 2l + 1$ and the F_l are the Chebyshev polynomials (2D) or the Legendre polynomials (3D), respectively. α denotes the angle between \mathbf{r} and \mathbf{r}' .

The partial wave expansion reduces the complexity from a single d -dimensional problem to l -1D problems. This is crucial for the computation of the radial density matrices $\tilde{\rho}_l(r, r'; \tau)$ with an integration scheme like Matrix Squaring [Ch. 4]. However, the reconstruction (5.12) converges rather slowly, especially for large r and for high temperatures τ . PIMC simulations repeatedly evaluate the same inter-action over and over and benefits greatly from a more suitable representation than (5.12).

Although single-particle inter-actions depend on 6 separate coordinates, only the 3 relative distances between initial and final coordinates matter. Consider the following distances

$$q = \frac{r + r'}{2}, \quad s = |\mathbf{r} - \mathbf{r}'|, \quad z = r - r'. \quad (5.13)$$

The density matrix peaks on the diagonal and its off-diagonal elements decay on the order of the thermal de Broglie wavelength, so the off-diagonal s and z are

small and one can expand the action in a power series which reads

$$u(\mathbf{r}, \mathbf{r}'; \beta) = u^{\text{end}}(r, r'; \beta) + \sum_{k=1}^{\infty} \sum_{j=0}^k u_{kj}(q; \beta) z^{2j} s^{2(k-j)}, \quad (5.14)$$

$$u^{\text{end}}(r, r'; \beta) = \frac{u_0(r; \beta) + u_0(r'; \beta)}{2}. \quad (5.15)$$

The first term $u^{\text{end}}(r, r'; \beta)$ is called *end-point action*. The end-point action collects all diagonal terms from the exact pair inter-action. The higher order expansion coefficients $u_{kj}(q; \beta)$ are purely off-diagonal contributions. The end-point action is equivalent to the primitive action for an effective temperature-dependent potential where

$$\tau V^{\text{eff}}(r; \tau) = u^{\text{end}}(r, r; \tau). \quad (5.16)$$

Although the end-point action alone constitutes an advantage over the primitive action, one must take the off-diagonal contribution into account to achieve a significant reduction of necessary time-slices in PIMC. Fortunately, in contrast to the partial wave expansion (5.12), the power series expansion typically converges very fast. A neat example is the inter-action of the harmonic oscillator where the expansion terminates after the first order:

$$u_0(r; \beta) = \frac{r^2}{\nu^2} \tanh f - \frac{d}{2} \ln \left(\frac{2f}{\sinh(2f)} \right) \quad (5.17)$$

$$u_{10}(q; \beta) = \frac{1}{4\nu^2} [\coth f - \tanh f - f^{-1}] \quad (5.18)$$

$$u_{11}(q; \beta) = 0 \quad (5.19)$$

All higher order contributions are exactly zero. Figure 5.2 shows the harmonic end-point action at several temperatures using the interpretation as temperature-dependent potential [Eq. (5.16)]. The constant off-diagonal contribution to the harmonic inter-action is not shown.

5.3 Monte-Carlo Sampling

The path-integral representation of the partition function in conjunction with an approximate high-temperature expression of the density matrix covers the physical aspect of the PIMC method. The remaining issue is the actual numerical evaluation of the high-dimensional integral.

A straightforward naïve integration is out of question as the computational complexity grows linearly with the number of integration variables N . The *Monte Carlo (MC)* integration tackles the scaling problem by sampling over randomly

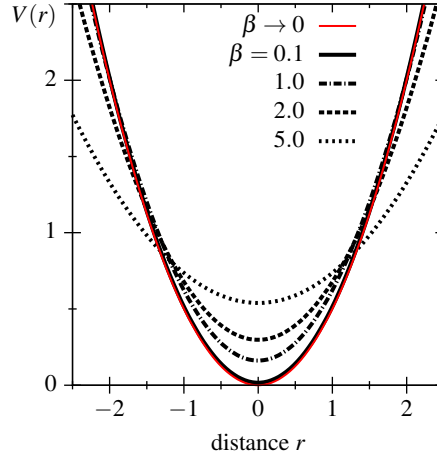


Figure 5.2 End-point action of the harmonic potential interpreted as effective potential according to Eq. (5.16). The red line corresponds to the classical potential recovered in the limit $\beta \rightarrow 0$. All quantity values are given in harmonic oscillator units.

distributed points $\tilde{\mathbf{x}}_i$ from the integration basis, e.g. \mathbb{R}^N . For some function $f : \mathbb{R}^N \rightarrow \mathbb{R}$ this means

$$\int d\mathbf{x} f(\mathbf{x}) = \int d\mathbf{x} \frac{f(\mathbf{x})}{p(\mathbf{x})} p(\mathbf{x}) = \lim_{M \rightarrow \infty} \frac{1}{M} \sum_{i=1}^M \frac{f(\tilde{\mathbf{x}}_i)}{p(\tilde{\mathbf{x}}_i)}, \quad (5.20)$$

where the probability of sampled points $\tilde{\mathbf{x}}_i$ is given by $p(\mathbf{x})d\mathbf{x}$. One may consider the integral as the expectation value of the function $f(\mathbf{x})/p(\mathbf{x})$.

The probability distribution p can be chosen arbitrarily. For the problem in question, $p(s)$ can be interpreted as the canonical weight of the microstate s which is given by $\pi(s)/Z$ with

$$\pi(s) = \prod_{\alpha=1}^M \rho(R_{\alpha-1}, R_{\alpha}; \tau) = \prod_{\alpha=1}^M \rho_0(R_{\alpha-1}, R_{\alpha}; \tau) e^{-U_{\alpha}}, \quad (5.21)$$

and $s = \{R_0, \dots, R_M\}$ with $R_M = PR_0$.

Unfortunately, one needs the partition function Z to generate microstates distributed according to $\pi(s)/Z$. Since the partition function is not known a priori, one constructs a so-called Markov chain which is a sequence of configurations with a fixed *transition probability* $P(s, s')$ to advance from microstate s to s' . Due to the law of conservation, the probability to reach *any* state must be one,

$$\sum_{s'} P(s, s') = 1, \quad (5.22)$$

and the transitions between states at equilibrium must leave the distribution of states invariant, i.e.

$$\sum_s \pi(s) P(s, s') = \pi(s'). \quad (5.23)$$

Eqs. (5.22) and (5.23) imply that 1 is an eigenvalue of P . The Perron-Frobenius theorem states that all remaining eigenvalues must all be less than 1, otherwise convergence to equilibrium cannot be attained. In such a case, kernel P is called primitive. Primitive Markov chains are also called *ergodic* or *regular* and they converge to a unique stationary limit if and only if the transition matrix P satisfies (5.23), which is commonly referred to as the *balance condition*. Note that the balance condition holds regardless of whether $\pi(s)$ is normalized or not.

One may devise a more strict condition known as *detailed balance*

$$\pi(s)P(s, s') = \pi(s')P(s', s) \quad (5.24)$$

which automatically satisfies the balance condition (5.23) if P obeys (5.22). The inverse is not true in general – the detailed balance condition is sufficient but not necessary to guarantee for the convergence of an ergodic Markov chain to its stationary limit.

Metropolis *et al.* [103] devised an ingenious way to construct the transition probabilities $P(s, s')$. In the *general Metropolis scheme*, $P(s, s')$ is split into an a priori *sampling distribution* $T(s, s')$ and an *acceptance probability* $A(s, s')$, i.e.

$$P(s, s') = T(s, s')A(s, s') . \quad (5.25)$$

For any chosen $T(s, s')$ the acceptance probability

$$A(s, s') = \min \left[1, \frac{T(s', s)\pi(s')}{T(s, s')\pi(s)} \right] \quad (5.26)$$

is sufficient for $P(s, s')$ to satisfy detailed balance. The proof is easy when considering that $A(s, s') = T(s', s)\pi(s')/T(s, s')\pi(s)$ implies $A(s', s) = 1$ and vice versa.

The sampling distribution $T(s, s')$ determines the probability for an attempt to move from the state s to s' . The acceptance probability $A(s, s')$ determines if this attempt is accepted or rejected. It is important to realize that although the variables of s' remain unchanged in the latter case, the state does still contribute to Eq. 5.21. This is why *any* choice for the sampling distribution is valid – Eq. (5.26) corrects for that by balancing accepted and rejected moves.

Obviously, states generated with Markov chains are correlated. Although bad performance can be counteracted by sampling more configurations, a better way is to increase the efficiency of the algorithm by minimizing the correlations. A careful choice of $T(s, s')$ can speed up convergence significantly. The optimal choice is the *heat bath transition rule* [89]

$$T_{\text{opt}}(s, s') = \frac{\pi(s')}{C_s} , \quad C_s = \sum_{s'' \in \mathcal{N}(s)} \pi(s''), \quad (5.27)$$

where the *neighborhood* $\mathcal{N}(s)$ is the set of all states which can be reached with a single move from s . Eq. (5.26) will then simply read

$$A_{\text{opt}}(s, s') = \min \left[1, \frac{C_s}{C_{s'}} \right]. \quad (5.28)$$

If the neighborhoods of s and s' are identical, then all moves will be accepted. From the definition (5.27), the normalization constant represents a kind of local partition function. Unfortunately, there is usually no convenient way to compute this constant in continuous space Monte-Carlo. However, one can use Eq. (5.27) as a guideline to construct efficient sampling distributions.

For PIMC, the elementary operation is the sampling of a single point on the path. More elaborate manipulations build upon this move. Without loss of generality, the task is to sample a new coordinate \mathbf{r}'_1 for a chosen bead which is connected to two fixed end points, located at \mathbf{r}_0 and \mathbf{r}_2 at the imaginary-times 0 and 2τ , respectively. The neighborhood of this move is the subspace obtained by fixing $d(NM - 1)$ variables (and the permutation), but allowing the remaining d coordinates vary throughout the box. According to the heat bath rule, the optimal choice for the sampling distribution is then given by

$$T_{\text{single}}^*(s, s') = \frac{1}{NM} \frac{1}{C_s} \rho(R_0, R'_1; \tau) \rho(R'_1, R_2; \tau), \quad (5.29)$$

where $1/(NM)$ is the probability to randomly choose a bead (out of a total NM) and with the normalization

$$C_s = \int dR'_1 \rho(R_0, R'_1; \tau) \rho(R'_1, R_2; \tau) = \rho(R_1, R_2; 2\tau). \quad (5.30)$$

As the neighborhood remains unchanged (i.e. $R'_0 = R_0$ and $R'_2 = R_2$), all moves will be accepted.

As noted before, it is unfeasible to compute the necessary normalization factor C_R , especially in the presence of long-range potentials. A related, but simpler method known as *free particle sampling*, drops all potential contributions and untouched coordinates from the sampling distribution. Then, one has [cf. Appx. D.1]

$$\begin{aligned} T_{\text{single}}(R, R') &= \frac{1}{NM} \frac{\rho_0(\mathbf{r}_0, \mathbf{r}'_1; \tau) \rho_0(\mathbf{r}'_1, \mathbf{r}_2; \tau)}{\rho_0(\mathbf{r}_0, \mathbf{r}_2; 2\tau)} \\ &= \frac{1}{NM} \frac{1}{(2\pi\lambda\tau)^{d/2}} \exp \left[-\frac{(\mathbf{r}_m - \mathbf{r}')^2}{2\lambda\tau} \right], \end{aligned} \quad (5.31)$$

with the midpoint $\mathbf{r}_m = (\mathbf{r}_0 + \mathbf{r}_2)/2$. Disregarding the leading factor, this distribution corresponds to a normalized Gaussian centered at \mathbf{r}_m with the width $\sqrt{\lambda\tau}$. Gaussian deviates can be easily sampled from uniform deviates with the Box-Muller transformation [96] or improvements on this method [104, 105].

The terms neglected in the sampling distribution reappear in the acceptance probability: Inserting Eq. (5.31) into Eq. (5.26) yields

$$A_{\text{single}}(s, s') = \min \left[1, e^{-\Delta U} \right], \quad (5.32)$$

where the difference of interactions, ΔU , is given by

$$\Delta U = U(R_0, R'_1) + U(R'_1, R_2) - U(R_0, R_1) - U(R_1, R_2). \quad (5.33)$$

Note that the action difference of *two* links contribute to Eq. (5.33). If $U(R, R')$ is diagonal, e.g. when using the primitive or the endpoint approximation, the explicit dependence on the endpoints R_0 and R_2 drops out of Eq. (5.33) leaving an expression of the form $\Delta U = \tau(V(R'_1) - V(R_1))$. In this case, PIMC very much resembles M classical Monte-Carlo simulations coupled by kinetic energy links.

It is certainly possible to improve upon free-particle sampling for single point moves. Such schemes try to incorporate some part of the inter-action into the sampling distribution, either explicitly or by using clever approximations. However, discussion of the fine points in this direction is beyond the scope of this thesis. A good overview can be found in Ref. [89].

Although single point moves already ensure traversal through the full spatial configuration space (i.e. excepting the permutation space), its overall performance is poor. More effective sampling schemes attempt to move several beads at once. With respect to PIMC, they are commonly called *multi-slice moves* and the following sections list the most important ones.

5.3.1 Staging

Staging refers to the straightforward extension of single bead sampling to a string of connected beads. More specifically, one attempts to sample a randomly chosen number $P \leq P_{\text{max}}$ of free-particle links between two fixed endpoints, \mathbf{r}_0 and \mathbf{r}_P , spaced $P\tau$ time-steps apart. One may think of the procedure akin to growing a new set of $P - 1$ beads from one endpoint to the other.

The sampling distribution simply resembles a generalized variant of Eq. (5.31), i.e.

$$T_{\text{stage}}(s, s') = \frac{1}{NM(P_{\text{max}} - 1)} \frac{1}{\rho_0(\mathbf{r}_0, \mathbf{r}_P; P\tau)} \prod_{\alpha=1}^P \rho_0(\mathbf{r}'_{\alpha}, \mathbf{r}'_{\alpha+1}; \tau) \quad (5.34)$$

where $\mathbf{r}'_0 = \mathbf{r}_0$ and $\mathbf{r}'_P = \mathbf{r}_P$. The normalization picks up an additional factor $P_{\text{max}} - 1$ accounting for the freedom to chose any $P \in [2, P_{\text{max}}]$. However, this form is unsuitable for sampling as it would require to sample all intermediate beads $\mathbf{r}_1, \dots, \mathbf{r}_{P-1}$ at once. A better approach is to rewrite Eq. (5.34) into a

product of conditional probabilities

$$\begin{aligned}
 T_{\text{stage}}(s, s') &= \frac{1}{NM(P_{\text{max}} - 1)} \prod_{\alpha=2}^{P-1} \frac{\rho_0(\mathbf{r}'_{\alpha-1}, \mathbf{r}'_{\alpha}; \tau) \rho_0(\mathbf{r}'_{\alpha}, \mathbf{r}_P; (P - \alpha)\tau)}{\rho_0(\mathbf{r}_{\alpha-1}, \mathbf{r}_P; (P - \alpha + 1)\tau)} \\
 &= \frac{1}{NM(P_{\text{max}} - 1)} \prod_{i=2}^{P-1} \frac{1}{(2\pi\lambda\tau_{\alpha})^{d/2}} \exp \left[-\frac{(\mathbf{r}_{m,\alpha} - \mathbf{r}'_{\alpha})^2}{2\lambda\tau_{\alpha}} \right], \tag{5.35}
 \end{aligned}$$

where the reduced temperature τ_{α} and the weighted midpoints $\mathbf{r}_{m,\alpha}$ are defined as [cf. Appx. D.1]

$$\tau_{\alpha} = \frac{P - \alpha}{P - \alpha + 1} \tau, \quad \mathbf{r}_{m,\alpha} = \frac{(P - \alpha)\mathbf{r}'_{\alpha-1} + \mathbf{r}_P}{P - \alpha + 1}. \tag{5.36}$$

In contrast to Eq. (5.34), Equation (5.35) corresponds to the subsequent sampling of new points as each new midpoint requires knowledge of the formerly sampled point. Thereby, each new point \mathbf{r}'_{α} is sampled from a normalized Gaussian centered at this midpoint with the width $\sqrt{\lambda\tau_{\alpha}}$.

The acceptance probability keeps the functional form of Eq. (5.32), but the inter-action difference must be computed over all newly sampled and discarded links, i.e.

$$\Delta U = \sum_{\alpha=1}^P U(R'_{\alpha-1}, R'_{\alpha}) - U(R_{\alpha-1}, R_{\alpha}), \tag{5.37}$$

where $R'_0 = R = 0$ and $R'_P = R_P$.

5.3.2 Bisectioning

Instead of growing the trajectory from one end as above, one may use a Lévy construction. Hereby, the midpoint of the new trajectory pieces is sampled first leaving two half-length trajectory pieces. Then, one recursively applies the same procedure to each half until all beads are sampled. For convenience, the original number of links is chosen as $P = 2^l$ with $1 \leq l \leq l_{\text{max}}$.

Without further modifications, bisectioning basically is identical to staging, but uses an alternative sampling method for the trajectory points. However, one can implement bisectioning as a *multi-level* move [cf. Appx. D.1] where the midpoint sampling of trajectories with 2^k links is done on the k^{th} level (counting from l to 1). After each level, one tests the so-far sampled points according to a modified level acceptance probability $A_k(s, s')$. $A_k(s, s')$ is constructed in such a way that $\sum_{k=1}^l A_k(s, s')$ corresponds to Eq. (5.32) with ΔU as in Eq. (5.37). As the midpoint on the k^{th} level is stochastically displaced the furthest, it has the highest

impact on the acceptance probability. Thus, early rejections of immature trajectories save the computational trouble to fully develop bad attempts.

The specifics of multi-level moves are explained in Appx. D.1. For bisectioning, one chooses the level sampling distributions according to (disregarding the initial normalization constant $1/(N M l_{\max})$)

$$\begin{aligned}
 T_k^{\text{bisect}}(s_k, s'_k) &= \prod_{\alpha=1}^{2^{l-k}} \frac{\rho_0(\mathbf{r}'_{2^{(\alpha-1)}\delta_k}, \mathbf{r}'_{2^{(\alpha-1)}\delta_k}; \delta_k \tau) \rho_0(\mathbf{r}'_{2^{(\alpha-1)}\delta_k}, \mathbf{r}'_{2^{\alpha}\delta_k}; \delta_k \tau)}{\rho_0(\mathbf{r}'_{2^{(\alpha-1)}\delta_k}, \mathbf{r}'_{2^{\alpha}\delta_k}; 2\delta_k \tau)}, \\
 &= \prod_{\alpha=1}^{2^{l-k}} \frac{1}{(2\pi\lambda\delta_k\tau)^{d/2}} \exp\left[-\frac{(\mathbf{r}_{m,\alpha}^{(k)} - \mathbf{r}'_{2^{(\alpha-1)}\delta_k})^2}{2\lambda\delta_k\tau}\right], \quad (5.38)
 \end{aligned}$$

with the fixed endpoints $\mathbf{r}'_0 = \mathbf{r}_0$ and $\mathbf{r}'_{2^l\delta_l} = \mathbf{r}_{2^l\delta_l}$, the level link length $\delta_k = 2^{k-1}$ and the level midpoints

$$\mathbf{r}_{m,\alpha}^{(k)} = \frac{\mathbf{r}'_{2^{(\alpha-1)}\delta_k} + \mathbf{r}'_{2^{\alpha}\delta_k}}{2}. \quad (5.39)$$

The level acceptance probability is

$$A_k^{\text{bisect}}(s_k, s'_k) = \min\left[1, e^{-\Delta U_k} e^{\Delta U_{k+1}}\right], \quad \Delta U_{l+1} = 0, \quad (5.40)$$

where $\Delta U_k = U(s'_k) - U(s_k)$ is the inter-action difference between the new and old configurations of all coordinates sampled down to the k^{th} level. Note that, on each level, the inter-action difference from the previous level is subtracted. Hence, one may use functionally different inter-actions on all levels save the last where the correct inter-action must be used.

5.3.3 Whole-Chain Displacement

Whole-Chain Displacement is the equivalent of the classical Monte-Carlo move where a particle is randomly displaced within a box. Here, each point of a closed loop of M links is displaced by the same vector \mathbf{n} . If chosen uniformly within a box with a Volume of $V = \Delta^d$, the sampling distribution is a constant, i.e. $T_{\text{displace}}(s, s') = 1/(NV)$. The acceptance probability is given by Eq. (5.32) where ΔU must be computed over the full trajectory.

Displacement moves are important during equilibration and in the more classical, high temperature regimes. In the quantum regime, it suffers either from small acceptance ratios or small achievable displacement vectors. Here, displacement should be attempted rarely as the move comes with a high computational cost. One may also displace a multi-particle exchange cycle, but the cost to performance ratio is even worse.

5.3.4 Permutation Sampling

If quantum exchange is important, staging or bisection alone is not sufficient as neither samples permutation space. An additional specialized move is necessary for this task. Changing the permutation state involves two particles at the very least. In principle, one can sample the full permutation space using only pair exchanges.

To sample a pair exchange, one simultaneously cuts two trajectories and regrows them after an exchange of the fixed endpoints. The regrowth itself can be done with staging, bisectioning, or any other suited sampling algorithm. For any free-particle sampling method, the sampling distribution is equivalent to [cf. Eq. (5.34)]

$$T_{\text{pair}}(s, s') = T_{\text{pick}} \prod_{k=1}^2 \frac{1}{\rho_0(\mathbf{r}_{k,0}, \mathbf{r}'_{k,P}; P\tau)} \prod_{\alpha=1}^P \rho_0(\mathbf{r}'_{k,\alpha}, \mathbf{r}'_{k,\alpha+1}; \tau), \quad (5.41)$$

where $\mathbf{r}_{k,\alpha}$ denotes the α^{th} bead in the trajectory of the k^{th} particle. Due to fixed initial endpoints, one has $\mathbf{r}'_{k,0} = \mathbf{r}_{k,0}$ but $\mathbf{r}'_{1,P} = \mathbf{r}_{2,P}$ and $\mathbf{r}'_{2,P} = \mathbf{r}_{1,P}$ for the fixed exchanged endpoints. Without further restraints, T_{pick} denotes the probability to pick any pair of particles, an initial time-slice and number of links, i.e.

$$T_{\text{pick}} = \frac{2}{N(N-1)M(P_{\text{max}}-1)}. \quad (5.42)$$

In this case, only the inter-action difference determines the acceptance probability of this move [cf. Eq. (5.32) and Eq. (5.37)].

While the above will sample permutation space theoretically, one enjoys very small acceptance ratios and, thus, poor performance in practice. Assuming that particle exchanges are likely at all – which is certainly not the general case – the main other reason lies in the naïve way how the pair of particles is chosen as the success of an attempt strongly correlates with the spatial distance of the endpoints. The general approach for improvement is an implementation of permutation sampling as multi-level move. Here, in a prelude step (level), one picks [cf. Eq. (5.42)] and tests a pair under certain constraints, so the move can be rejected before one did the actual sampling in a second step. As with any multi-level move, the rules on choosing and testing a pair (or cyclic exchanges of more particles) are arbitrary as long as the full move satisfies detailed balance [cf. Appx. D.2]. Details on different methods can be found, e.g., in [89, 99].

5.4 Worm-Algorithm

Permutation sampling is actually the soft spot of the PIMC method. The simulation of properties that are most directly affected by quantum exchanges suffers from a

very unfavorable scaling of required computer time with system size. This hurdle seems difficult to conquer within conventional PIMC, and more generally within any Monte Carlo scheme formulated in the canonical ensemble.

This complication is overcome with the *Worm-Algorithm* (WA) which has been adapted to continuous space models by Boninsegni *et al.* [106, 107]. In contrast to PIMC, the method works with the grand-canonical ensemble, i.e. the system is connected to a particle reservoir so that the particle number N in the system fluctuates. Consequently, in order to specify the thermodynamic state of the system, one needs to assign the chemical potential μ , as well as the temperature $\beta = 1/(k_B T)$ and the volume V . Additionally, the WA operates in an extended configurational space which encompasses the usual closed-loop configurations (referred to as Z sector or *diagonal configurations*) and configurations containing an additional open trajectory being the eponymous *worm*. The latter are called G sector or *off-diagonal configurations*. States in G contribute to the one-particle *Matsubara Green function* while only states in Z contribute to the (grand-canonical) partition function. Due to

$$Z = \text{Tr} e^{-\beta(\hat{H} - \mu\hat{N})} = \sum_N Z_N e^{\beta\mu N}, \quad (5.43)$$

one may also compute canonical averages by taking only those Z_N configurations which have a specific particle number N .

The Z sector of the WA configuration space is nothing but the full configuration space of conventional PIMC. It emerges from the path-integral representation of the grand-canonical density matrix $\hat{\rho}_{\text{gc}}$ corresponding to the sum over canonical density-matrices $\rho_N(R, R'; \beta)$ weighted with the *fugacity* $z = e^{\beta\mu N}$.

G sector configurations are made up of a single open-ended trajectory in addition to the many-particle background. They are described by the one-particle Matsubara Green function, i.e.

$$G(\mathbf{r}_1, \mathbf{r}_2; \beta_1 - \beta_2) = \left\langle \mathcal{T}[\hat{\psi}(\mathbf{r}_1, \beta_1)\hat{\psi}^\dagger(\mathbf{r}_2, \beta_2)] \right\rangle = \frac{1}{Z} g(\mathbf{r}_1, \mathbf{r}_2; \beta_1 - \beta_2), \quad (5.44)$$

where $\hat{\psi}^\dagger$ and $\hat{\psi}$ are the particle creation and annihilation field-operators, respectively, and \mathcal{T} denotes the (imaginary) time-order operator. In path-integral representation, the unnormalized $g(\mathbf{r}_{\mathcal{I}}, \mathbf{r}_{\mathcal{M}}; P\tau)$ (with $P \in \mathbb{N}$) describes the creation of a particle at $\mathbf{r}_{\mathcal{M}}$ (*Masha*), its propagation for P imaginary-time steps and annihilation at $\mathbf{r}_{\mathcal{I}}$ (*Ira*). This open-ended string of beads makes up the worm. All time-slices touched by the worm contain an additional particle and since P need not be an integer multiple of the total number of time-slices M , configuration in the G sector may have an effective fractional particle number on the whole.

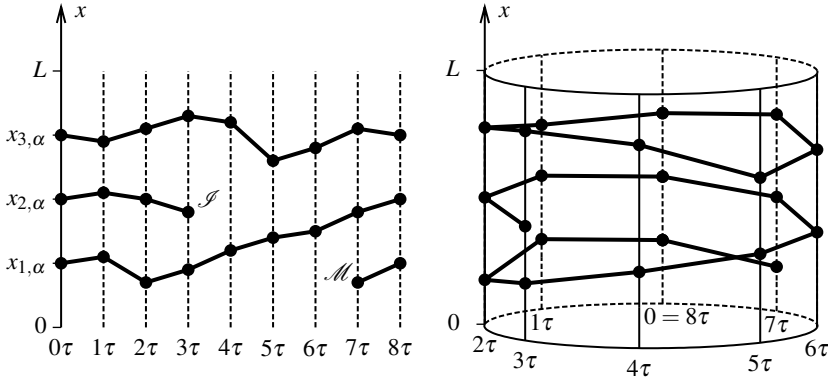


Figure 5.3 Illustration of an off-diagonal configuration (G sector). One of the three single-particle trajectories [see Fig. 5.1] is cut open creating the open-ended worm propagating from \mathcal{M} to \mathcal{I} . There are three time-slices which each contain one bead less. But, the worm itself may wrap multiple times around the β -cylinder and effectively represent several particles.

Formally, the ensemble of all configurations corresponds to the generalized partition function

$$Z_{\text{WA}} = Z + Z' , \quad (5.45)$$

with

$$Z' = C \sum_{j_{\mathcal{I}}, j_{\mathcal{M}}} \int d\mathbf{r}_{\mathcal{I}} d\mathbf{r}_{\mathcal{M}} g(\mathbf{r}_{\mathcal{I}}, \mathbf{r}_{\mathcal{M}}; (j_{\mathcal{I}} - j_{\mathcal{M}})\tau) , \quad (5.46)$$

where C is a dimensionless constant. C does not enter into thermal averages and can be set to any value. It purely affects the relative statistics of Z and G -sectors, i.e. how many G configurations are sampled for each Z configuration.

As before, the partition function is unknown, so individual configurations are constructed by a Markov-chain. To do so, one must devise new moves to sample the additional degrees of freedom. Although one may keep the usual PIMC updates for manipulating Z configurations, the original WA [106] traverses the full configuration space by creating, destroying and manipulating the worm *exclusively*.

A striking difference to conventional PIMC is that the number of coordinates across individual configurations is not constant. Since each move which changes the number of coordinates is not self-adjoint, it must have a partner for the reverse step. The complementary pair as a whole satisfies detailed balance. Consequently, instead of choosing a move one now chooses a pair. The final result does

not depend on the global probability of addressing each pair, as long as the specific moves within a pair are chosen uniformly. This is assumed in the acceptance probabilities presented below.

5.4.1 Open/Close

The first method to introduce a worm is to select a bead at random and remove the next P links of the single-particle trajectory. The chosen bead, \mathbf{r}_0 , is the head (\mathcal{M}) and \mathbf{r}_P the tail (\mathcal{I}) of the new worm. This move is called *open* and switches from the Z to the G -sector. Its sampling distribution is simply

$$T_{\text{open}}(s_Z, s'_G) = \frac{1}{NMP_{\text{max}}} , \quad (5.47)$$

where P_{max} denotes the maximum number of links which can be removed at once, i.e. $1 \leq P \leq P_{\text{max}}$. For the complementary move, *close*, one samples P free-particle links from $\mathbf{r}_{\mathcal{M}}$ to $\mathbf{r}_{\mathcal{I}}$. The natural choice of the sampling method is *staging* from Sec. 5.3.1, but any other method is fine. Thus, one has

$$T_{\text{close}}(s_G, s'_Z) = \frac{1}{\rho_0(\mathbf{r}_0, \mathbf{r}_P; P\tau)} \prod_{\alpha=1}^P \rho_0(\mathbf{r}'_{\alpha-1}, \mathbf{r}'_{\alpha}; \tau) , \quad (5.48)$$

with $\mathbf{r}_0 = \mathbf{r}_{\mathcal{M}}$ and $\mathbf{r}_P = \mathbf{r}_{\mathcal{I}}$. These beads are unique within any G configuration, so the leading factor of Eq. (5.34) drops out. Note that with respect to *open*, one is only allowed to sample up to P_{max} links. If $t_{\mathcal{I}} - t_{\mathcal{M}} > P_{\text{max}}\tau$, *close* is rejected in any case.

With Eq. (5.26), the acceptance probabilities read

$$A_{\text{open}}(s_Z, s'_G) = \min \left[1, \frac{CNMP_{\text{max}}}{\rho_0(\mathbf{r}'_{\mathcal{I}}, \mathbf{r}'_{\mathcal{M}}, P\tau)} e^{-\Delta U - P\mu\tau} \right] , \quad (5.49)$$

$$A_{\text{close}}(s_G, s'_Z) = \min \left[1, \frac{\rho_0(\mathbf{r}_{\mathcal{I}}, \mathbf{r}_{\mathcal{M}}, P\tau)}{CNMP_{\text{max}}} e^{-\Delta U + P\mu\tau} \right] , \quad (5.50)$$

where $\Delta U = U(s') - U(s)$ denotes the inter-action difference between new and old configuration and N refers to the number of particles in the corresponding Z sector, i.e. before opening and after closing. The factor $e^{P\mu\tau}/C$ appears from the ratio of the grand-canonical weights $\pi(s_Z)/\pi(s_G)$. Aside from the arbitrary constant C , it accounts for the energy difference when changing the number of links in the system.

5.4.2 Insert/Remove

Instead of introducing a worm by removing a trajectory piece, one may simply *insert* a new worm from scratch. To do so, one selects a random time-slice on

which one samples the position of $\mathbf{r}'_{\mathcal{M}} = \mathbf{r}'_0$ uniformly in V and grows a trajectory of $1 \leq P \leq P_{\max}$ links on its head. Since, \mathbf{r}_P is not fixed a priori one has the sampling distribution

$$T_{\text{insert}}(s_Z, s'_G) = \frac{1}{VM P_{\max}} \prod_{\alpha=1}^P \rho_0(\mathbf{r}'_{\alpha-1}, \mathbf{r}'_{\alpha}; \tau). \quad (5.51)$$

Remove involves no randomness at all, i.e.

$$T_{\text{remove}}(s_G, s'_Z) = 1, \quad (5.52)$$

although this move is automatically rejected if the worm has more than P_{\max} links.

With Eq. (5.26) the acceptance probabilities are

$$A_{\text{insert}}(s_Z, s'_G) = \min \left[1, CVM P_{\max} e^{-\Delta U + P\mu\tau} \right], \quad (5.53)$$

$$A_{\text{remove}}(s_G, s'_Z) = \min \left[1, \frac{1}{CVM P_{\max}} e^{-\Delta U - P\mu\tau} \right], \quad (5.54)$$

where $\Delta U = U(s') - U(s)$ is the inter-action difference between new and old configuration.

One can choose the constant C and the maximum number of links P_{\max} to balance moves between the G sector and the Z sector. The natural choice,

$$C \sim \frac{1}{VM P_{\max}}, \quad P_{\max} \sim \frac{1}{2\lambda\tau} = \frac{M}{2\lambda\beta}, \quad (5.55)$$

guarantees that no macroscopically large factors arise in the acceptance probabilities of *open*, *close*, *insert* and *remove*.

5.4.3 Advance/Recede

Another possibility to effectively change the particle number but without leaving the G -sector is to lengthen the worm by sampling a new trajectory piece of P links on its head. This move is called *advance* and its counterpart *recede*. *Advance* is very similar to *insert*, except that one does not need to sample the initial bead. *Recede* differs from *remove* as one has the freedom to remove any number of $1 \leq P \leq P_{\max}$ links. The sampling distributions read

$$T_{\text{advance}}(s_G, s'_G) = \frac{1}{P_{\max}} \prod_{\alpha=1}^P \rho_0(\mathbf{r}'_{\alpha-1}, \mathbf{r}'_{\alpha}; \tau), \quad (5.56)$$

$$T_{\text{recede}}(s_G, s'_G) = \frac{1}{P_{\max}}, \quad (5.57)$$

where, for *advance*, one has $\mathbf{r}'_0 = \mathbf{r}_{\mathcal{I}}$ and $\mathbf{r}'_P = \mathbf{r}'_{\mathcal{I}}$. *Recede* is rejected if the worm has only P or fewer links. The acceptance probabilities are simply

$$A_{\text{advance}}(s_G, s'_G) = \min \left[1, e^{-\Delta U + P\mu\tau} \right], \quad (5.58)$$

$$A_{\text{recede}}(s_G, s'_G) = \min \left[1, e^{-\Delta U - P\mu\tau} \right]. \quad (5.59)$$

5.4.4 Swap

Although *advance* and *recede* can change the per Permutation sampling can be very effectively realized in the G -sector. First, one chooses a random bead, \mathbf{r}_0 , located on the same time-slice as the head of the worm $\mathbf{r}_{\mathcal{I}}$. Then, one deletes the next $P = P_{\text{max}}$ links from \mathbf{r}_0 up to \mathbf{r}_P and reconnects $\mathbf{r}_{\mathcal{I}}$ to \mathbf{r}_P with a newly sampled trajectory piece. This self-adjoint move is called *swap*.

The sampling distribution reads

$$T_{\text{swap}}(s_G, s'_G) = \frac{1}{N} \frac{1}{\rho_0(\mathbf{r}_{\mathcal{I}}, \mathbf{r}_P; P\tau)} \prod_{\alpha=1}^P \rho_0(\mathbf{r}'_{\alpha-1}, \mathbf{r}'_{\alpha}; \tau), \quad (5.60)$$

with $\mathbf{r}'_0 = \mathbf{r}_{\mathcal{I}}$ and $\mathbf{r}'_P = \mathbf{r}_P$. The swapped head of the worm gives rise to a kinetic action contribution in the acceptance probability,

$$A_{\text{swap}}(s_G, s'_G) = \min \left[1, \frac{\rho_0(\mathbf{r}_0, \mathbf{r}_P; P\tau)}{\rho_0(\mathbf{r}_{\mathcal{I}}, \mathbf{r}_P; P\tau)} e^{-\Delta U} \right]. \quad (5.61)$$

One can significantly improve the acceptance ratio by selecting only swaps which minimize the impact of the kinetic contribution, see e.g. [106]. This puts spatial restraints on the initial selection converting *swap* to a local move. As such, it enjoys high acceptance ratios similar to those of *advance/recede*. Note that the latter two also change the permutation state if the worm length crosses an integer multiple of M .

5.5 Estimators

With a PIMC or a WA simulation, one generates path configurations s up to some total S . In order to compute thermal averages, one needs to express a given quantum expectation $\langle \hat{A} \rangle$ [Eq. (2.10)] as an average over paths. Ultimately, one records individual measurements A_i and estimates the thermal expectation as an arithmetic average,

$$\langle \hat{A} \rangle \approx \bar{A} = \frac{1}{S} \sum_{i=1}^S A_i, \quad A_i \equiv A(s_i). \quad (5.62)$$

The specific formula which is used to obtain \bar{A} is called *estimator*. There are usually different estimators for the same thermal expectations.

In contrast to the non-random thermal average \hat{A} , every \bar{A} is only an estimation of the former and as such a fluctuating quantity. One can easily show that the standard statistical error of the mean is

$$\varepsilon_{\bar{A}} = \frac{\sigma_A}{\sqrt{S}}(1 + 2\tau_A) , \quad \tau_A = \frac{1}{\sigma_A} \sum_{k=1}^{\infty} \overline{(A_0 - \bar{A})(A_k - \bar{A})} \quad (5.63)$$

where σ_A^2 is the variance of the A_i and τ_A the (*integrated*) *auto-correlation time*. There are further errors from various sources. In summary, every estimator is characterized by its *systematic bias*, *time-step error* (due to finite M), *finite-size error* (due to finite N and V), *statistical error* (due to finite S) and *efficiency* (robustness to temporal correlations of the Markov chain).

For an observable \hat{A} which are diagonal in the coordinate representation used by PIMC, there is always a straightforward method to construct an estimator since one can compute $A(R_\alpha)$ on any time-slice α . The estimator is given by a simple average over paths [cf. Eq. (2.10)], i.e.

$$\bar{A} = \langle A(R_\alpha) \rangle_Z \equiv \frac{1}{S} \sum_{s \in Z} A(R_\alpha) , \quad (5.64)$$

where $s \in Z$ denotes a configuration in the ensemble given by Z . One may replace $A(R_\alpha)$ with the average over time-slices which improves statistics. In the following – to keep the notation simple – such optional averaging is not explicitly noted. All bead indices refer to positions within the same time-slice (with the exception of $\mathbf{r}_{\mathcal{I}}$ and $\mathbf{r}_{\mathcal{M}}$ which are unique).

Furthermore, the diagonality allows to construct *local* estimators. The typical example is the local density estimator

$$n(\mathbf{r}) = \frac{1}{V} \left\langle \sum_{j=1}^N \delta(\mathbf{r} - \mathbf{r}_j) \right\rangle_{Z_N} , \quad (5.65)$$

where V denotes the volume. Such estimators usually require some means to compute functions like $\delta(\mathbf{r} - \mathbf{r}_j)$). This is typically solved by collecting statistics to finite-size spatial bins at the expense of an additional systematic error. In some cases, one may devise more elaborate schemes to circumvent this problem.

Other commonly computed quantities include the *pair distribution function*

$$g(\mathbf{r}) = \left\langle \frac{1}{N^{\mathcal{P}}} \sum_{j < k}^N \delta(\mathbf{r} - (\mathbf{r}_j - \mathbf{r}_k)) \right\rangle_{Z_N} , \quad N^{\mathcal{P}} = \frac{N(N-1)}{2} , \quad (5.66)$$

and the (*hexagonal*) *bond-order correlation function*

$$g_6(\mathbf{r}) = \frac{1}{g(\mathbf{r})} \left\langle \frac{1}{N^{\text{P}}} \sum_{j < k}^N G_j^* G_k \delta(\mathbf{r} - (\mathbf{r}_j - \mathbf{r}_k)) \right\rangle_{Z_N}, \quad G_j = \frac{1}{N_j^{\text{nb}}} \sum_{l=1}^{N_j^{\text{nb}}} e^{i6\phi_{jl}}, \quad (5.67)$$

where G_j is the *local bond order parameter* of the j^{th} particle. The complex valued G_j is computed from the N_j^{nb} neighboring particles (within some defined radius) where ϕ_{jl} denotes the angle of the connecting line to the l^{th} neighbor with respect to some fixed axis.

If sampling the off-diagonal G -sector with WA, one can estimate the *Matsubara Green function* with

$$g_{\text{M}}(\mathbf{r}, \tau) = \langle \delta(\tau - (\tau_{\text{I}} - \tau_{\text{M}})) \delta(\mathbf{r} - (\mathbf{r}_{\text{I}} - \mathbf{r}_{\text{M}})) \rangle_G. \quad (5.68)$$

A better estimator is given in [106].

There is another general approach if the thermal expectation $\langle \hat{A} \rangle$ can be written as derivative of the partition function. Applying the derivative to a single link of the path-integral yields

$$\frac{d}{dx} \rho(R_{\alpha-1}, R_{\alpha}; \tau) = -\rho(R_{\alpha-1}, R_{\alpha}; \tau) \frac{d}{dx} S_{\alpha}, \quad (5.69)$$

where S_{α} denotes the exact link action [cf. Eq. (5.4)]. Hence, an estimator of $\langle \hat{A} \rangle$ can be constructed by

$$\langle \hat{A} \rangle = -\frac{1}{Z} \frac{dZ}{dx} = M \left\langle \frac{d}{dx} S_{\alpha} \right\rangle_{Z_N}, \quad (5.70)$$

where, on average, the sum over all link equals M single-link contributions due to the symmetry in imaginary-time. This simplification can be omitted in order to improve statistics. Equation (5.70) is especially useful for quantities which are not diagonal in coordinate representation.

The prime example is the *thermodynamic estimator* of the energy which is obtained by differentiating Z with respect to the inverse temperature, i.e.

$$E_{\text{th}} = -\frac{1}{Z} \frac{dZ}{d\beta} = \left\langle \frac{d}{d\tau} S_{\alpha} \right\rangle_{Z_N} = \left\langle \frac{dN}{2\tau} - \frac{(R_{\alpha-1} - R_{\alpha})^2}{2\lambda\tau^2} + \frac{dU_{\alpha}}{d\tau} \right\rangle_{Z_N}, \quad (5.71)$$

where the derivative of the kinetic action was inserted in the last step [cf. (5.5)]. In the high-temperature limit $\tau \rightarrow 0$, the first two terms are the kinetic energy and the last is the potential energy since U reduces to τV [cf. (5.9)].

Herman *et al.* [108] noted that E_{th} behaves poorly near classical limit. The reason is due to the troublesome behavior of the kinetic energy contributions if M is fixed while letting τ get small. This can be circumvented with the *virial energy estimator* defined as [89]

$$E_v = \left\langle \frac{dN}{2L\tau} - \frac{(R_{\alpha-L} - R_\alpha)(R_{\alpha-1} - R_\alpha)}{2\lambda L\tau^2} - \frac{1}{2}F_\alpha \cdot \Delta_\alpha + \frac{dU_\alpha}{d\tau} \right\rangle_{Z_N}, \quad (5.72)$$

where

$$F_\alpha = -\frac{1}{\tau} \nabla_{R_\alpha} [U_{\alpha-1} - U_\alpha] \quad (5.73)$$

is the *generalized force* – which converges to the classical force when inserting the primitive action – and

$$\Delta_\alpha = R_\alpha - \frac{1}{2L} \sum_{\beta=0}^{L-1} (R_{\alpha-\beta} + R_{\alpha+\beta}) \quad (5.74)$$

is the displacement of the particles' positions from their imaginary-time averages within the window L , $1 \leq L \leq M$.

The size of the window determines the behavior of the virial estimator. If $L = 1$, the force term drops from E_v leaving exactly E_{th} . If $L = M$, the troublesome second term vanishes unless there are permutations, i.e. $R_{\alpha+M} \neq R_\alpha$, which are, however, unlikely in the critical near classical limit. If they do appear, the second term describes (approximately) the energy contribution of bosonic particle exchanges.

Lastly, a particularly appealing property of PIMC simulations is the possibility to compute the superfluid fraction γ_s , i.e. the fraction of the total density which does not respond to slow movements of the confinement. In the rotating bucket experiment [109], the superfluid will stay at rest while the normalfluid rotates rigidly with the walls. The smaller rotating mass reduces the effective moment of inertia I_{qm} . The measured deviation to the classically expected value I_{cl} leads to very simple yet effective way to obtain γ_s

$$\gamma_s = \frac{n_s}{n} = 1 - \frac{I_{\text{qm}}}{I_{\text{cl}}}. \quad (5.75)$$

This effect is known as *non classical rotational inertia* (NCRI). It is directly linked to the presence of off-diagonal long-range order (ODLRO) [110], a concept introduced by Yang [6]. As such, the superfluid fraction must be estimated from the full path configuration and cannot be computed from individual time slices or links.

The work done is $E = I_{\text{qm}}\omega^2/2$, where ω is the angular velocity. In linear response theory, I_{qm} can be defined as the work done by an infinitesimally small

rotation rate, i.e.

$$I_{\text{qm}} = \left. \frac{dF}{d\omega^2} \right|_{\omega=0} = \left. \frac{d\langle \hat{L}_z \rangle}{d\omega} \right|_{\omega=0} \quad \hat{L}_z = i\hbar \sum_{i=0}^N \frac{\partial}{\partial \phi_i}, \quad (5.76)$$

where F is the free energy, \hat{L}_z is the total angular momentum operator in z -axis and ϕ_i is the angular coordinate in cylindrical coordinates of the i^{th} particle.

Statistical mechanics do not require the use of an inertial reference frame. Hence, in order to derive an estimator for I_{qm} , one considers the system in the frame rotating with the bucket. The Hamiltonian is simply given by $\hat{H}_\omega = \hat{H}_0 - \omega \hat{L}_z$ where \hat{H}_0 is the Hamiltonian at rest. The details of how to derive a path-integral expression for Eq. (5.76) with this Hamiltonian are discussed in [89]. In the end, one arrives at [111]

$$\gamma_s = \frac{2m \langle A_z^2 \rangle}{\beta \lambda I_{\text{cl}}}, \quad (5.77)$$

where two functions of a given path are introduced, namely the projected area

$$\mathbf{A} = \frac{1}{2} \sum_{j=1}^N \sum_{\alpha=1}^M \mathbf{r}_{j,\alpha-1} \times \mathbf{r}_{j,\alpha}, \quad (5.78)$$

and the classical moment of inertia

$$I_{\text{cl}} = \left\langle \sum_{j=1}^N \sum_{\alpha=1}^M m_j \mathbf{r}_{j,\alpha-1}^\perp \cdot \mathbf{r}_{j,\alpha}^\perp \right\rangle, \quad (5.79)$$

where m_j is the mass and $\mathbf{r}_{j,\alpha}^\perp$ is the projected position of the j^{th} bead on the α^{th} time-slice. Note that due to the symmetry of \mathbf{A} its average, $\langle \mathbf{A} \rangle$, vanishes.

Equation (5.77) is referred to as *area formula* in literature [111]. It relates the superfluid fraction to the ratio of the covered area by the particle trajectories to the cross-sectional area of the whole system. It obviously emphasizes the importance of particle exchange, since a N -particle permutation trajectory naturally covers more area. Since single-particle paths also have a finite extension, they result in a non-bosonic contribution to superfluidity in finite systems [112]. If the size of the bucket is greater than the thermal wavelength, such contributions are negligible [89].

There is an elegant way to adapt the area formula to macroscopic systems simulated as rectangular confinements with periodic boundary conditions. Consider a superfluid confined in a thin annulus of width d with a mean radius $R \gg d$. The classical moment of inertia is $I_{\text{cl}} = mNR^2$. The area A can be written as $WR/2$ where the *winding number* W is defined as the flux of trajectories winding around the annulus times the circumference. Inserting these expressions into

Eq. (5.77) yields

$$\gamma_s = \frac{1}{2\lambda\beta} \frac{\langle W^2 \rangle}{N}, \quad \mathbf{W} = \sum_{j=1}^N \int_0^\beta dt \frac{d\mathbf{r}_j(t)}{dt}, \quad (5.80)$$

where the vectorized definition of the winding number takes the periodic boundary condition in all spatial directions into account. Equation (5.80) ignores any non-winding trajectories, since their contribution is $\mathcal{O}(R^{-2})$ and negligible for large R , i.e. for simulation boxes much larger than the thermal wavelength. One can derive Eq. (5.80) directly when calculating the response of the (periodic) system to a linear velocity of its walls, i.e. using the total momentum operator \hat{P} instead of \hat{L} [111].

PART III

Indirect Excitons

Modeling the Interaction of Indirect Excitons

Excitons are bound electron-hole pairs in semiconductors [26]. One can certainly simulate a composite gas of electrons and holes with the PIMC method presented in Ch. 5, but this only works reliably for a very small number of particles. The reason is the ubiquitous *fermion sign problem* which causes an exponential increase in the numerical complexity either when lowering the temperature, increasing the particle number, or increasing the correlation strength. In 2005, Troyer and Wiese have proven the sign problem to be NP-hard [113]. This implies that a full and generic solution of the sign problem would also solve all problems in the complexity class NP in polynomial time.

In order to circumvent the fermion sign problem, one has to introduce additional approximations. In the case of excitons, the obvious approach is to consider excitons as single entities. Since excitons are bosons, PIMC can accurately account for bosonic exchange symmetry with no further approximation [cf. Ch. 5]. The complexity of the original setup is hidden in an effective exciton interaction. This chapter details how this interaction is derived in case of spatially indirect excitons with a strong dipole moment. It mainly follows the method introduced by Filinov *et al.* [114], but goes beyond a purely numerical derivation.

6.1 Model

The importance of spatially indirect excitons has been emphasized in the introduction. The general idea is to confine electrons and holes into separate layers for which several possible experimental realization exist [33, 50, 51]. The model used here considers a single wide semiconductor quantum well (QW) of width L containing N_e electrons in the conduction band and N_h holes in the valence band

which are created by an optical pulse [50, 51]. Application of an electrostatic field of strength E perpendicular to the QW plane created allows to spatially separate electrons and holes to different edges of the QW. By varying E this separation can be changed between 0 and L giving rise to a variable dipole moment d .

The full Hamiltonian governing a system of N_e electrons and N_h holes reads

$$\hat{H} = \hat{H}_{\parallel} + \hat{H}_{\perp} + \hat{W} \quad (6.1)$$

with the parts

$$\hat{H}_{\parallel} = \sum_{\alpha \in \{e,h\}} \sum_{i=1}^{N_{\alpha}} \left[-\frac{\hbar^2}{2m_{\alpha}^{\parallel}} \nabla_{\mathbf{r}_i}^2 \right], \quad (6.2)$$

$$\hat{H}_{\perp} = \sum_{\alpha \in \{e,h\}} \sum_{i=1}^{N_{\alpha}} \left[-\frac{\hbar^2}{2m_{\alpha}^{\perp}} \frac{\partial^2}{\partial z_i^2} + V^{\text{QW}}(z_i) + V^{\text{E}}(z_i, E_z) \right], \quad (6.3)$$

$$\hat{W} = \sum_{i < j}^N \frac{q_i q_j}{\epsilon} \frac{1}{\sqrt{(\mathbf{r}_i - \mathbf{r}_j)^2 + (z_i - z_j)^2}}, \quad (6.4)$$

with $N = N_e + N_h$. The Hamiltonian is split into the out-of-plane \hat{H}_{\perp} and in-plane single particle contributions \hat{H}_{\parallel} and the two-body Coulomb interaction \hat{W} coupling the out-of-plane problem and the in-plane problem.

If the characteristic spacing of the quantized one-particle energy levels $\Delta\epsilon_i$ is much larger than the typical inter-particle interaction energy $U_{\alpha\beta}$, the dynamics of the latter take place on a larger time frame than the former. This satisfies the conditions for an adiabatic approximation explained in chapter 2.4.3: One can separate the out-of-plane motion of each hole and electron from the in-plane motion with the ansatz

$$\rho(\beta) = \rho_{\parallel}(\mathbf{r}_1, \dots, \mathbf{r}_N; \beta) \prod_{i=1}^{N_e} \rho_e(z_i; \beta) \prod_{j=1}^{N_h} \rho_h(z_j; \beta). \quad (6.5)$$

If the single particle density matrices $\rho_e(z; \beta)$ and $\rho_h(z; \beta)$ are known, one integrates the original Bloch equation over all out-of-plane coordinates yielding the reduced in-plane problem with the effective Hamiltonian

$$\hat{H}_{\parallel}^{\text{eff}} = \hat{H}_{\parallel} + \hat{W}_{\parallel}, \quad (6.6)$$

with the new in-plane interaction \hat{W}_{\parallel} reading in coordinate representation

$$\hat{W}_{\parallel} = \sum_{i < j}^{N_e} V_{ee}(r_{ij}) + \sum_{i < j}^{N_h} V_{hh}(r_{ij}) + \sum_{i=1}^{N_e} \sum_{j=1}^{N_h} V_{eh}(r_{ij}), \quad (6.7)$$

where each term represents a smoothed, particle species dependent Coulomb potential obtained by integrating out the out-of-plane density distribution, i.e.,

$$V_{\alpha\beta}(r; \beta) = \frac{q_\alpha q_\beta}{\epsilon} \int dz dz' \frac{\rho_\alpha(z; \beta) \rho_\beta(z'; \beta)}{\sqrt{r^2 + (z - z')^2}}, \quad \alpha, \beta = \text{h, e}. \quad (6.8)$$

In the following, Greek indices denote the particle species, electron (e) or hole (h), and Roman indices label individual particles.

The actual work lies in finding the single particle density matrices $\rho_\alpha(z; \beta)$. These can be computed by solving the 1D single particle problem in a quantum well with an applied electric field. There are several methods to choose from, the list includes PIMC simulations or a direct numerical computation via matrix squaring (see chapter 4.2). The section 6.3 discusses the solution of the quantum well Bloch equation in detail.

While the Hamiltonian (6.6) hides the out-of-plane complexity in an effective in-plane interaction potential, it still describes a system of individual electrons and holes. A PIMC simulation of such a system is only feasible if one neglects the fermionic nature of the particles. However, electrons and holes may form bound pairs called *excitons* under certain conditions. Excitons are compound bosons and PIMC is perfectly capable of handling bosonic exchanges.

The existence of excitons requires that its binding energy E_X is much larger than the thermal energy $k_B T$ and the effective exciton-exciton interaction V_{XX} . The effective exciton *dipole moment* d follows directly from the electron and hole densities, $\rho_e(z; \beta)$ and $\rho_h(z; \beta)$:

$$d = \langle z_e \rangle - \langle z_h \rangle = \int dz z \rho_e(z; \beta) - \int dz' z' \rho_h(z'; \beta). \quad (6.9)$$

The electron \mathbf{r}^e and hole coordinates \mathbf{r}^h are dropped in favor of a more suitable set describing the exciton center-of-mass position \mathbf{R} and its internal electron hole separation \mathbf{r}^{eh} , i.e. $(\mathbf{r}_i^e, \mathbf{r}_i^h) \rightarrow (\mathbf{R}_i, \mathbf{r}_i^{\text{eh}})$ for all $i = 1, \dots, N_X$. Electrical neutrality is assumed, i.e. $N_X \equiv N_e = N_h$. The coordinates transform according to

$$\left. \begin{aligned} \mathbf{r}^h &= \mathbf{R} + \frac{m_e^{\parallel}}{M_X} \mathbf{r}^{\text{eh}}, \\ \mathbf{r}^e &= \mathbf{R} - \frac{m_h^{\parallel}}{M_X} \mathbf{r}^{\text{eh}}, \end{aligned} \right\} \iff \left\{ \begin{aligned} \mathbf{R} &= \frac{m_e^{\parallel}}{M_X} \mathbf{r}^e + \frac{m_h^{\parallel}}{M_X} \mathbf{r}^h, \\ \mathbf{r}^{\text{eh}} &= \mathbf{r}^e - \mathbf{r}^h, \end{aligned} \right. \quad (6.10)$$

where $M_X = m_e^{\parallel} + m_h^{\parallel}$ is the exciton mass. With these new coordinates, the Hamiltonian (6.6) is split into a center-of-mass \hat{H}_{cm} , a relative \hat{H}_{rel} , and a coupling term \hat{W} , i.e.

$$\hat{H}_{\parallel}^{\text{eff}} = \hat{H}_{\text{cm}} + \hat{H}_{\text{rel}} + \hat{W}, \quad (6.11)$$

with

$$\hat{H}_{\text{cm}} = \sum_{i=1}^{N_X} \left[-\frac{\hbar^2}{2M_X} \nabla_{\mathbf{R}_i}^2 \right], \quad (6.12)$$

$$\hat{H}_{\text{rel}} = \sum_{i=1}^{N_X} \left[-\frac{\hbar^2}{2\mu} \nabla_{\mathbf{r}_i^{\text{eh}}}^2 + V_{\text{eh}}(r_i^{\text{eh}}; \beta) \right], \quad (6.13)$$

$$\hat{W} = \sum_{i<j}^{N_X} \left[V_{\text{ee}}(|\mathbf{r}_i^{\text{e}} - \mathbf{r}_j^{\text{e}}|) + V_{\text{hh}}(|\mathbf{r}_i^{\text{h}} - \mathbf{r}_j^{\text{h}}|) + V_{\text{eh}}(|\mathbf{r}_i^{\text{e}} - \mathbf{r}_j^{\text{h}}|) \right], \quad (6.14)$$

where $\mu = m_{\text{e}}^{\text{ll}} m_{\text{h}}^{\text{ll}} / M_X$ is the reduced mass. Note that the relative Hamiltonian picks up those terms from the effective in-plane potential (6.8) where electron and hole coordinates belong to the same exciton.

The assumed energy relation $E_X \gg V_{\text{XX}}$ paves the road for another adiabatic approximation, this time within the 2D plane. Consider the ansatz

$$\rho_{\parallel}(\mathbf{r}_1^{\text{e}}, \dots, \mathbf{r}_{N_{\text{e}}}^{\text{e}}, \mathbf{r}_1^{\text{h}}, \dots, \mathbf{r}_{N_{\text{h}}}^{\text{h}}; \beta) = \rho(\mathbf{R}_1, \dots, \mathbf{R}_{N_X}; \beta) \prod_{i=1}^{N_X} \rho_X(r_i^{\text{eh}}; \beta). \quad (6.15)$$

Again following the approximation procedure and integrating over all internal relative degrees of freedom r^{eh} yields the effective exciton Hamiltonian \hat{H}_X^{eff}

$$\hat{H}_X^{\text{eff}} = \sum_{i=1}^{N_X} \frac{\hbar^2}{2M_X} \nabla_{\mathbf{R}_i}^2 + \sum_{i<j}^{N_X} V_{\text{XX}}(R_{ij}), \quad (6.16)$$

with the center-of-mass distance $R_{ij} \equiv |\mathbf{R}_i - \mathbf{R}_j|$ and the effective exciton interaction $V_{\text{XX}}(R_{ij})$, which is given by

$$V_{\text{XX}}(R_{ij}) = \sum_{\alpha, \beta = \text{e, h}} \int d^2 \mathbf{r}_i^{\text{eh}} d^2 \mathbf{r}_j^{\text{eh}} V_{\alpha\beta}(|\mathbf{r}_i^{\alpha} - \mathbf{r}_j^{\beta}|; \beta) \rho_X(r_i^{\text{eh}}; \beta) \rho_X(r_j^{\text{eh}}; \beta), \quad (6.17)$$

where each \mathbf{r}_i^{α} refers to the coordinates of the i^{th} excitons' component α , namely the electron $\alpha = \text{e}$ or hole $\alpha = \text{h}$. These may be expressed in terms of the integration variables as

$$\mathbf{r}_1^{\text{h}} - \mathbf{r}_2^{\text{h}} = \mathbf{R}_1 - \mathbf{R}_2 + \frac{m_{\text{e}}^{\text{ll}}}{M_X} (\mathbf{r}_1^{\text{eh}} - \mathbf{r}_2^{\text{eh}}), \quad (6.18)$$

$$\mathbf{r}_1^{\text{e}} - \mathbf{r}_2^{\text{e}} = \mathbf{R}_1 - \mathbf{R}_2 - \frac{m_{\text{h}}^{\text{ll}}}{M_X} (\mathbf{r}_1^{\text{eh}} - \mathbf{r}_2^{\text{eh}}), \quad (6.19)$$

$$\mathbf{r}_1^{\text{h}} - \mathbf{r}_2^{\text{e}} = \mathbf{R}_1 - \mathbf{R}_2 + \frac{m_{\text{e}}^{\text{ll}}}{M_X} \mathbf{r}_1^{\text{eh}} + \frac{m_{\text{h}}^{\text{ll}}}{M_X} \mathbf{r}_2^{\text{eh}}. \quad (6.20)$$

The required density matrix $\rho_X(r^{\text{eh}}; \beta)$ solves the single exciton Bloch equation for Eq. (6.13). This problem and the computation of the final exciton interaction are discussed in Sec. 6.4.

6.2 The Classical Approximation

Above derivation recovers the classical exciton potential for point-like charges. In order to show this, one assumes an electron-hole layer separation of d and sets the corresponding densities

$$\rho_e(z; \beta) = \delta(z - d) , \quad \rho_h(z; \beta) = \delta(z) . \quad (6.21)$$

Insertion into Eq. (6.9) validates this ansatz. The in-plane interaction for singly charged pair of particles with $e \equiv q_h = -q_e$ can then be directly read of Eq. (6.8):

$$V_{eh}^{\text{cl}}(r; \beta) = V_{he}^{\text{cl}}(r; \beta) = -\frac{e^2}{\epsilon} \frac{1}{\sqrt{r^2 + d^2}} , \quad (6.22)$$

$$V_{eh}^{\text{cl}}(r; \beta) = V_{he}^{\text{cl}}(r; \beta) = \frac{e^2}{\epsilon} \frac{1}{r} . \quad (6.23)$$

In the classical picture of a bound pair, the electron is sitting directly atop the hole, so the in-plane distance of the two is zero. This motivates the ansatz for the exciton density distribution

$$\rho_X(\mathbf{r}; \beta) = \delta(\mathbf{r}) . \quad (6.24)$$

Using this and Eq. (6.23) in Eq. (6.17) yields the classical exciton interaction potential

$$V_{XX}^{\text{cl}}(R; \beta) = \sum_{\alpha, \beta=e, h} V_{\alpha\beta}^{\text{cl}}(R; \beta) = \frac{e^2}{\epsilon} \left[\frac{2}{R} - \frac{2}{\sqrt{R^2 + d^2}} \right] . \quad (6.25)$$

The most noticeable implication of the classical model (6.25) is its mass independence. The semiconductor material enters only as a dielectric but does not affect the systems physics. This is easy to see when considering a reduced Hamiltonian in effective atomic units – all material differences are then hidden in the renormalization of length and energy scales.

However, the model (6.25) is an improvement over a pure dipole approximation for the exciton interaction. This approximation remains valid in the $R \gg d$ case. Deviations occur when the exciton spacing falls below the dipole moment, i.e. $R \lesssim d$. The excitons feel their compound nature and recover a Coulomb-like interaction in the $R \ll d$ case. In summary, the limiting cases of Eq. (6.25) read

$$V_{XX}^{\text{cl}}(R; \beta) \xrightarrow{R \rightarrow 0} \frac{e^2}{\epsilon} \frac{2}{R} , \quad V_{XX}^{\text{cl}}(R; \beta) \xrightarrow{R \rightarrow \infty} \frac{e^2}{\epsilon} \frac{d^2}{R^3} . \quad (6.26)$$

The factor of 2 in the Coulomb limit accounts for the two simultaneous electron-electron and hole-hole repulsions. Figure 6.1 shows the model interaction (6.25) and its limits.

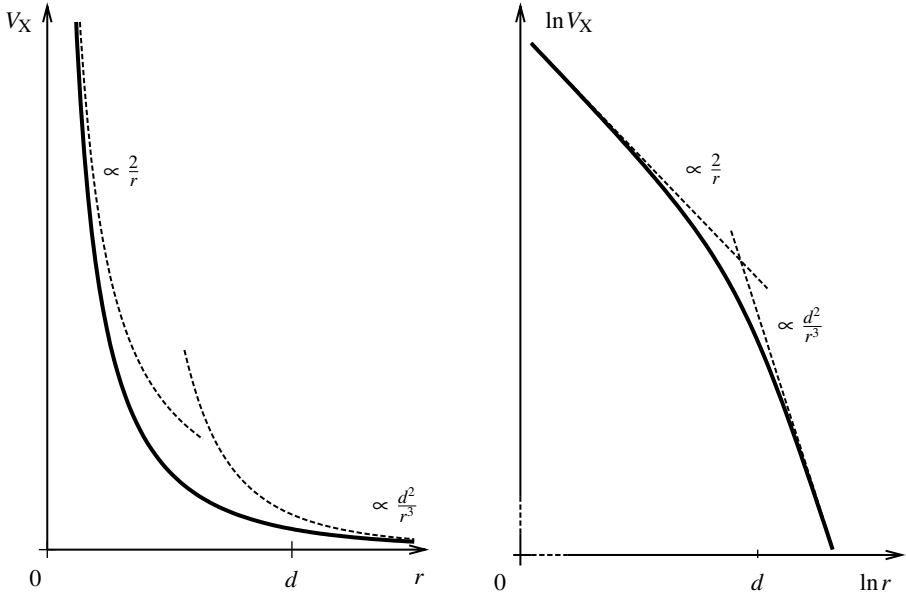


Figure 6.1 Classical approximation of the indirect exciton interaction V_{XX}^{cl} [Eq. (6.25)]. The dashed lines show the asymptotic behavior [Eq. (6.26)].

6.3 The Quantum Well Problem

The first step of the adiabatic approximation involves the solution of the single-particle out-of-plane problem. The Hamiltonian for a single electron (hole) in a quantum well with an electric field reads

$$\hat{H}_\alpha = -\frac{\hbar^2}{2m_\alpha} \frac{\partial^2}{\partial z^2} + V_\alpha \Theta\left(\left|z\right| - \frac{L}{2}\right) + \frac{q_\alpha}{\epsilon} E_z z, \quad \alpha = e, h, \quad (6.27)$$

where m_α is the (out-of-plane) mass and q_α the charge of the particle in question, V_α the depth and L the width of its confining quantum well centered at 0, and E_z the strength of the applied electric field in z -direction.

For numerical treatment, it is essential to reduce the problem to its actual free parameters. To this end, one introduces dimensionless units by the renormalization

$$E \rightarrow \frac{2\lambda_\alpha}{L^2} E', \quad z \rightarrow Lz', \quad (6.28)$$

where $\lambda_\alpha = \hbar^2/(2m_\alpha)$ is the quantumness of the particle species “ α ”. Applying (6.28) with an additional intermediate step $E \rightarrow 2\lambda_\alpha E''$ without length rescaling,

one obtains the effective Hamiltonian(s)

$$\hat{H}_\alpha'' = -\frac{1}{2}\partial_z^2 + V^{\text{eff}}\Theta\left(|z| - \frac{L}{2}\right) + E^{\text{eff}}z, \quad (6.29)$$

$$\hat{H}_\alpha' = -\frac{1}{2}\partial_{z'}^2 + L^2V^{\text{eff}}\Theta\left(|z'| - \frac{1}{2}\right) + L^3E^{\text{eff}}z', \quad (6.30)$$

where the shortcuts $V^{\text{eff}} = 2\lambda_\alpha V_\alpha$ and $E^{\text{eff}} = 2\lambda_\alpha E_z q_\alpha / \epsilon$ were introduced. The two-step approach was used to stress the problem's scaling with length, i.e. replacing the parameters as

$$(L, V^{\text{eff}}, E^{\text{eff}}) \rightarrow (1, L^2V^{\text{eff}}, L^3E^{\text{eff}}), \quad (6.31)$$

in the first Hamiltonian yields the second Hamiltonian describing exactly the same problem (on a renormalized energy scale). Thus, on a theoretical level, the quantum well plus electric field problem can be fully understood by considering it at a fixed width and changing only the potential depth and electric field strength. For an experimental realization in semiconductor heterostructures however, the potential depth is a material constant, but a large region of the parameter space is still accessible by tuning the well width. This will be explored at the end of this section, when discussing the application of the theoretical results to real materials.

6.3.1 Electron and Hole Density Distributions

Several methods are available for finding solutions to (6.30). In the present case, the focus lies on obtaining the thermal (canonical) density matrix $\rho(z; \beta)$. A straightforward path is the simulation of a single particle in the potential defined by (6.30) at given external parameters L^2V^{eff} , L^3E^{eff} and the (effective) temperature

$$\beta \equiv \frac{2\lambda_\alpha}{L^2} \frac{1}{k_B T}. \quad (6.32)$$

PIMC is a natural choice for the simulation method and has been done in previous studies [114, 115]. Tackling the problem with PIMC has the advantage that the method delivers more than just density profiles. Additionally, it is easy to extend the analysis to related multi-particle problems.

The disadvantages of computing $\rho(z; \beta)$ with PIMC are mainly numerical concerns (convergence, simulation time, stability, etc). The biggest problem arises due to the non-differentiability of the potential at the quantum well edges – in the simulation, inter-action derivatives are needed for an exact energy estimation. This can be circumvented if using a slightly modified, differentiable potential. A more tricky approach uses immobile virtual particles and mimics the wall potential with the interaction to these particles [115].

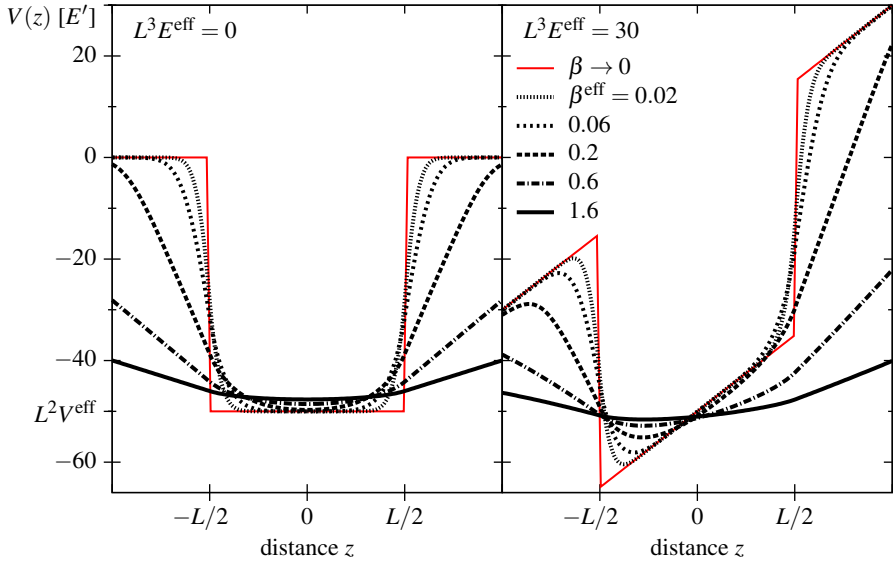


Figure 6.2 Temperature dependence of the effective trapping potential $V(z)$ of a particle in quantum well of width L and strength $L^2 V^{\text{eff}} = 50$ at two different electric field strengths $L^3 E^{\text{eff}}$. The red curve shows the classical quantum well potential valid in the high-temperature limit $\beta \rightarrow 0$. Each black curve displays the effective potential a classical particle feels due to quantum effects.

For this thesis, a completely different approach was chosen. Due to its single-particle 1D nature, the matrix squaring method qualifies as a direct way to compute $\rho(z; \beta)$. The differentiability of the potential is of no concern as the method bases solely on integration. It also very robust and very fast, especially in 1D where no partial wave expansion is needed.

Matrix squaring itself is explained in detail in chapter 4.2. In a nutshell, the same high-temperature representation of the density matrix as for PIMC is levered, but the path-integral is computed directly. This works reliably only if the integral's complexity is low, i.e. the penalty for writing a given density matrix as a product at twice the temperature leads only to a single additional integration. m iterations of convolution integrals of the density matrix with itself – starting at a given temperature β – then yields the desired density matrix at a 2^m -times lower temperature. The accuracy can readily be checked by starting at a higher temperature and doing more iterations (squarings).

The resulting density matrix can be interpreted as an effective potential $V(z)$ according to Eq. (5.16) in the following sense: A classical point-like particle moving in such an effective potential leads to thermal expectations identical to those obtained when solving the original quantum mechanical problem. All single-particle quantum effects are absorbed in shape of the potential. Figure 6.2 illustrates

the impact of these effects for the quantum well problem. Each black curve displays the potential at a different temperature starting from the classical potential shown with a red curve. The (effective) temperature range was adjusted to highlight the typical results when employing this method. At high temperatures $\beta \lesssim 0.1$ only minor alterations are observed – sharp edges are smoothed, but the original shape is clearly visible. Around $\beta \approx 0.1 \dots 1$, quantum effects start to dominate and smooth out most of the details found in original potential. In the shown $\beta = 1.6$ case, even the differences between different electric field strengths (cf. left and right panel of Fig. 6.2) seem to disappear. Below $\beta \approx 1$, the system settles into the ground state which then constitutes the sole remaining contribution to the density matrix (or the action, respectively). Due to Eq. (5.16), only the product $\beta V(z)$ converges, so the effective potential $V(z)$ still softens to counteract an increase of β . Indeed, the perceived difference of the $\beta = 0.6$ and $\beta = 1.6$ cases in Fig. 6.2 is a constant proportional to the temperature change.

The density distribution $\rho(z)$ can be computed from the diagonal elements of the density matrix $\rho(z, z'; \beta)$. As the matrix squaring method works with unnormalized $\rho(z, z'; \beta)$, $\rho(z)$ must be normalized by the partition function, i.e.

$$\rho(z) = \frac{1}{Z} \int dz' \rho(z, z'; \beta) \delta(z - z') = \frac{1}{Z} \rho(z, z; \beta), \quad Z = \int_{-a}^a dz \rho(z, z; \beta), \quad (6.33)$$

where $z, z' \in [-a; a]$ is the interval on which the density matrix is tabulated. If $\rho(z, z; \beta)$ does not fall off fast enough towards this artificial boundary, the interval must be extended to obtain an accurate normalization. Although the computational cost to do so is easily manageable, the Hamiltonian (6.30) in combination with matrix squaring does not improve the results in the way sought. Firstly, a constant homogeneous electric field extending infinitely is unphysical and would result in particles gaining ever more energy by running down the ramp. Secondly, the matrix squaring method as a statistical method is ignorant of the particle dynamics, i.e. there is no initial preparation of the particle in a particular state. If the outermost edge of the (spatially finite) electric field falls way below the bottom of the quantum well, the resulting density matrix will be more or less sharply peaked at this edge. In thermal equilibrium, this is the expected and correct result, regardless how long an initially trapped particle could sustain before it escapes by tunneling.

Fortunately, matrix squaring is quite stable with respect to edge conditions: Extending or shrinking the tabulated area does not affect the shape of the density very much, it only alters the normalization of the density distribution $\rho(z)$ as discussed above. Furthermore, the focus here lies on finding $\rho(z)$ for a particle which remains confined in the quantum well for long, but not necessarily infinite time. A good indicator for a low tunnel leakage rate is a high (well) peak to (wall) minimum ratio of $\rho(z)$ which is independent of the normalization. If this is the

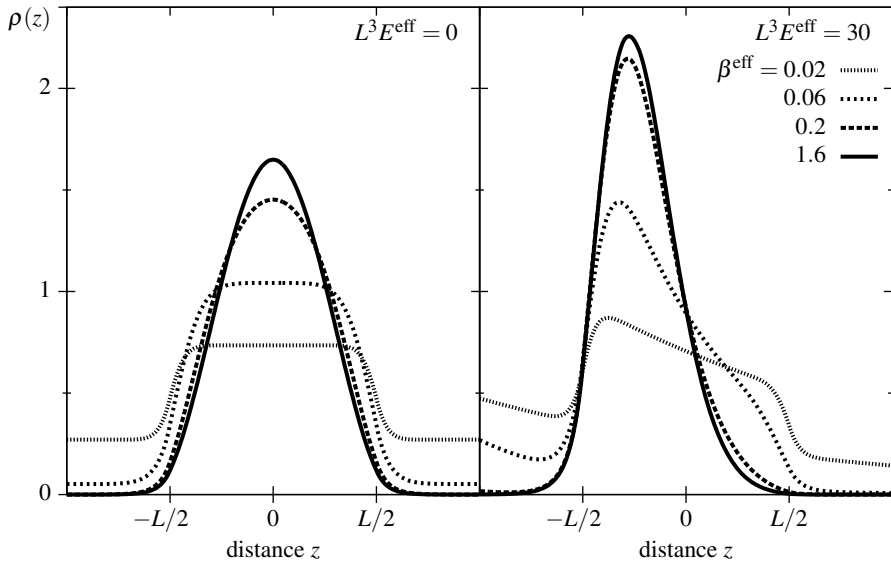


Figure 6.3 Temperature dependence of the density distribution $\rho(z)$ of a particle in quantum well of width L and strength $L^2V^{\text{eff}} = 50$ at two different electric field strengths L^3E^{eff} . Each $\rho(z)$ is normalized to 1 over the full computational range $[-L, L]$. Obviously, such a normalization is very sensitive on the computational range if the particle is not fully trapped as in the high-temperature scenarios $\beta \lesssim 0.1$.

case, the inevitable increase of $\rho(z)$ to the edge of the computational interval becomes irrelevant. One can then trim a so that any major out-of-well increase is absent and obtain a meaningful estimate for $\rho(z)$ by using (6.33).

Figure 6.3 displays the density distribution $\rho(z)$ for the same simulation parameters as in Fig. 6.2. The normalization according to (6.33) was carried out on the full computational range spanning $2L$. Apparently, this does not make the results look very normalized for higher temperatures $\beta \leq 0.06$. However, the problem is only partly related to the issues discussed above – for $\beta \lesssim 0.1$, there is a non-negligible contribution of continuum states to the thermal density matrix $\rho(z, z'; \beta)$.

On the other end of the temperature range, the only remaining contribution to $\rho(z, z'; \beta)$ originates from the ground state. This point is reached at $\beta \gtrsim 1$ where no further changes to $\rho(z)$ are observed at lower temperatures. For this reason, the data for $\beta = 0.6$ (cf. Fig. 6.2) is omitted from Fig. (6.3) as it practically coincides with the curve shown for $\beta = 1.6$. Due to its origin, $\rho(z)$ is sharply peaked at low temperatures. As expected, the position of the peak is shifted in presence of an electric field. The amount of this shift with respect to the external parameters is the central question of the following investigation.

The results shown Fig. 6.2 and 6.3 allow to draw a first conclusion regarding

the temperature necessary for an experimental realization of indirect excitons. For multiple reasons – stable confinement and strong localization among others – it is necessary to reach temperatures where the particle resides in the ground state which implies

$$\beta \gtrsim 1, \quad k_{\text{B}}T \lesssim \frac{2\lambda_{\alpha}}{L^2} \propto \frac{1}{m_{\alpha}L^2}, \quad (6.34)$$

where the latter expression follows immediately from the definition (6.32). In this context, the following computations are done at a single temperature, $\beta = 2$. This restriction comes with no loss of generality for the validity of $\rho(z)$ as long as (6.34) holds.

Figure 6.4 shows the results for the three different effective trapping potentials $L^2V^{\text{eff}} = 5$ (top), 50 (middle) and 500 (bottom). Each time, the effective electric field strength L^3E^{eff} is increased in evenly spaced steps until the quantum well fails to trap the particle within its walls. Curves shown in red indicate such failings.

When increasing L^2V^{eff} , the localization of $\rho(z)$ also increases greatly and L^3E^{eff} can be increased to much higher values before the particle leaks out of the trap. More interestingly, the maximum achievable shift of the peak position of $\rho(z)$ is greatly enhanced: At $L^2V^{\text{eff}} = 5$, $\rho(z)$ barely leaves its central position before leaking at $L^3E^{\text{eff}} \approx 3$. But at $L^2V^{\text{eff}} = 500$, $\rho(z)$ can be pinned against one potential wall. The opposite half of the potential is almost completely evacuated.

6.3.2 Estimating the Dipole Moment

The dipole moment of an electron-hole pair in the quantum well can be computed according to Eq. (6.9). For an accurate estimation, one needs to insert the electron and hole density distributions obtained from the two-body problem which includes the attraction of electron and hole. Unfortunately, Matrix Squaring is unable to cope with this problem, so one should resort to other methods like PIMC simulations. On the other hand, one may safely use the single body solutions from the previous section if the correlations are sufficiently weak. Previous studies [115] found that the correlations can be neglected for strong electric fields, or, more specifically, if the condition

$$\frac{e^2}{\epsilon d} \ll E_z d \quad (6.35)$$

is satisfied. Otherwise, using the single-particle solutions overestimates the dipole moment. In the following, it is assumed that this condition holds. In any case, the presented results set an upper bound for the dipole moment with the given parameters.

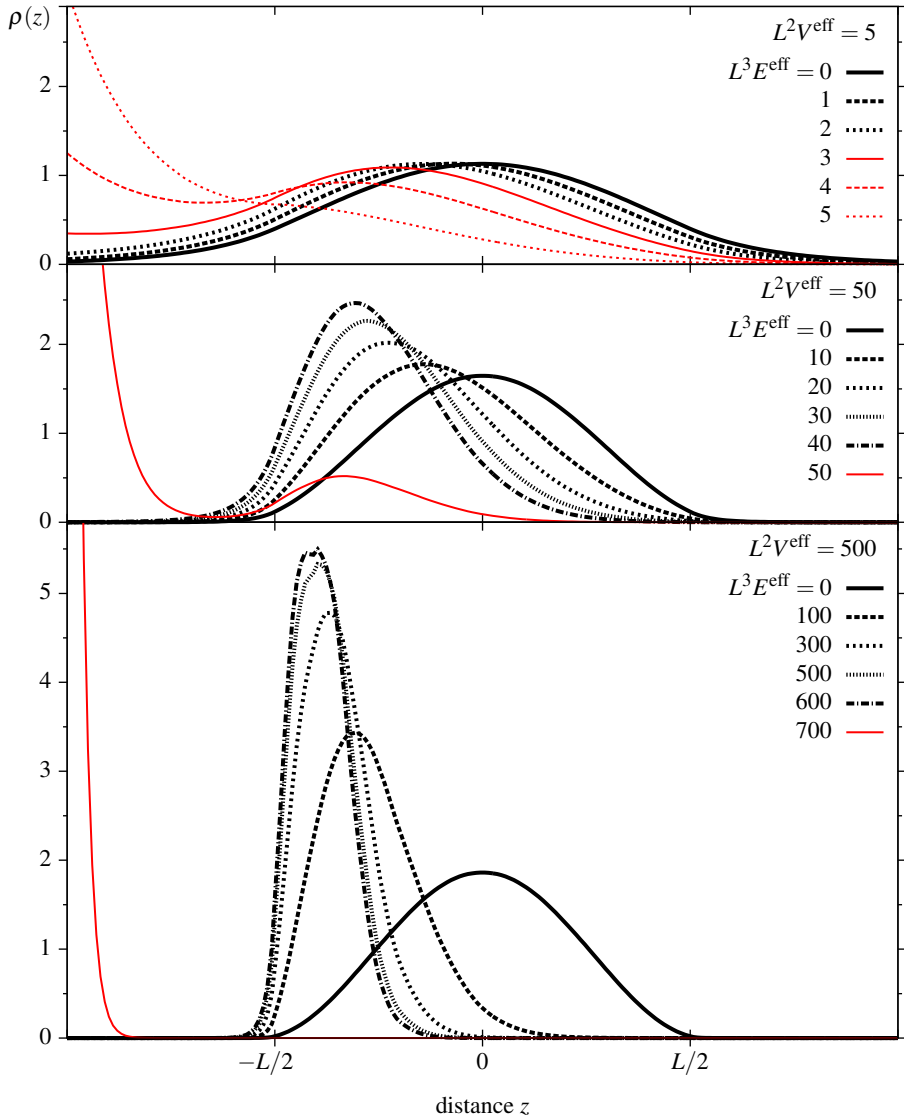


Figure 6.4 Density distribution $\rho(z)$ of a particle in quantum well of width L at three different trapping strengths L^2V^{eff} (fixed in each panel) and various electric field strengths L^3E^{eff} . The scaling of the ordinates is kept constant across all panels and each $\rho(z)$ is normalized to 1 over the full computational range $[-L, L]$ making the particle localizations visually comparable. Curves drawn in red mark parameter choices where the particle cannot be fully trapped in the quantum well. Note that this characterization is somewhat dependent on the computational range, see text for an explanation.

In the simplest, mass symmetric case, $\lambda_e = \lambda_h$, the dipole moment can be estimated directly from a single particle computation:

$$d^{\text{symm}} = L \int_{-a}^a dz z \rho(z), \quad (6.36)$$

where $[-a; a]$ is the tabulation interval. The reasoning for the choice of a finite a is the same as before (see discussion for Eq. (6.33)). Computing the dipole moment in this way is the most useful approach for quantifying the shift of the peak position of $\rho(z)$.

Obviously, the dipole moment d is always 0 in absence of an external electric field. The well width L sets the maximum theoretical value for d , but this value can only be achieved in the limit $V_0 \rightarrow \infty$. As seen in Fig. 6.4, the practical upper limit of d is dependent on the ability to trap the particle successfully. For weak dipole moments, any reasonable choice for the integration interval a yields accurate results for d [Eq. (6.36)]. Increasing the effective electric field strength $L^3 E^{\text{eff}}$ while keeping a constant results in a sudden jump of d at some point, especially for large trapping strengths $L^2 V^{\text{eff}}$ (cf. the difference between the red and black curves in Fig. 6.4). This point sets a lower bound for the estimate of the maximum dipole moment. This bound can be improved if a is trimmed down carefully; however, computations of d remain unreliable to certain degree in vicinity of its upper limit due to the restrictions on choosing a (see discussion for Eq. (6.33)).

If an exact estimate of the limiting value of d is not the primary concern, the choice of a is not so important. This is certainly the case here, as operating at the utmost edges is not required for an experimental realization of indirect excitons. To this end, a was set to L , i.e. computing the integral (6.36) over twice the quantum well width, $2L$. A large array of computations has been carried out at several potential strength $L^2 V^{\text{eff}} = 1 \dots 4000$ while also varying the electric field strength $L^3 E^{\text{eff}} = 1 \dots 1000$. The results for the dipole moment d are shown in Fig. 6.5. Red curves correspond to results where $L^2 V^{\text{eff}}$ is weak and stable trappings seems rather uncertain [cf. Fig. 6.4, upper panel]. However, the trend for weak $L^3 E^{\text{eff}}$ matches those shown for larger $L^2 V^{\text{eff}}$ (black curves). In this regime, the dipole moment d/L increases linear with $L^3 E^{\text{eff}}$. The response coefficient decreases with increasing $L^2 V^{\text{eff}}$, but seems to settle at a lower bound marked via a solid red line in Fig. 6.5, for $L^2 V^{\text{eff}} \gtrsim 1000$.

The estimate for the lower bound of the maximum d is marked by the dot-dashed red line in Fig. 6.5. The behavior of d in vicinity to this limit depends on $L^2 V^{\text{eff}}$. For large $L^2 V^{\text{eff}}$, d saturates and increases only slightly with further increase of $L^3 E^{\text{eff}}$ before reaching its maximum value. This plateau regime cannot be reached for $L^2 V^{\text{eff}} \lesssim 100$. Or equivalently, stable trapping must be possible for $L^3 E^{\text{eff}} \gtrsim 600$.

The universal behavior of d for $L^2 V^{\text{eff}} \gtrsim 1000$ extends to plateau regime – the only perceptible difference is the value of $L^3 E^{\text{eff}}$ at which trapping becomes

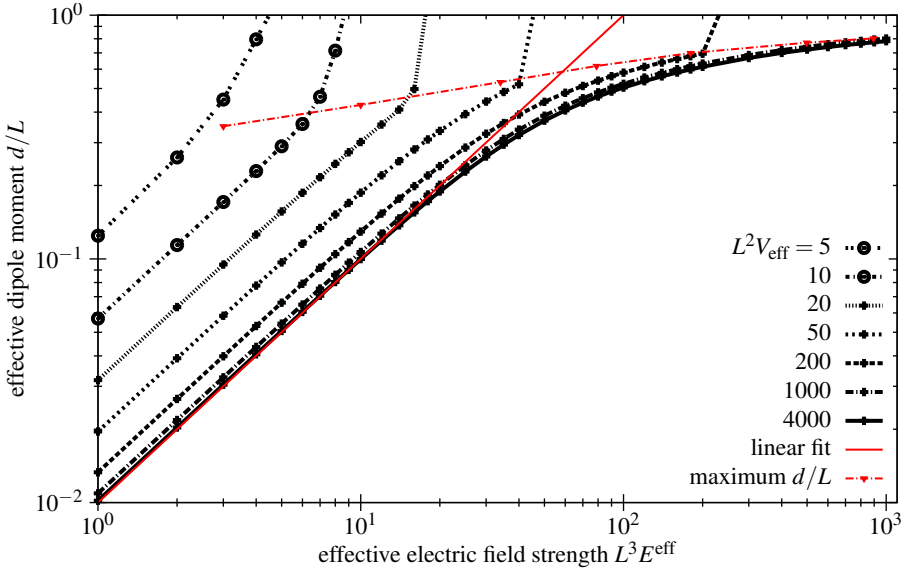


Figure 6.5 Dependence of the effective dipole moment d/L on the effective electric field strength $L^3 E^{\text{eff}}$ for a mass symmetric pair of particles with opposite charges confined in a quantum well of width L . Black lines connect matrix squaring results for the same effective potential depth $L^2 V^{\text{eff}}$. There is no clear distinction whether a particle resides within or without the trap in case of the two weakest trapping strengths (marked with open circles), especially near the maximum d/L line (dashed red) [cf. Fig. 6.4, upper panel]. The solid red line marks a linear fit approximating the d -dependence for weak field strengths E at high trapping strengths $L^2 V^{\text{eff}} \gtrsim 600$.

unstable. The overall dependence of d on $L^2 V^{\text{eff}}$ and $L^3 E^{\text{eff}}$ is neatly summarized in a contour plot (6.6), each curve connecting points of equal dipole moment d . The red line marks the maximum theoretical limit $d = L$ – parameter values which fall into the shaded area are not expected to yield stable results.

In realistic materials, one must take the usually asymmetric electron/hole masses into account. Considering the generic Hamiltonian (6.30), the differences between an electron and a hole enter by changes of the effective V^{eff} and E^{eff} . From their definition, one sees

$$\frac{V_h^{\text{eff}}}{V_e^{\text{eff}}} = \frac{m_h V_e}{m_e V_h} \approx \frac{m_h}{m_e}, \quad \frac{E_h^{\text{eff}}}{E_e^{\text{eff}}} = \frac{m_h}{m_e}, \quad (6.37)$$

with $V_e \approx V_h$ which holds for most materials. Thus, the results presented for the dipole moment d of symmetric particles can easily be adapted to the new situation provided that the temperature condition (6.34) is still met by the heavier particle (which is typically the hole). In this case, the dipole moment becomes

$$d^{\text{asymm}} = \frac{1}{2} d^{\text{symm}} \left(V_h^{\text{eff}}, E_h^{\text{eff}} \right) + \frac{1}{2} d^{\text{symm}} \left(\frac{m_h}{m_e} V_h^{\text{eff}}, \frac{m_h}{m_e} E_h^{\text{eff}} \right), \quad (6.38)$$

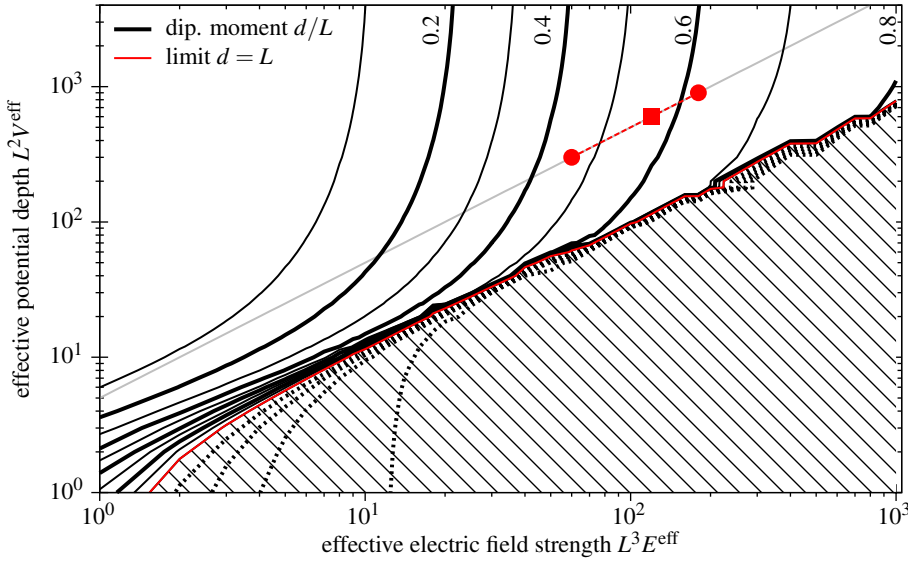


Figure 6.6 Effective dipole moment d/L depicted as contour plot. The axes span the parameter space of $L^3 E^{\text{eff}}$ and $L^2 V^{\text{eff}}$ on which d/L was computed with the matrix squaring method for a mass symmetric pair of particles with opposite charges confined in a quantum well of width L . Points with equal d/L are connected with black lines. The red line marks the theoretical upper limit of $d = L$. Parameter tuples which fall into the shaded area are unable to reliably trap particles within the quantum well.

when taking the hole as reference particle.

According to Eq. (6.37), pairs of parameter tuples always obey $V_e^{\text{eff}}/E_e^{\text{eff}} = V_h^{\text{eff}}/E_h^{\text{eff}}$. Thus, both tuples fall onto a line parallel to $L^2 V^{\text{eff}} = L^3 E^{\text{eff}}$. The mass ratio m_h/m_e determines the spacing between the electron tuple and hole tuple. When noting their values in Fig. 6.6, their arithmetic average corresponds parameter tuple determining the value of the dipole moment d . Obviously, this point falls onto the line connecting the electron tuple with the hole tuple.

An example for the graphical construction of the dipole moment d^{asymm} for $m_h/m_e = 3$ is marked in Fig. 6.6. The lower red dot corresponds to the electron's parameter tuple and the upper to the hole's. One of either can be freely chosen, the mass ratio unambiguously determines the other. The value of d^{asymm} can be read off at the position marked by the red square. Judging from this example, the mass ratio of a given material can have a significant influence on the dipole moment.

6.3.3 The Effective in-Plane Interactions

With the single electron/hole density distribution $\rho_e(z)$, the effective in-plane interaction can be computed according to Eq. (6.8). Introducing a relative variable

$t = z - z'$, this integral can be expressed as

$$V_{\alpha\beta}(r; \beta) = \frac{q_\alpha q_\beta}{\epsilon} \int dt \frac{h_{\alpha\beta}(t; \beta)}{\sqrt{r^2 + t^2}}, \quad (6.39)$$

where $h_{\alpha\beta}$ is defined as density-density correlation

$$h_{\alpha\beta}(t; \beta) \equiv \int dz \rho_\alpha(z; \beta) \rho_\beta(z + t; \beta) = (\rho_\alpha \star \rho_\beta)(t; \beta). \quad (6.40)$$

In the same species scenario, i.e. $\alpha = \beta$, Equation (6.40) yields the auto-correlation $h_{\alpha\alpha}(t; \beta)$ and $h_{\beta\beta}(t; \beta)$. The correlation integral can be solved directly, or by using the relation $(f \star g) = \mathcal{F}^{-1}[\mathcal{F}[f]^* \cdot \mathcal{F}[g]]$, where $\mathcal{F}[f]$ is the Fourier transform of f . The second, indirect method is much faster when taking advantage of Fast-Fourier-Transforms (FFT).

When using results from the previous section, the conversion from the effective out-of-plane units must be considered. For the density distribution this means

$$\rho_\alpha(z; \beta) = \frac{1}{L} \rho'_\alpha(z/L; \beta) = \frac{1}{L} \rho'_\alpha(z'; \beta), \quad (6.41)$$

where the prime indicates that the quantity is to be taken in effective units used in the previous subsection. With Eq. (6.40), one has $h_{\alpha\beta}(t; \beta) = h'_{\alpha\beta}(t/L; \beta)/L$, so Eq. (6.39) can be rewritten as

$$V_{\alpha\beta}(r; \beta) = \frac{e_\alpha e_\beta}{\epsilon L} V'_{\alpha\beta}(r/L; \beta), \quad V'_{\alpha\beta}(r'; \beta) = \int dt' \frac{h'_{\alpha\beta}(t'; \beta)}{\sqrt{r'^2 + t'^2}}. \quad (6.42)$$

It is instructive to take a look at the correlation function $h_{\alpha\beta}(t; \beta)$ separately, as it enters Eq. (6.39) like an effective density distribution. Figure 6.7 shows the results for a symmetric electron-hole pair. The chosen effective trapping strength of $L^2 V^{\text{eff}} = 500$ is sufficiently large to ensure strong particle localizations and make large electron-hole separations possible (cf. Fig. 6.6). Three different electric field strengths, $L^3 E^{\text{eff}} = 5$ (left panel), 50 (middle panel), and 500 (right panel) cover the full range from weak to strong e-h-separation. In each case, the input density distributions for the electron, $\rho_e(z)$, and for the hole, ρ_h are shown as red curves. A black solid line denotes the auto-correlation $h_{\alpha\alpha}(z)$ and a black dashed line denotes the cross-correlation $h_{\alpha\beta}(t)$. This covers all cases, as it is $h_{ee} = h_{hh}$ and $h_{eh} = h_{he}$ due to the mass symmetry.

Not surprisingly, the correlation functions are always smoother than their generating density distributions. The auto-correlation is also always symmetric with respect to $t = 0$. It is singly peaked at $t = 0$ whose height grows in unison with its contributing density distribution: The stronger ρ_α is localized, the higher $h_{\alpha\alpha}$ peaks.

The cross-correlation is also symmetric to $t = 0$ and for small dipole moments $d \ll L$, the cross-correlation is virtually identical to the auto-correlation

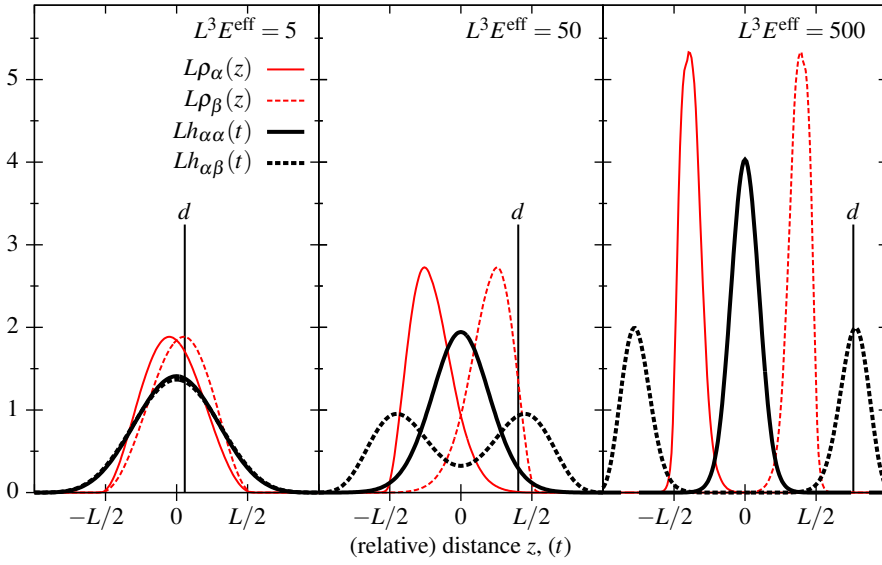


Figure 6.7 Density-density correlations $h_{\alpha\alpha}(t)$ (solid black), and $h_{\alpha\beta}(t)$ (dashed black) for a mass symmetric pair of particles with opposite charges confined in a quantum well of width L . The wall potential is sufficiently strong ($L^2 V^{\text{eff}} = 500$) to enable strong localization of the particle densities $\rho_{\alpha}(z)$ (solid red), $\rho_{\beta}(z)$ (dashed red). Displayed are three cases with increasing field strength $L^3 E^{\text{eff}} = 5, 50, 500$ from left to right.

with a single peak at $t = 0$. However, the peaks of $h_{\alpha\beta}$ are approximately centered at $|t| = d$ and, thus, $h_{\alpha\beta}$ develops its typical bimodal appearance for larger d .

Because the correlation functions retain the normalization to unity, the each peak of the cross-correlation has (approximately) half the weight of the single auto-correlation. Taking into account the form of the integrand in Eq. (6.39), one has $|V_{\alpha\beta}| \leq V_{\alpha\alpha}$ and $|V_{\alpha\beta}| \leq V_{\beta\beta}$ for all in-plane distances r . Hence, the effective in-plane potential is purely repulsive.

Figure 6.8 displays the effective in-plane potential and its contributions for the same parameters as in Fig. 6.7. Because auto-correlation and cross-correlation are virtually identical for small $d \ll L$ (left panel), their contributions to the in-plane potential $V_{\alpha\alpha} + V_{\alpha\beta}$ (black dashed line) cancel each other to a large degree. This leads to a deviation of several orders of magnitude from the classical exciton-exciton interaction $V_{\text{XX}}^{\text{cl}}$ (red dashed line) at small in-plane distances $r \lesssim d$. The quality of $V_{\text{XX}}^{\text{cl}}$ improves for larger d . In all cases however, both classical and effective in-plane potential coincide in their long-range asymptotes $r \rightarrow \infty$ matching the standard dipole potential $V \sim d^2/r^3$.

A striking feature of the computed same-species potentials $V_{\alpha\alpha}(r)$ is their logarithmic divergence in the limit $r \rightarrow 0$, in contrast to the usual $1/r$ divergence of

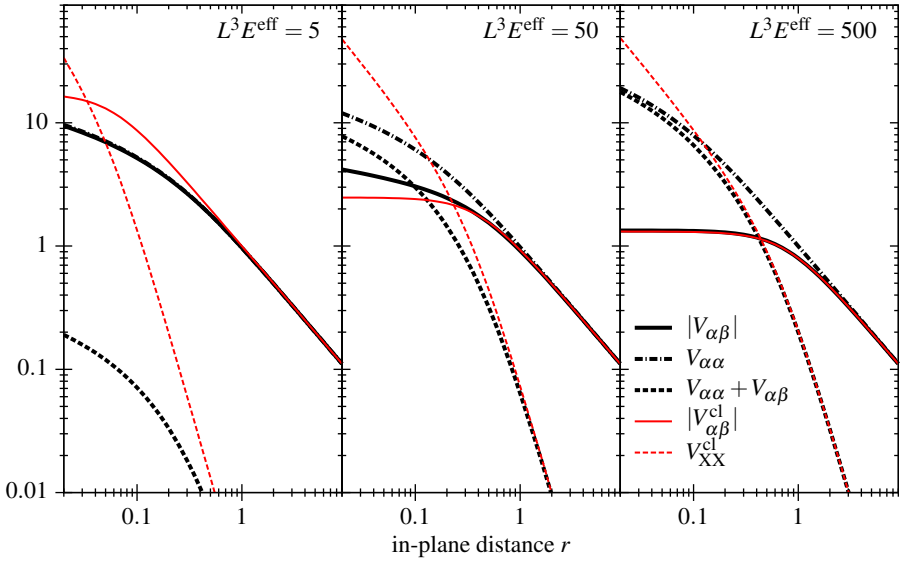


Figure 6.8 Several effective in-plane interactions for a mass symmetric pair of particles with opposite charges confined in a quantum well of width L . The conditions are identical those of Fig. 6.7 with a wall potential of $L^2 V^{\text{eff}} = 500$ and the three cases of increasing field strength $L^3 E^{\text{eff}} = 5, 50, 500$ from left to right. Each panel displays the same-species in-plane interaction $V'_{\alpha\alpha}(r')$ (dot-dashed black), the inter-species interaction $V'_{\alpha\beta}(r')$ (solid black) and their sum (dashed black) in comparison to the classical e-h interaction $V'_{\alpha\beta}{}^{\text{cl}}(r')$ (solid red) and the classical exciton interaction $V'_{\text{XX}}{}^{\text{cl}}(r')$ (dashed red). Primed quantities refer to the definition (6.42).

point-like charges. Due to the aforementioned similarity, the inter-species potential $V_{\alpha\alpha}(r)$ shares this behavior for small $d \ll L$. The asymptotic can be derived from Eq. (6.42) when assuming $h_{\alpha\beta}(t) = h_{\alpha\beta}(0) + \mathcal{O}(t^2)$, i.e.

$$V'_{\alpha\beta}(r') = \int dt' \frac{h_{\alpha\beta}(0)}{\sqrt{r'^2 + t'^2}} + \mathcal{O}(t') \xrightarrow{r' \rightarrow 0} -h_{\alpha\beta}(0) \ln r'. \quad (6.43)$$

This limit holds as long as $h_{\alpha\beta}(t)$ vanishes exponentially for $t \rightarrow \infty$ and one has $h_{\alpha\beta}(0) > 0$. Interestingly, the latter condition is not met for $h_{\text{eh}}(t)$ at large e-h separations [cf. Fig. 6.7, right panel]. In this case, $V'_{\text{eh}}(r')$ does not diverge and can be accurately approximated by $V_{\text{eh}}^{\text{cl}}(r) = 1/\sqrt{r^2 + d^2}$ (solid red line in Fig. 6.8).

6.3.4 Application

The theoretical investigation of the quantum well problem identifies two independently tunable parameters: The effective potential depth $L^2 V^{\text{eff}}$ and the effective electric field strength $L^3 E^{\text{eff}}$. Both parameters depend on the width L of quantum well which can be controlled by varying the thickness of the intermediate layer

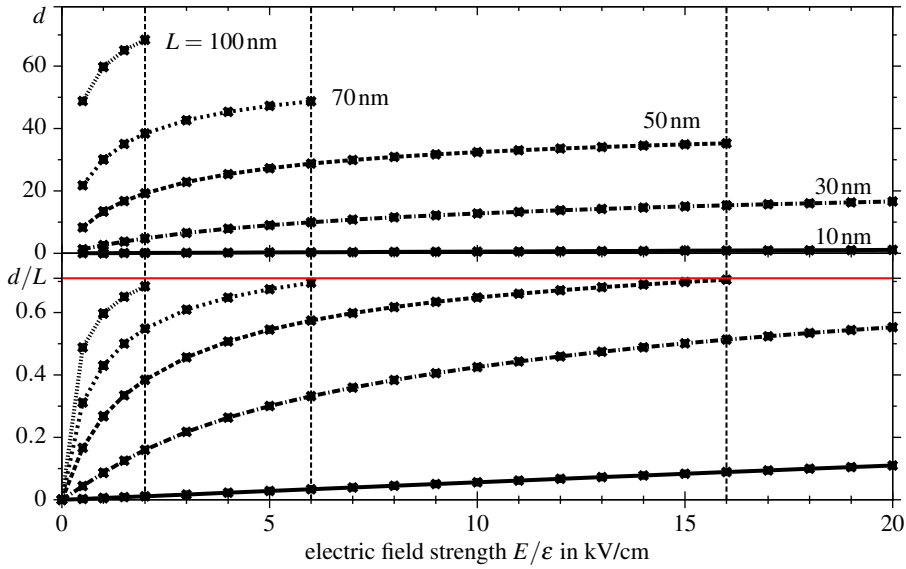


Figure 6.9 Dependence of the dipole moment d on the electric field strength E in a AlGaAs/GaAs quantum well of different widths L . Both panels depict the same data obtained via matrix squaring at temperatures satisfying condition (6.34). The upper panel shows d in nm. In the lower panel, the ordinate is rescaled according to d/L for each curve. The red lines marks the limiting d – and vertical black lines the corresponding limiting E – up to which stable solutions were found.

in an experimental realization with semiconductor heterostructures. Thus, very strong effective potential depths can be achieved, although V^{eff} is given only by material constants.

Of central importance is the dipole moment d of an electron-hole pair. Obviously, the chosen well width L limits the achievable dipole moment, i.e. $d < L$. Figure 6.9 displays the dependence of d in a AlGaAs/GaAs quantum well on the electric field strength E where each line corresponds to different widths L . Each curve shows a similar behavior: d increases linearly with E for weak electric field strengths and saturates before reaching its maximum value. Due to the scaling law $L^3 E^{\text{eff}}$, one needs much smaller values of E to achieve the same d in broader quantum wells. The limiting value is also reached at much smaller field strengths E .

The lower panel suggests that the upper limit for d is given by $d/L \approx 0.7$, e.g. one needs at least a well width of $L \gtrsim 50$ nm to achieve a dipole moment of $d = 35$ nm. However, the maximum upper limit is usually underestimated as calculations near this boundary depend heavily on the size of the integration grid (see explanation of Eq. (6.33)). Thus, it is likely that even larger d/L -ratios are possible.

From the findings above, one may conclude that a broader quantum well offers only advantages. It certainly allows for larger dipole moments d at smaller field strengths E and improves the electron-hole separation due to higher an effective potential depth $L^2 V^{\text{eff}}$. However, there is one serious drawback. All these results are valid if and only if the temperature condition (6.34) is met. If the temperature is too high, neither trapping nor a strong particle localization and, hence, dipole moment can be expected [cf. Fig. 6.3]. Unfortunately, the limiting temperature scales as $\propto L^{-2}$ according to (6.34) which runs contrary to the aforementioned advantages. As a result, the optimal experimental setup operates in the saturated regime close to the limiting d/L ratio for any desired dipole moment d .

Note that condition (6.34) must be satisfied for each particle species at the same time. Due to the scaling $T \propto m_\alpha^{-1}$, the limiting temperature is determined by the heavier particle which is the hole in most cases. For example, one has $T \lesssim 2.61$ K for a 30 nm wide AlGaAs/GaAs quantum well for which Figure 6.10 displays the density profiles $\rho_h(z)$, $\rho_e(z)$ and effective in-plane potentials $V_{hh}(r)$, $V_{ee}(r)$, $V_{eh}(r)$. The valence/conduction band offsets in an AlGaAs/GaAs heterostructure are quite similar, but GaAs features an out-of-plane mass ratio of $m_h^\perp/m_e = 5.65$ causing a much stronger effective trapping potential of $L^2 V_h^{\text{eff}} = 725.4$ for the hole in contrast to the electronic $L^2 V_e^{\text{eff}} = 170.1$. Hence, the hole is more localized even in absence of an external electric field [cf. the weak E case in Fig. 6.10, upper left panel], but the difference is quite small.

The particle's mass also affects its response to the electric field E as it enters into the effective field strength $L^3 E^{\text{eff}}$. The ratio $E_h^{\text{eff}}/E_e^{\text{eff}}$ always equals the mass ratio (see Eq. (6.37)). Hence, the hole reacts 5.65-times stronger to an electric field E resulting in larger shift and stronger edge localization. This behavior can be seen in the upper middle and rightmost panel of Fig. 6.10. The strength of the density localization is directly proportional to the height of the corresponding density auto-correlation. It comes at no surprise that $h_{hh}(t)$ (upper panel, solid black lines) has a more pronounced peak than $h_{ee}(t)$ (dashed black lines). While both peak heights increase with growing E , the hole-density auto-correlation is much more strongly affected and, thus, the peak-difference to $h_{ee}(t)$ also increases.

The effective same-species in-plane interactions $V_{\alpha\alpha}(r)$ [Eq. (6.39)] features a logarithmic divergence for $r \rightarrow 0$ proportional to $h_{\alpha\alpha}(0)$ [Eq. (6.43)]. $h_{\alpha\alpha}(0)$ increases with E and so does the corresponding $V_{\alpha\alpha}(r)$ for small r – and $V_{hh}(r)$ more so than $V_{ee}(r)$ (Fig. 6.10, lower panels, solid and dashed black lines, respectively).

Of course, the shape of the electron-hole cross-correlation $h_{eh}(t)$ is also affected by the mass ratio. But as in the equal mass case, $h_{eh}(t)$ always remains symmetric with respect to $t = 0$ and its peaks are close to $t = \pm d$ for large dipole moments. For sufficiently strong d , the corresponding effective e-h in-plane interaction $V_{eh}(r)$ approaches the $\propto -1/\sqrt{r^2 + d^2}$ -limit. The quality of this approximation depends on $h_{eh}(0)$ with a perfect alignment for a vanishing value.

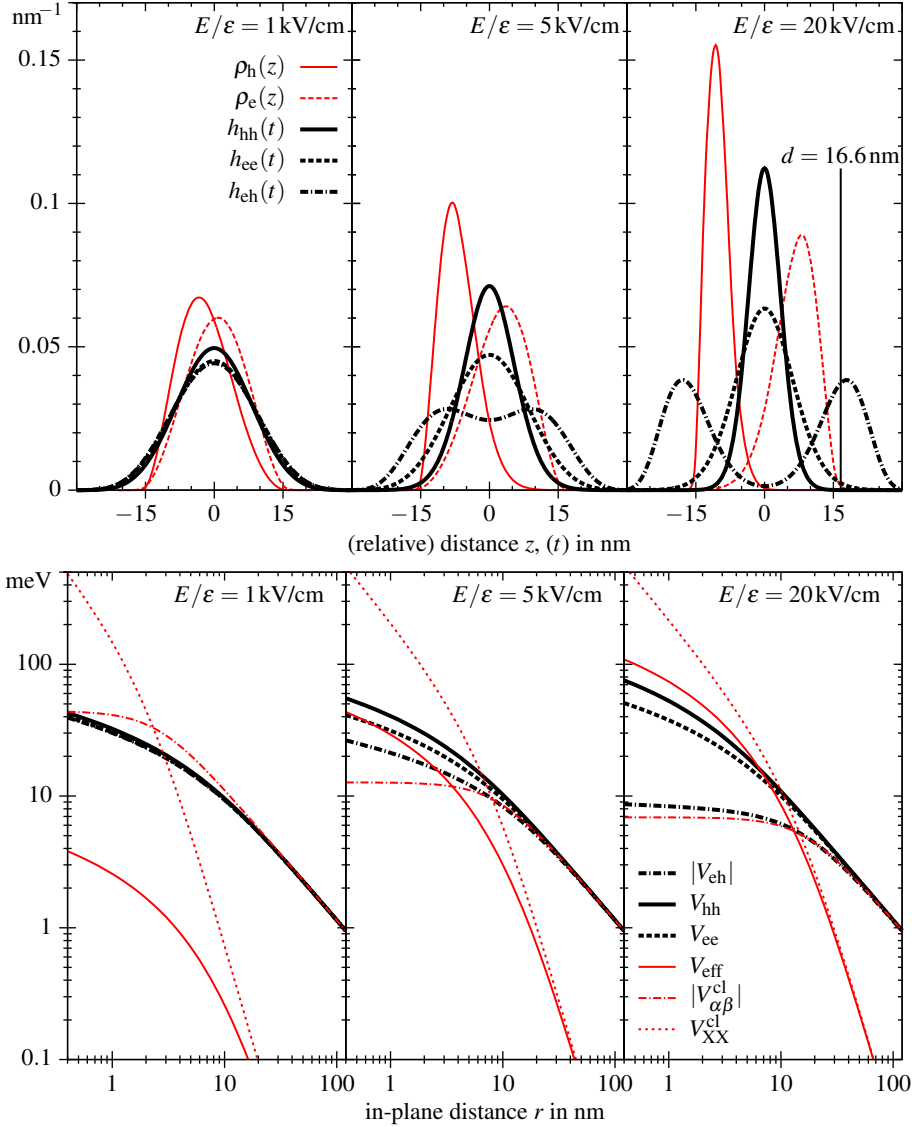


Figure 6.10 Results for a 30 nm wide AlGaAs/GaAs quantum well at three different electric field strengths. The densities were computed with the matrix squaring method at an effective $\beta = 2$ for each particle species. The results are valid for any temperature $T \lesssim 2.61$ K which satisfies Eq. (6.34) for both species at the same time. Upper panel: Electron density $\rho_e(z)$ and hole density $\rho_h(z)$ (red curves) as well as their correlation functions $h_{hh}(t)$, $h_{ee}(t)$ and $h_{eh}(t)$ (black curves). Lower panel: Effective in-plane interactions $V_{hh}(r)$, $V_{ee}(r)$, and $V_{eh}(r)$, the latter shown in comparison with the classical approximation $V_{\alpha\beta}^{cl}(z)$ (Eq. (6.23)). For reference, the sum $V_{eff}^cl(r) = V_{hh}(r) + V_{ee}(r) + 2V_{eh}(r)$ and the classical exciton interaction V_{XX}^{cl} are also shown.

Otherwise, $V_{\text{eh}}(r)$ still diverges logarithmically for $r \rightarrow 0$.

In summary, the mass ratio plays an important role in the small r behavior of same-species interactions, but is mostly irrelevant for the electron-hole potential in a scenario with a strong e-h separation and, hence, $h_{\text{eh}}(0) \rightarrow 0$. While the localization depends on the particle mass (see above), a sufficiently strong electric field in a sufficiently deep potential well can always enforce a good separation. The displayed $E/\epsilon = 20$ kV/cm results in Fig. 6.10 serve as an example.

6.4 The in-Plane Problem

The in-plane system describing electrons and holes as individual particles can be mapped to a system of excitons Eq. (6.11). The second adiabatic approximation requires a solution of the single exciton problem [cf. Eq. (6.13)], i.e.

$$\hat{H}_{\text{X}} = -\frac{\hbar^2}{2\mu} \nabla_r^2 + V_{\text{eh}}(r), \quad (6.44)$$

where the effective in-plane $V_{\text{eh}}(\mathbf{r})$ is given by Eq. (6.42). The previous investigation have shown that the classical approximation of the interaction potential (Eq. (6.8)), i.e.

$$V_{\text{eh}}^{\text{cl}}(r) = -\frac{q^2}{\epsilon} \frac{1}{\sqrt{r^2 + d^2}}, \quad (6.45)$$

describes the system quite accurately for situations where the electron-hole separation is sufficiently pronounced. Therefore, the problem is considered within this approximation as it simplifies the application of the matrix squaring method.

As with the quantum well problem, the Hamiltonian can be brought to a dimensionless form with the renormalization

$$E \rightarrow \frac{2\lambda_\mu}{\tilde{a}_{\text{B}}^2} \tilde{E} \equiv \tilde{\text{H}}\tilde{\text{a}} \tilde{E}, \quad r \rightarrow \tilde{a}_{\text{B}} \tilde{r} \equiv \frac{\epsilon\hbar^2}{q^2\mu} \tilde{r}, \quad (6.46)$$

where \tilde{a}_{B} and $\tilde{\text{H}}\tilde{\text{a}}$ are the effective atomic units of length and energy, respectively. Together with the classical approximation of $V_{\text{eh}}(r)$, the dimensionless Hamiltonian reads

$$\tilde{\hat{H}}_{\text{X}} = -\frac{1}{2} \nabla_{\tilde{r}}^2 - \frac{1}{\sqrt{\tilde{r}^2 + \tilde{d}^2}}, \quad (6.47)$$

where $\tilde{d} \equiv d/\tilde{a}_{\text{B}}$ denotes the dipole moment in units of the effective Bohr radius. \tilde{d} is the only remaining degree of freedom which greatly simplifies the investigation of the problem.

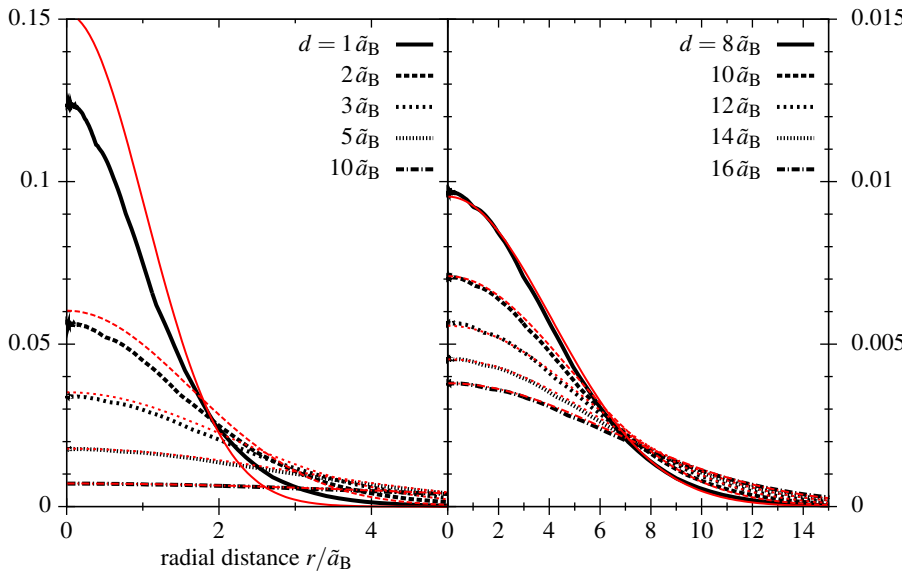


Figure 6.11 Radial density distributions $\rho_X(r)$ of the single-exciton problem (6.47) for different values of the dipole moment d . Black curves denote results from the matrix squaring method at temperatures satisfying the condition (6.48). Gaussian fits to the density profiles are shown as red curves. The right-hand panel is magnified by a factor of ten compared to the left; the curves for $d = 10 \tilde{a}_B$ are repeated to illustrate the scaling.

6.4.1 The Exciton Density Distribution

As before, matrix squaring can be used to solve the Bloch equation of the Hamiltonian 6.47 by computing the density matrix $\rho^X(\tilde{\mathbf{r}}, \tilde{\mathbf{r}}'; \beta)$ directly. The procedure is more involved as one has to deal with a two dimensional problem. For isotropic potentials, $\rho^X(\tilde{\mathbf{r}}, \tilde{\mathbf{r}}'; \beta)$ can be expanded in partial waves. One then applies matrix squaring to each of the l radial density matrix coefficients $\rho_l^X(\tilde{r}, \tilde{r}'; \beta)$ where l is the order of the expansion.

In the limit $d \rightarrow 0$, equation (6.47) converges to the standard 2D-Coulomb Hamiltonian. It is expected that the density distribution $\rho_X(\tilde{\mathbf{r}}; \beta)$ is dominated by ground state contributions at roughly $k_B T \lesssim 0.1 \tilde{\text{H}}\text{a}$ in this case. This condition is not valid for larger dipole moments $\tilde{d} > 1$, where the potential becomes more shallow and lower temperatures are needed. Tests with different values of \tilde{d} show that the temperature necessary to observe convergence of $\rho_X(\tilde{\mathbf{r}}; \beta)$ can be estimated with

$$\beta \gtrsim 10 \tilde{d}^{3/2}, \quad k_B T \lesssim \frac{\lambda_\alpha}{5 \tilde{a}_B^2 \tilde{d}^{3/2}} \propto \frac{1}{m_\alpha \tilde{d}^{3/2}}. \quad (6.48)$$

Furthermore, the increasingly shallow potential with increasing dipole moment \tilde{d} implies that the resulting radial density distribution $\rho_X(r)$ should also

broaden. Indeed, the results presented in Fig. 6.11 support this trend. One also notes that the density profile has a distinctive Gaussian shape as indicated by the fitting curves shown in red. Gaussian densities are characteristic for harmonic potentials. The connection is obvious when considering the series expansion of the potential:

$$\frac{1}{\sqrt{r^2 + d^2}} = \frac{1}{|d|} \left[1 - \frac{1}{2} \frac{r^2}{d^2} + \mathcal{O}\left(\frac{r^4}{d^4}\right) \right]. \quad (6.49)$$

The constant $1/|d|$ is simply an energy shift which does not influence the shape of the density. The second term can be identified as an effective harmonic potential with $\omega = |d|^{-3/2}$. The density matrix for the harmonic potential can be computed analytically, the exact expression is given in Ch. 2.3.2. Adapted to effective atomic units, one obtains

$$\rho_X(\tilde{r}; \tilde{\beta}) = \mathcal{G}_2(\tilde{r}; \sigma(\tilde{d}; \tilde{\beta})) , \quad \sigma^2(d; \beta) = \frac{1}{2} d^{3/2} \coth\left(\frac{1}{2} d^{-3/2} \beta\right) . \quad (6.50)$$

Note that $\coth(x > 2) \approx 1$ which supports the empirically found scaling of $\beta \propto d^{3/2}$ in the ground state condition (6.48). The computed densities have been compared to Eq. (6.50). However, a Gaussian fit shows much better agreement for

$$\sigma^2(d) = 1.05 d^{4/3} , \quad (6.51)$$

which is used in Fig. 6.11 for the red curves. This deviation may be due to neglected higher order terms in Eq. (6.49).

6.4.2 The Effective Exciton Interaction

Deriving the effective interaction $V_{XX}(R; \beta)$ is rather involved in the present case, as it requires a solution of the four dimension integral Eq. (6.17). As both, density matrices and the interaction potentials, are sharply peaked, a straightforward computation is additionally quite error prone.

Fortunately, Eq. (6.17) can be brought into a form similar to Eq. (6.42). To simplify the derivation, a compact notation for Eq. (6.17) is used, i.e.

$$V_{XX}(R_{ij}) = \sum_{\alpha, \beta=e,h} \tilde{V}_{\alpha\beta}(R_{ij}) , \quad (6.52)$$

$$\tilde{V}_{\alpha\beta}(R_{ij}) \equiv \int d^2 \mathbf{r}_i^{\text{eh}} d^2 \mathbf{r}_j^{\text{eh}} V_{\alpha\beta}(r_{ij}^{\alpha\beta}; \beta) \rho_X(r_i^{\text{eh}}; \beta) \rho_X(r_j^{\text{eh}}; \beta) . \quad (6.53)$$

where the original expressions Eqs. (6.18)–(6.20) are condensed to

$$\mathbf{r}_{ij}^{\alpha\beta} = \mathbf{R}_{ij} + \mu_\beta \mathbf{r}_i^{\text{eh}} - \mu_\alpha \mathbf{r}_j^{\text{eh}} , \quad (6.54)$$

with the shortcuts $\mathbf{r}_{ij}^{\alpha\beta} \equiv \mathbf{r}_i^\alpha - \mathbf{r}_j^\beta$, $\mathbf{R}_{ij} \equiv \mathbf{R}_i - \mathbf{R}_j$, and the definitions $\mu_h \equiv m_e''/M_X$ and $\mu_e \equiv -m_h''/M_X$.

Switching to a new set of integration variables

$$\mathbf{t}^{\alpha\beta} = \mu_\alpha \mathbf{r}_j^{\text{eh}} - \mu_\beta \mathbf{r}_i^{\text{eh}} = \mathbf{R}_{ij} - \mathbf{r}_{ij}^{\alpha\beta}, \quad \mathbf{x} = \mu_\alpha \mathbf{r}_j^{\text{eh}}, \quad (6.55)$$

transforms the integral $\tilde{V}_{\alpha\beta}(R_{ij})$ to

$$\tilde{V}_{\alpha\beta}(R_{ij}) = \int d^2\mathbf{t}^{\alpha\beta} V_{\alpha\beta}(|\mathbf{R}_{ij} - \mathbf{t}^{\alpha\beta}|; \beta) h_{\alpha\beta}(\mathbf{t}^{\alpha\beta}), \quad (6.56)$$

where $h_{\alpha\beta}(\mathbf{t})$ is defined as density-density cross-correlation

$$h_{\alpha\beta}(\mathbf{t}) = \frac{1}{\mu_\alpha^2 \mu_\beta^2} \int d^2\mathbf{x} \rho_\alpha(\mathbf{x}; \beta) \rho_\beta(\mathbf{x} + \mathbf{t}; \beta) = (\rho_\alpha \star \rho_\beta)(\mathbf{t}), \quad (6.57)$$

of the rescaled exciton densities $\rho_\alpha(\mathbf{x}) \equiv \rho_X(|\mathbf{x}|/|\mu_\alpha|; \beta)$. The integration (6.56) also has the form of a convolution unlike its cousin Eq. (6.42) for the quantum well case. This stresses the effect of the integration as a smoothing operation of the input potential $V_{\alpha\beta}$. Due to the Coulomb-like form of the input however, an evaluation of (6.56) using FFTs seems unfeasible.

The previous chapter shows that the exciton density matrix ρ_X quite accurately resembles a Gaussian of width σ , especially in the limit of strong dipole moments $\tilde{d} > 1$ [cf. Fig. 6.11]. With

$$\rho_\alpha(\mathbf{x}) = \mathcal{G}_2(\mathbf{x}/|\mu_\alpha|; \sigma) = \mu_\alpha^2 \mathcal{G}_2(\mathbf{x}; |\mu_\alpha|\sigma), \quad (6.58)$$

the correlation integral (6.57) can be computed analytically which gives

$$h_{\alpha\beta}(\mathbf{t}) = \mathcal{G}_2(\mathbf{t}; \sigma_{\alpha\beta}), \quad \sigma_{\alpha\beta} = \sigma \sqrt{\mu_\alpha^2 + \mu_\beta^2}. \quad (6.59)$$

Equation (6.42) can also be simplified with this result: Switching to polar coordinates and carrying out the angle integration yields

$$\tilde{V}_{\alpha\beta}(R_{ij}) = \int dt \sqrt{\frac{t}{R}} V_{\alpha\beta}(t; \beta) \mathcal{G}_1(t - R_{ij}; \sigma_{\alpha\beta}) \mathcal{I}_0\left(\frac{tR_{ij}}{\sigma_{\alpha\beta}^2}\right), \quad (6.60)$$

where $\mathcal{I}_n(x)$ is the scaled modified Bessel function [Eq. (4.21)].

The strength of the smoothing solely depends on the width $\sigma_{\alpha\beta}$ of the Gaussian kernel. $\sigma_{\alpha\beta}$ in turn depends parametrically on the dipole moment and the effective in-plane masses. With the results from the previous chapter, $\sigma_{\alpha\beta}$ evaluates to

$$\sigma_{ee} = \sqrt{2} \tilde{d}^{2/3} \frac{m_e}{M_X}, \quad \sigma_{hh} = \sqrt{2} \tilde{d}^{2/3} \frac{m_h}{M_X}, \quad \sigma_{eh} = \tilde{d}^{2/3} \sqrt{1 - 2 \frac{\mu_X}{M_X}}, \quad (6.61)$$

where μ_X denotes the reduced mass of the exciton. The ratio μ_X/M_X never exceeds $1/4$ – this value is reached for equal masses of electrons and holes. The specific expressions presented above were chosen due to stylistic reasons – one can rewrite each $\sigma_{\alpha\beta}$ in terms of only two parameters, the dipole moment d and the in-plane mass ratio m_h^i/m_e .

The integral (6.60) has an analytical solution for the Coulomb potential, i.e. $V_{\alpha\alpha}(r) = 1/r$, which reads

$$\tilde{V}_{\alpha\alpha}^C(R) = \frac{1}{R} \mathcal{I}_0 \left(\frac{R^2}{4\sigma_{\alpha\alpha}^2} \right), \quad (6.62)$$

with the asymptotes

$$\tilde{V}_{\alpha\alpha}^C(R) \xrightarrow{R \rightarrow 0} \sqrt{\frac{\pi}{2\sigma_{\alpha\alpha}^2}}, \quad \tilde{V}_{\alpha\alpha}^C(R) \xrightarrow{R \rightarrow \infty} \frac{1}{R}. \quad (6.63)$$

Equation (6.60) must be evaluated numerically for $V_{\alpha\beta}^{\text{cl}}(r) = 1/\sqrt{r^2 + d^2}$. However, the asymptotic solutions are given by

$$\tilde{V}_{\alpha\beta}^C(R) \xrightarrow{R \rightarrow 0} \sqrt{\frac{\pi}{2\sigma_{\alpha\beta}^2}} \exp\left(\frac{d^2}{2\sigma_{\alpha\beta}^2}\right) \left[1 - \operatorname{erf}\left(\frac{d}{\sqrt{2}\sigma_{\alpha\beta}}\right) \right], \quad (6.64)$$

$$\tilde{V}_{\alpha\beta}^C(R) \xrightarrow{R \rightarrow \infty} \frac{1}{R}. \quad (6.65)$$

As shown in Sec. 6.3.3, the classical electron-hole interaction $V_{\alpha\beta}^{\text{cl}}(r)$ is an accurate approximation of the exact $V_{\alpha\beta}(r)$ for strong e-h separations. One can expect a similar accuracy of $\tilde{V}_{\alpha\beta}^C(R)$ in this case. Contrastingly, differences between $V_{\alpha\alpha}(R)$ and $\tilde{V}_{\alpha\alpha}^C(R)$ may appear because the exact $V_{\alpha\alpha}(r)$ has a logarithmic divergence for $r \rightarrow 0$. As even the stronger $1/r$ divergence is completely smoothed out however, differences should be restricted to a minor shift of the $R \rightarrow 0$ asymptotic (6.63).

In summary, a direct evaluation of Eq. (6.60) using the classical potentials likely yields a very good approximation of the exact effective exciton interaction $V_{XX}(R)$ [Eq. (6.52)]. The approximation only depends on the dipole moment d and the (in-plane) mass ratio m_h/m_e via Eq. (6.61). The latter are material constants and the first is determined by the out-of-plane problem. Note that it is not important how exactly a specific value of d is realized.

Figure 6.12 shows the dependence of the effective exciton interaction $V_{XX}(R)$ [Eq. (6.52)] on the dipole moment d and the mass ratio m_h/m_e . The curves were computed using Eq. (6.60) with the classical approximations for the particle interactions. The findings show two general trends: First, increasing the dipole moment d strengthens the repulsion at large distances $R \gtrsim d$, but weakens the interaction otherwise. Second, a higher mass ratio leads to stronger repulsion at small distances $R \lesssim d$, but causes no changes on long ranges.

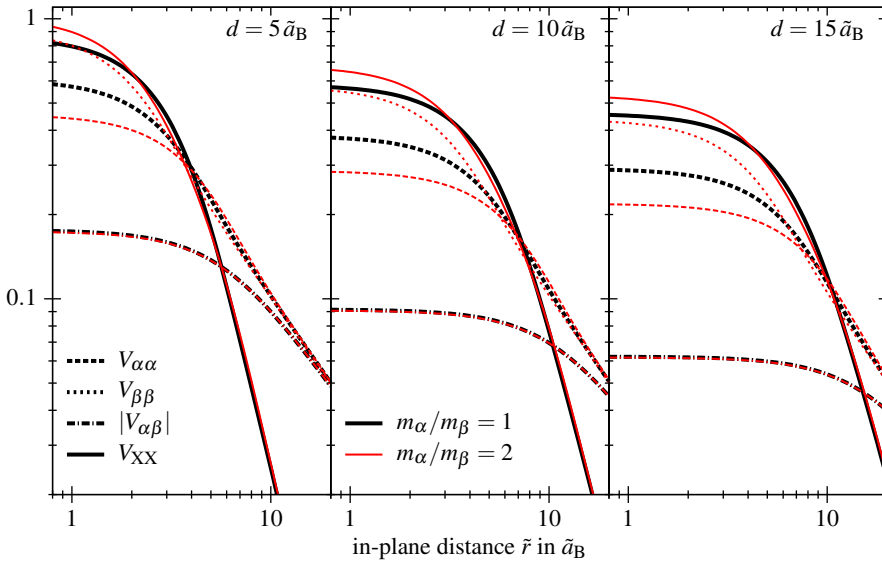


Figure 6.12 Effective exciton interaction $V_{XX}(R)$ [Eq. (6.52)] and its components $\tilde{V}_{\alpha\beta}(R)$ [Eq. (6.60)] for three dipole moments $d = 5, 10, 15$ (from left to right). Results were obtained using the Gaussian exciton density approximation [Eqs. (6.50) and (6.61)] and the classical approximation for the particle interaction. Black curves correspond to equal mass particles, red curves to $m_\alpha/m_\beta = 2$.

The exact $V_{XX}(R)$ shares the $R \rightarrow \infty$ asymptotic with the classical exciton potential $V_{XX}^{\text{cl}}(R)$ [(6.25)], but differs fundamentally on small distances. While $V_{XX}^{\text{cl}}(R)$ retains the Coulomb singularity at $r \rightarrow 0$, $V_{XX}(R)$ always converges to a finite value. This limit depends on the in-plane mass-ratio which does not affect $V_{XX}^{\text{cl}}(R)$ at all.

6.4.3 Application

The general investigation above hints that the final exciton potential may depend on only two parameters: The effective dipole moment \tilde{d} and the in-plane mass ratio $m_{\text{h}}^{\text{II}}/m_{\text{e}}$. The validity of this assumption can be checked by using the exact in-plane interactions derived from the quantum well solutions for determining first the exciton density $\rho_{\text{X}}(r)$ via matrix squaring and afterwards the smoothed out effective exciton interaction.

To this end, the effective exciton interaction $V_{XX}(R)$ has been computed for a ZnSSe/ZnSe semiconductor heterostructure. Choosing ZnSe over GaAs has some practical advantages which will be discussed at the end of this section.

Figure 6.13 displays the results for $V_{XX}(R)$ for several effective dipole moments \tilde{d} . The specific values of \tilde{d} were chosen to match those from [114] which uses $d_0 \equiv 20.41 \text{ nm} = 4.8 \tilde{a}_{\text{B}}$ as the dipole moment of a 30 nm wide ZnSe quantum

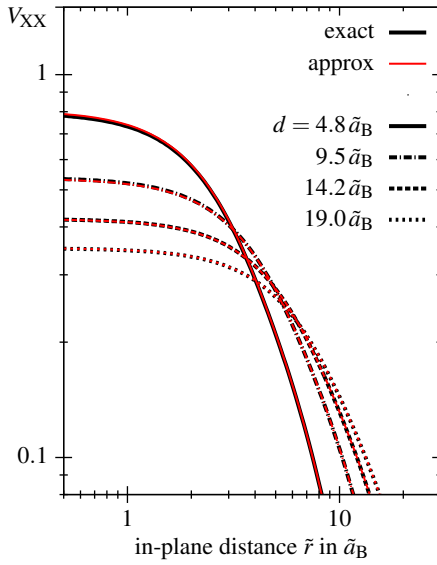


Figure 6.13 Effective interaction $V_{XX}(R)$ [Eq. (6.52)] of excitons in a ZnSSe/ZnSe well for four dipole moments d . Curves in black correspond to results obtained by numerical smoothing (6.60) of the true particle interactions $V_{\alpha\beta}(r)$ [Eq. (6.42)]. Red curves show the approximate solution using the classical point-particle interaction [Eq. (6.62) and following].

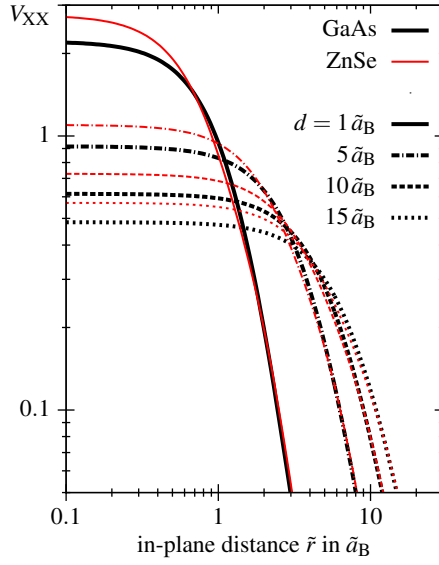
well with an applied electric field of $E/\epsilon = 20$ kV/cm. The black curve in Fig. 6.13 denote exact results whilst the red curves correspond to solutions of Eq. (6.60) using classical particle interactions. One observes a close to perfect match of both methods in the investigated range with only very minor deviations for the two low- \tilde{d} cases.

There is a simple argument why the analytical solutions of Eq. (6.60) with classical potentials works so well. In the first step, the exciton density matrix is approximated by a Gaussian. The original approximation of the exact in-plane interaction neglect the logarithmic $r \rightarrow 0$ -divergences of the latter. For the electron-hole interaction, this is of little importance as the deviation is minor to begin with and matrix squaring effectively smooths the potential, making the deviation even smaller. Consequently, the Gaussian fit to the exciton density distribution of the simplified model (6.47) also describes the exact solution very well.

Hence, the second step, smoothing the in-plane interactions with the exciton density-density correlation [Eq. (6.56)], can be simplified to Eq. (6.60) without any loss. This form smooths out the $1/r$ -divergence of the classical Coulomb potential [Eq. (6.62)], so the weaker logarithmic divergence of the exact potential disappears as well. The core region, i.e. the region where deviation of the exact potential to the Coulomb potential occur, is smaller than the width σ of the smoothing kernel. This causes *any* potential weaker than Coulomb to be smoothed to the same result.

Note that $V_{XX}(R)$ does also depend on the hole to electron mass ratio, but specifically only their *in-plane* mass ratio. This dependence enters explicitly through the width $\sigma_{\alpha\beta}$ of the Gaussian smoothing kernel [Eq. (6.61)]. Thus, the results for a specific effective dipole moment \tilde{d} vary from material to material. A compari-

Figure 6.14 Effective interaction $V_{XX}(\tilde{R})$ [Eq. (6.52)] of excitons for four dipole moments d . Curves in black show results for a AlGaAs/GaAs well with an (in-plane) mass ratio of $m_h^{\text{II}}/m_e = 1.68$; curves in red correspond to ZnSSe/ZnSe well with $m_h^{\text{II}}/m_e = 2.47$. Results are shown in effective atomic units Eq. (6.46) which differ between both cases, i.e. $\tilde{a}_B^{\text{GaAs}} = 15.9 \text{ nm}$ and $\tilde{a}_B^{\text{ZnSe}} = 4.3 \text{ nm}$ [cf. Tab. 6.1].



son of GaAs and ZnSe is shown in Fig. 6.14. ZnSe features with $m_h^{\text{II}}/m_e = 2.47$ a greater mass ratio than GaAs with $m_h^{\text{II}}/m_e = 1.68$. It has been noted before that a larger mass ratio increases the repulsion in the core region and the same trend is observed in the present case. For $r \gtrsim d$, both curves converge to the classical potential of two parallel point dipoles. Obviously, they also coincide with the classical exciton potential at this point.

Table 6.1 Parameters for semiconductor quantum wells. The values for $\text{Al}_x\text{Ga}_{1-x}\text{As}/\text{GaAs}$ correspond to $x = 0.3$. The $\text{Zn}_x\text{S}_{1-x}\text{Se}/\text{ZnSe}$ values for V_h and V_e are the maximum values for $x = 1$. With doping and other values for x , the potential depths for electrons and holes may be tuned to a certain degree. From [114] and references therein.

material		$\text{Al}_x\text{Ga}_{1-x}\text{As}/\text{GaAs}$	$\text{ZnS}_x\text{Se}_{1-x}/\text{ZnSe}$
ϵ		12.58	8.7
m_h^\perp/m_0		0.377	0.86
m_h^\parallel/m_0		0.112	0.37
m_e/m_0		0.0667	0.15
V_h	meV	163	335
V_e	meV	216	335
λ_h^\perp	$\text{nm}^2 \text{ eV}$	0.101	
λ_e	$\text{nm}^2 \text{ eV}$	0.571	
V_h^{eff}	nm^{-2}	0.806	
V_e^{eff}	nm^{-2}	0.189	
E_h^{eff}	$\text{nm}^{-3} \text{ keV}^{-1}$	39.31×10^{-6}	
E_e^{eff}	$\text{nm}^{-3} \text{ keV}^{-1}$	6.96×10^{-6}	
μ/m_0		0.0418	0.107
λ_μ	$\text{nm}^2 \text{ eV}$	0.911	0.356
\tilde{a}_B	nm	15.93	4.30
\tilde{H}_a	meV	7.187	38.47
M_X/m_0		0.179	0.52
M_X/μ		4.28	4.86
a_B^*	nm	3.73	0.885
H_a^*	meV	30.73	186.96

Crystallization of Indirect Excitons

The model from the previous chapter can be used to simulate a large number of spatially indirect excitons with the Path-Integral Monte Carlo (PIMC) method [Ch. 5] based on first principles: PIMC can accurately account for bosonic exchange symmetry with no further approximation.

This chapter presents the results from such PIMC simulations of spatially indirect excitons with a strong dipole moment. They show that the system can indeed crystallize as it has been predicted in the past [64, 65]. As noted in the introduction, crystallization requires a sufficiently strong interaction which exceeds the kinetic energy by a certain threshold. This obviously bounds the solid to low temperature regimes, i.e. the system always melts at some point when heated. In quantum systems, however, one must take the zero-point motion into account which leads to the existence of quantum phase transitions, i.e. constant-temperature melting either by compression [116, 117] or by relaxation [60, 61]. Due to the peculiar shape of the exciton interaction, the solid phase of indirect excitons shows *both* of them. The findings are summarized in a full phase diagram of spatially indirect excitons with strong dipole moments.

7.1 Model

The Hamiltonian (6.1) governs the dynamics of a system of N_e electrons in the conduction band and N_h holes in the valence band confined in a semiconductor quantum well (QW). It contains the kinetic energy, the interaction with the external electric field [Eqs. (6.2) and (6.3)] and all Coulomb pair interactions between the particles [Eq. (6.4)]. The thermodynamic properties of this system is fully described by the density operator of the electrons, $\hat{\rho}_{\mathcal{A}}^{N_e}$, and the holes, $\hat{\rho}_{\mathcal{A}}^{N_h}$

[cf. Eq. (2.14)].

A full many-body description of this system is hampered by the fermion sign problem which makes a direct numerical investigation of the fermionic density operators virtually impossible [113]. Fortunately, the system can be substantially simplified under the assumption of strongly bound indirect excitons with parallel dipole moments. In this case, the composite electron-hole system can be mapped onto $N_e = N_h = N_X$ indirect excitons. As a result, the dynamics of such a system is governed by the effective 2D-Hamiltonian (6.16)

$$\hat{H}^{\text{eff}} = -\lambda_X \sum_{i=1}^{N_X} \nabla_{\mathbf{r}_i}^2 + \sum_{i<j} V_{XX}(r_{ij}), \quad (7.1)$$

where $\lambda_X = \hbar^2/(2M_X)$ is the exciton quantumness with the effective in-plane exciton mass $M_X = m_e + m_h^{\parallel}$, \mathbf{r}_i the center of mass (com) coordinate of the i^{th} exciton and $r_{ij} = |\mathbf{r}_i - \mathbf{r}_j|$ denotes the com distance between two excitons. The complexity of the out-of-plane interaction and internal exciton structure are hidden in the effective inter-exciton interaction V_{XX} . The detail on the mapping procedure and the computation of the effective potential V_{XX} are explained in Chapter 6.

The Hamiltonian (7.1) serves as model which is investigated in this chapter. As excitons are composite bosons [118, 119], the thermodynamic properties are determined by the bosonic density operator $\hat{\rho}_S^{N_X}$ [cf. Eq. (2.13)]. Treating excitons as bosons implies that electrons and holes may only exchange coordinates as a pair. Such a bosonization procedure has been used in many theoretical analysis [120]. One might worry that this causes deviations due to the original fermionic nature of the excitons' components [121, 122]. However, as long as excitons are stable and strongly repulsive, the error has been found negligible [114].

The relevant parameter which determines the phase of the system is the *coupling parameter*, the ratio of average potential, $\langle V \rangle$, to kinetic energy, $\langle T \rangle$ [58]. One can approximate the average potential energy as $\langle V \rangle \approx V(\bar{r})$ where \bar{r} is the average inter-particle distance. The expression for the kinetic energy depends on the nature of the system.

In classical two-dimensional systems, the the average kinetic energy is given by $\langle T \rangle_{\text{cl}} = k_B T$. For the limiting cases of the effective exciton potential, one recovers the *Coulomb coupling parameter* Γ_C and *dipole coupling parameter* Γ_d defined as

$$\Gamma_C = \frac{\text{Ha}^*}{k_B T} \frac{a_B^*}{\bar{r}}, \quad \Gamma_d = \frac{\text{Ha}^*}{k_B T} \frac{d^2}{a_B^{*2}} \left[\frac{a_B^*}{\bar{r}} \right]^3, \quad (7.2)$$

with the exciton Bohr radius $a_B^* = \epsilon \hbar^2 / (e^2 M_X)$ and the exciton Hartree $\text{Ha}^* = 2\lambda_X / a_B^*$.

In (bosonic) quantum systems, the average kinetic energy is given by $\langle T \rangle_{\text{qm}} = 2\lambda_X/\bar{r}^2$. Again, the limiting cases of the potential are described by different coupling parameter. In the Coulomb high density limit, one has the *Coulomb coupling parameter* r_s and, in the low-density dipole limit, one has the *dipole coupling parameter* r_d . Their definitions are readily obtained when inserting the corresponding potentials into Eq. (1.1), i.e.

$$r_s = \frac{\bar{r}}{a_B^*}, \quad r_d = \frac{d^2}{a_B^{*2}} \frac{a_B^*}{\sqrt{\pi}\bar{r}}, \quad (7.3)$$

where $a_B^* = \epsilon\hbar^2/(e^2 M_X)$ is the effective exciton Bohr radius. By convention, the quantum dipole coupling parameter has an additional factor of $1/\sqrt{\pi}$ [61, 114]. These definitions imply the relation

$$r_d = \frac{d^2}{a_B^{*2}} \frac{1}{\sqrt{\pi}r_s}. \quad (7.4)$$

Instead of choosing effective exciton Bohr radius, one is certainly free to use the more familiar effective electron Bohr radius $a_{\text{Be}}^* = 2\lambda_X\epsilon/e^2 = \hbar^2\epsilon/(e^2 m_e)$ as unit of length. The full transformation to effective atomic units reads [cf. Appx A]

$$r \rightarrow r^* a_{\text{Be}}^*, \quad E \rightarrow E^* \text{Ha}_e^* = E^* \frac{2\lambda_e}{a_{\text{Be}}^{*2}}. \quad (7.5)$$

In this system of units, the definition (7.2) of the classical coupling parameters remains unaffected, but their quantum counterparts Eq. (7.3) explicitly depend on the mass ratio M_X/m_e . The definitions then read

$$\Gamma_C = \frac{\text{Ha}_e^*}{k_B T} \frac{a_{\text{Be}}^*}{\bar{r}}, \quad \Gamma_d = \frac{\text{Ha}_e^*}{k_B T} \frac{d^2}{a_{\text{Be}}^{*2}} \left[\frac{a_{\text{Be}}^*}{\bar{r}} \right]^3, \quad (7.6)$$

$$r_s = \frac{M_X}{m_e} \frac{\bar{r}}{a_{\text{Be}}^*} \equiv \frac{M_X}{m_e} r_{\text{se}}, \quad r_d = \frac{M_X}{m_e} \frac{d^2}{a_{\text{Be}}^{*2}} \frac{a_{\text{Be}}^*}{\sqrt{\pi}\bar{r}}, \quad (7.7)$$

where the usual electron Coupling parameter or *Brueckner parameter* r_{se} is introduced.

Table 7.1 Effective electron atomic units. From [114].

material		AlGaAs/GaAs	ZnSSe/ZnSe
M_X/m_e		2.68	3.46
a_{Be}^*	nm	9.98	3.07
Ha_e^*	meV	11.47	53.93

From the definitions of the coupling parameters Eqs. (7.2) and (7.3), it is clear that the phase of the system depends on three external parameters, the reduced (inverse) temperature T^* (β^*), the reduced dipole moment d^* and the reduced density n^* which determines the average particle spacing \bar{r} . They are defined as

$$\frac{1}{\beta^*} = T^* \equiv \frac{k_B T}{\text{Ha}_e^*}, \quad n^* \equiv \frac{a_{\text{Be}}^{*2}}{\pi \bar{r}^2}, \quad d^* \equiv \frac{d}{a_{\text{Be}}^*}. \quad (7.8)$$

The dipole moment d only determines the specific interaction potential of the model (7.1). In a Monte-Carlo simulation the system, one typically works within the canonical ensemble which is defined by the inverse temperature β and the density $n = N_X/V$. The former enters into the acceptance ratios of configuration changes and the latter is controlled by preparing a system of N_X particles and choosing the size of the simulation box accordingly. Furthermore, a Path-Integral Monte-Carlo simulation [Ch. 5] takes bosonic quantum exchange into account. Hence, the simulation works on *first principles* – no further approximations are necessary for the given model (7.1).

7.2 Simulation Results

The effective exciton potential parametrically depends on two quantities, the dipole moment d and the in-plane mass ratio m_h^{\parallel}/m_e . In a wide quantum well setup, the first can be controlled by the well width and the applied electric field strength while the latter is determined by the material choice. Since ZnSe has superior properties regarding experimental realizations, it is the material of choice for which the results in this chapter are computed. Figure 7.1 shows V_{XX} for several values of d . A detailed explanation of the behavior is given in Ch. 6.

In a first step, the approximate boundaries of the solid phase have been computed for a fixed dipole moment. Its value is chosen to $d = 13.3 a_{\text{Be}}^*$ (red curve in Fig. 7.1) – strong dipole moments are preferable as the relation of the relevant coupling parameters (7.4) suggests stabilization of the solid with increasing d . The system (7.1) with the given inter-action potential $V_{XX}(r; d)$ has been simulated extensively using PIMC [Ch. 5]. Thereby, the number of excitons is kept fixed to $N_X = 60$ while the (inverse) temperature β and the density n are varied by several orders of magnitude to traverse the canonical configurational space. Naturally, the excitons are treated as bosons and the simulation box has periodic boundary conditions.

The relevant quantity to detect crystallization is the pair distribution function [PDF], $g(\mathbf{r})$. Being diagonal in coordinate representation, the PDF can be easily estimated with PIMC [Eq. (5.66)] and converges very fast. Hence, a rather low number of Monte Carlo steps is sufficient (i.e. ~ 200 – $1000k$ steps) which makes it an ideal tool to raster the configurational space efficiently.

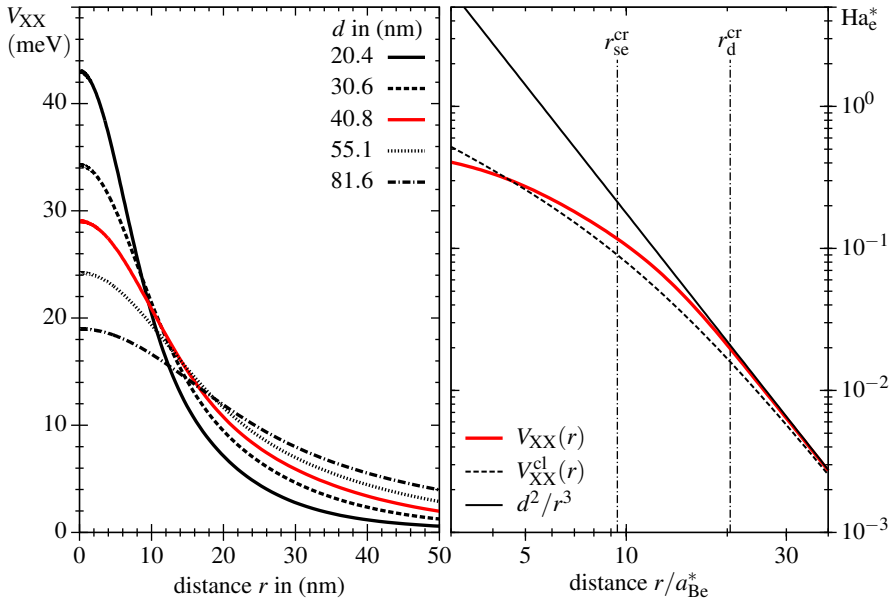


Figure 7.1 Effective exciton interaction V_{XX} in a ZnSe quantum well for varying strengths of the dipole moment d . The righthand panel shows the potential in a double logarithmic plot for $d = 13.3 a_{Be}^*$ (red curve). For comparison, the dipole potential d^2/r^3 and the classical exciton potential V_{XX}^{cl} [Eq. (6.25)] are also shown.

The PDF denotes the probability to find a pair of particles separated by the distance \mathbf{r} . In an ideal gas, the PDF equals unity everywhere. Otherwise, the PDF starts at 0 (known as the *correlation hole*) but asymptotically converges to unity. Increasingly strong modulations signal emergence of spatial order. While the usual pair distribution function $g(r) = g(|\mathbf{r}|)$ only accounts for translational order, the full 2D PDF resolves orientational modulations as well. Orientational order is absent in the liquid which eases the distinction of the phases. Visual inspection is already sufficient to locate the transitions to the solid phase.

Doing so, one can identify three transitions in the present system – one while keeping the density fixed (shown in Fig. 7.2) and two while keeping the temperature fixed (shown in Fig. 7.3). The 2D PDF is displayed as color coded heat map. The black spot indicates the correlation hole which is centered around the pinned reference exciton. Modulations around unity are shown in green (red) for negative (positive) deviations. In the figures, the solid phase is characterized by a regular hexagonal grid of yellow dots. The liquid lacks clear orientational modulations but still shows concentric modulations.

While all panels show the transition to the solid, the nature of the transition is fundamentally different and is explored in the following.

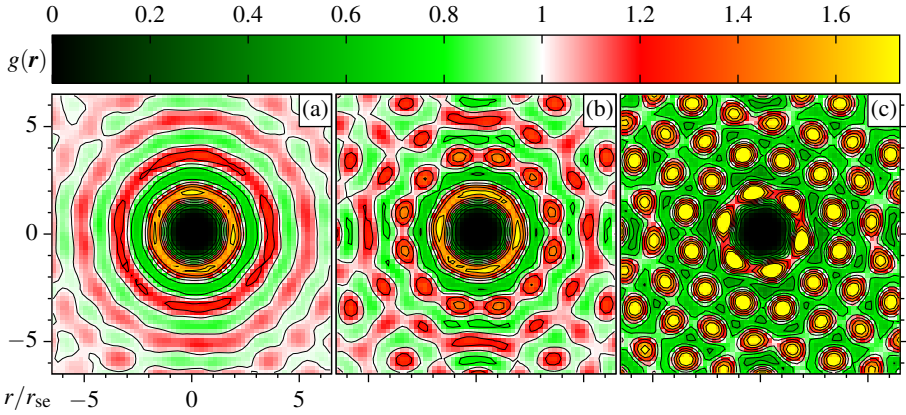


Figure 7.2 Constant density freezing for $na_{Be}^{*2} = 0.0035$ illustrated with the 2D pair distribution function $g(\mathbf{r})$ relative to a fixed particle in the center. The temperature decreases from left to right: $k_B T / Ha_c^* = 1.74 \cdot 10^{-3}$ (a), $1.38 \cdot 10^{-3}$ (b), and $1.08 \cdot 10^{-3}$ (c).

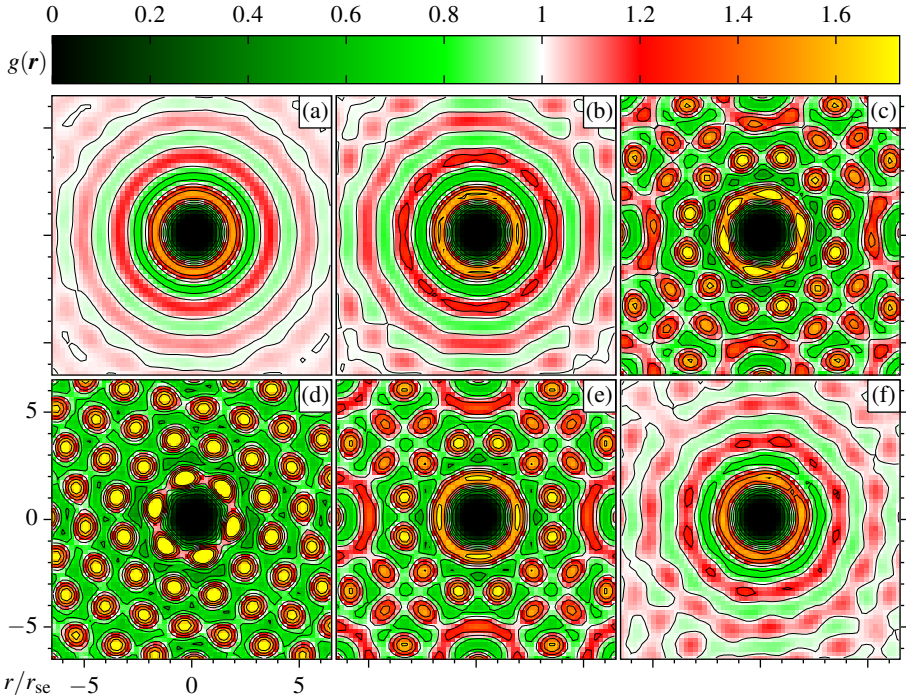


Figure 7.3 Isothermal transitions for $k_B T_1 = 0.001 Ha_c^*$ illustrated with $g(\mathbf{r})$. The top row shows freezing for $na_{Be}^{*2} = 0.84 \cdot 10^{-3}$ (a), $1.3 \cdot 10^{-3}$ (b), and $1.7 \cdot 10^{-3}$ (c) while the bottom row shows melting for $na_{Be}^{*2} = 3.5 \cdot 10^{-3}$ (d), $3.9 \cdot 10^{-3}$ (e), and $4.4 \cdot 10^{-3}$ (f).

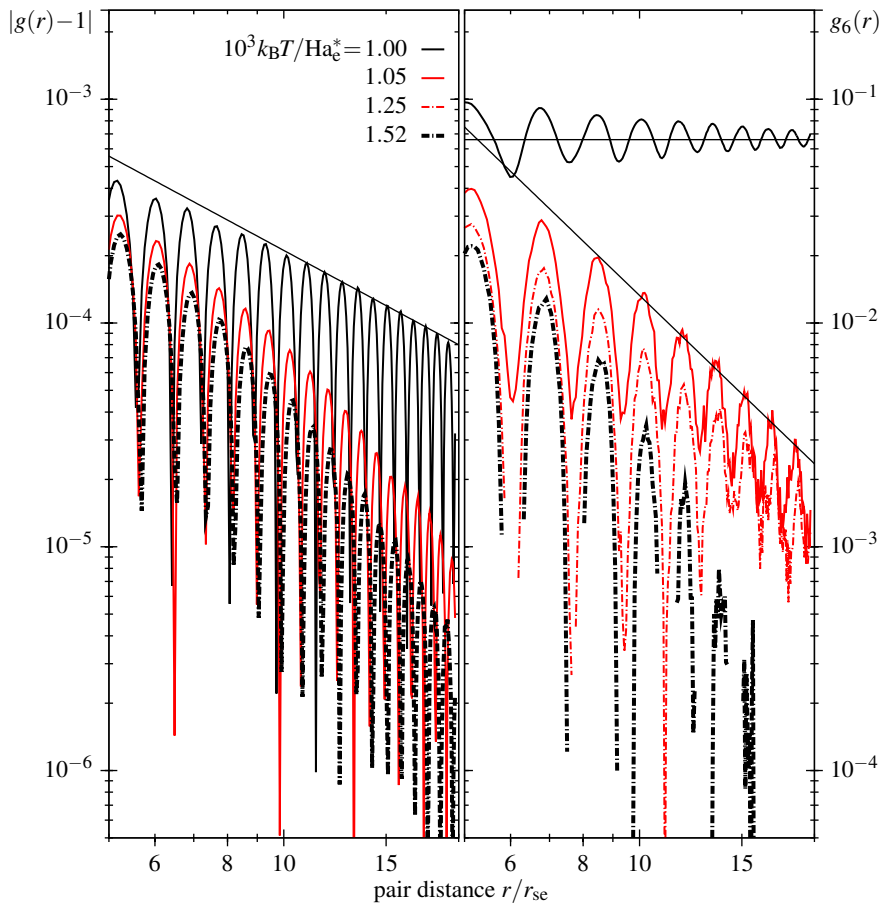


Figure 7.4 Constant density freezing. Translational correlation function $|g(r) - 1|$ (left) and bond-order correlation function $g_6(r)$ (right) at $na_{Be}^{*2} = 0.0022$.

7.2.1 Normalfluid-Solid Transition

The defining feature of a conventional solid is spatial long-range order. The existence or absence of translational long range order is detected from the asymptotes of the angle-averaged function pair distribution function [PDF] $g(r)$ for large $r = |\mathbf{r}|$. While the simulations for $N_X = 60$ provide a reasonable estimate of the parameter range where the transition to the solid can be expected, such small scale simulations only extend to 3 peaks of the PDF. In order to judge the asymptote of the PDF, the particle number must be increased significantly. Using the WA, such simulations – while still including bosonic particle exchange – are certainly possible. However, the particle number is a fluctuating quantity with WA, determined by the chemical potential μ . Preliminary runs are necessary to find the “correct” value of μ for the desired N_X . In this sense, the results presented in this subsection

are recorded for the “fixed” number of $N_X = 500$ excitons.

As discussed in Ch. 3, true long-range translational order does not exist in 2D systems [54]. Instead, the Kosterlitz-Thouless-Halperin-Nelson-Young (KTHNY) theory for freezing predicts a solid phase characterized by *quasi* long-range translational order [79]. So while the PDF always converges to unity in the limit of large pair distances, $r \rightarrow \infty$, it changes from an exponential decay in the liquid to an algebraic decay in the solid phase.

The transition is illustrated in the left panel of Fig. 7.4. Shown is not the PDF directly but the related correlation function $|g(r) - 1|$ which accounts for the deviation of the PDF from unity and decays to zero. The long-range behavior can be read off the enveloping curve. In the log-log plot, algebraic decay implies a linear envelope which is the case for $k_B T_1 = 0.001 \text{ Ha}_e^*$ data (solid black line). Contrastingly, The envelope of the $k_B T_1 = 0.00152 \text{ Ha}_e^*$ data (dash-dotted black line) curves downward indicating the absence of any long-range order.

Additionally, KTHNY theory expects true long-range orientational order in the solid. Its existence follows from the asymptote of the bond-order correlation function $g_6(r)$ [cf Eq. (5.67)]. The right panel of Fig. 7.4 displays the results for the transition. The $k_B T_1 = 0.001 \text{ Ha}_e^*$ data (solid black line) clearly exhibits long-range order as $g_6(r)$ converges to a finite value for $r \rightarrow \infty$.

Within KTHNY theory, there is no direct melting transition to the liquid without any long-range order, but two continuous transition with an intermittent hexatic phase characterized by quasi long-range orientational order [cf. Tab 3.2]. Indeed, the simulation results for $g_6(r)$ support this scenario. Figure 7.4 marks data which fall into the hexatic phase in red, namely the results obtained for $k_B T_1 = 0.00105 \text{ Ha}_e^*$ and $k_B T_1 = 0.00125 \text{ Ha}_e^*$. The hexatic phase does not exhibit long-range translational order as shown in the left panel of Fig. 7.4.

The KTHNY scenario for melting assumes two separate continuous transitions mediated by unbinding of dislocation pairs and breaking of dislocations into point defects, respectively. It does not rule out the possibility of a direct first order transition from solid to liquid [79]. The existence or absence of the hexatic phase in 2D systems is not rigorously proven up to date – there are studies supporting both scenarios. A recent work from Clark *et al.* [123] claims its existence in quantum Coulomb systems composed of boltzmannons. On the other hand, classical Coulomb systems are thought to have a clear first order phase transition [124] and, in Yukawa and dipole systems, the hexatic phase seems to be of a transient nature which disappears in true equilibrium [125].

The difficulties arise as equilibration may be extremely long for large systems (e.g. with up to $N = 10^6$ particles) which is troublesome even in classical simulations. In the present case, neither the particle number nor the accessible simulation time is sufficient to rule out such effects. Indeed, when monitoring the number of defects, there is an abrupt increase at the melting temperature which is inconsistent with KTHNY theory. Additionally, one normally observes a region of phase

coexistence for first order transitions when simulated with a finite systems. The discovered “hexatic” phase may be a relic of such.

7.2.2 Superfluid-Normalfluid Transition

Figure 7.3 indicates that the solid phase is confined to limited density range. The nature of the isothermal transitions themselves is explored in the following section. This section addresses the question what happens if one chooses a constant density cooling path, as in the previous section, but outside the density range of the solid.

Since the model deals with an interacting bosonic system, cooling without crystallization leads to the spontaneous emergence of quantum coherence – the system crosses normalfluid-superfluid transition. The natural quantity to detect this phase transition is the superfluid density n_s . In macroscopic PIMC simulations, n_s can be estimated with the winding number formula (5.80).

Being a 2D system, the transition falls into the XY universality class which is covered by the Berezinskii-Kosterlitz-Thouless (KT) theory [55, 56] discussed in Ch. 3. As such, the critical temperature relates to the critical superfluid density as [cf. Eq. (3.19)]

$$k_B T_{\text{cr}} = \frac{\pi}{2} n_s \frac{m_e}{M_X} \text{Ha}_e^* . \quad (7.9)$$

At T_{cr} , the superfluid density jumps from zero to n_s . This is a *universal* property [82], i.e. a lower critical temperature always implies a lower critical superfluid density. Finite system do not show a sudden jump, but a smoothed out curve when plotting n_s vs. temperature. However, one can locate the critical temperature on this curve at the point which satisfies (7.9).

Part of the critical behavior is the divergence of the correlation length $\xi(T)$ according to [126]

$$\xi(T) \propto \exp \left[\frac{a}{\sqrt{t}} \right] , \quad t \equiv \left(\frac{T}{T_{\text{cr}}} - 1 \right) , \quad (7.10)$$

with a being a non-universal temperature-density-dependent scaling factor. In a finite system, the system size $L = \sqrt{N_X}$ adopts the role of ξ somewhere in the vicinity of the critical point. When comparing the critical temperatures $T_{\text{cr}}(L)$ measured for different system sizes, Equation (7.10) implies the scaling

$$T_{\text{cr}} = T_{\text{cr}}(L) - \frac{b}{\ln^2 L} , \quad (7.11)$$

where b is a constant and T_{cr} the true critical temperature in the thermodynamic limit. More details on this method can be found in [70].

In summary, one records the critical temperatures on the same cooling path for several particle sizes according to Eq. (7.9) and extrapolates to the thermodynamic limit with Eq. (7.11). Figure 7.6 displays the results obtained for several densities.

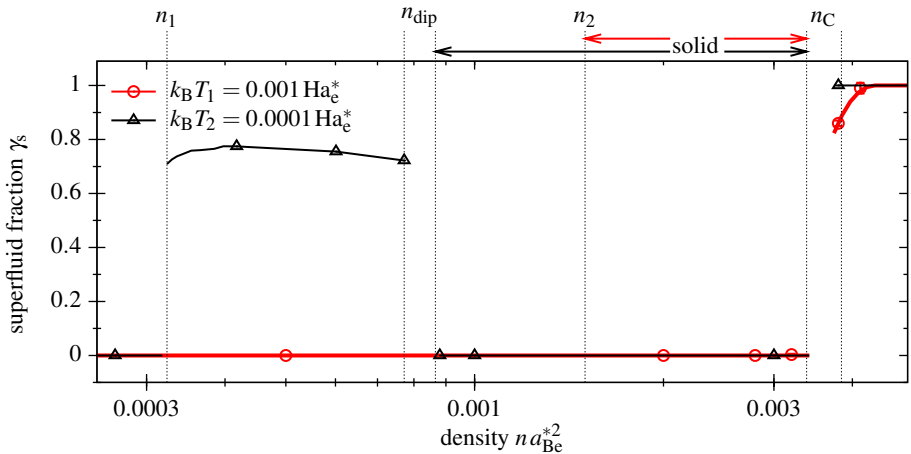


Figure 7.5 Superfluid fraction γ_s , Eq. (5.80), vs. density for two temperatures. Data points with error bars are PIMC results, lines are a guide to the eye.

7.2.3 Superfluid-Solid Transition

From the discussion of the previous sections, it is clear that there must be a transition from the solid to the superfluid phase by changing the density while keeping the temperature fixed. This transition is detected by the pair distribution function *and* the superfluid fraction simultaneously. The measurements of the latter along two isothermal melting paths are displayed in Fig. 7.5. The spanning arrows on top of the plot indicate where the PDF indicate the crystal phase [cf. Fig. 7.3].

Consider the solid at a low temperature of $k_B T = 0.0001 \text{ Ha}_e^*$. When increasing the density while the temperature is kept fixed, one observes that the system melts at $n_C a_{Be}^{*2} \approx 0.0036 \pm 0.003$ accompanied by a jump of the superfluid fraction γ_s from 0 to 1 (black curve in Fig. 7.5). Pressure melting is a feature of Coulomb-like systems [117] where the quantum coupling parameter decreases with density [cf. Eq. (7.3)]. Its value at the transition is $r_{se}^{cr} = 9.4 \pm 0.3$ which persists even at zero temperature. When shifting the melting path to higher temperatures, melting and the onset of superfluidity decouple above $k_B T \gtrsim 0.001 \text{ Ha}_e^*$ – the system crosses into the normalfluid phase before settling into the superfluid phase. The nature of these transitions is discussed in the previous two subsections. Figure 7.5 includes the data for a melting path at $k_B T = 0.001 \text{ Ha}_e^*$ (red curve). Here, the superfluid fraction γ_s does not jump immediately to 1 which is expected due to the closeness to the KT transition in vicinity of the triple point. Moving away from the KT transition, γ_s quickly approaches unity at higher densities.

Now consider the behavior when lowering the density starting from the original spot at $k_B T = 0.0001 \text{ Ha}_e^*$ in the solid. Again keeping this temperature fixed, one observes a similar melting transition to the superfluid phase at $n_{dip} a_{Be}^{*2} \approx$

0.00078 ± 0.00005 which, again, persist to zero temperature. The difference is that the system melts by relaxation or, alternatively, freezes upon compression. Such transitions are known to occur in dipole systems where the relevant coupling parameter increases with density [cf Eq. (7.3)]. Its value of $r_d^{\text{cr}} = 17 \pm 1$ corresponding to n_{dip} agrees with values obtained for pure 2D dipole systems [60–62].

Note that the superfluid fraction does not directly jump to unity. On the low-density side of the crystal, the melting path crosses the transition line already quite close to the triple point. Hence, when relaxing along the high-temperature path at $k_B T = 0.001 \text{ Ha}_e^*$ (red line in Fig. 7.5), the system already melts at a higher density of $n_2 a_{\text{Be}}^{*2} \approx 0.0017$ but never crosses into the superfluid phase upon further relaxation. This is expected as, on one hand, the melting transition is located on the normalfluid side of the universal temperature-density relation stated by the KT criterion [cf. (7.9)]. Since, on the other hand, the relation is strictly monotonic, the system can only leave the superfluid phase upon relaxation. This is also the case at $n_1 a_{\text{Be}}^{*2} \approx 0.00033$ ($r_d = 11$ [70]) for the low-temperature path.

As a closing remark, quantum transitions from a superfluid to a solid are first order transitions. In the conducted simulations, coexistence of both phases is observed at both transition lines. These regions are delimited by vertical lines in Fig. 7.5. The value of γ_s fluctuates wildly from 0 to a finite value in these regions.

7.3 Phase Diagram

Figure 7.6 summarizes the findings in a full n - T phase diagram of indirect excitons. The parameter space is patterned into the three observed phases: normalfluid (unshaded), superfluid (striped red), and solid (criss-crossed). The solid divides the superfluid region into two disconnected areas. A fourth phase is sketched at the righthand border where the system is expected to transform into an electron-hole plasma. The pressure dissociation of excitons, known as *Mott effect* [127] (see also [128, 129]), is not included in the model as excitons are assumed stable *a priori*, but can be estimated to densities at around $n_M a_{\text{Be}}^{*2} = 0.03$ ($r_{\text{se}}^M = 3.2 \pm 0.4$) [130–132]. Though not part of the present study, the electron-hole plasma can exhibit a rich phase diagram on its own, like hole crystal embedded in an electron liquid [116, 133].

The existence of two quantum transitions – even in the ground state – is the most striking feature of the exciton phase diagram. The transitions are located at $r_d^{\text{cr}} = 17 \pm 1$ and $r_{\text{se}}^{\text{cr}} = 9.4 \pm 0.3$ (denoted with vertical dashed lines in Fig. 7.6) which translates to $n_{\text{dip}} a_{\text{Be}}^{*2} \approx 0.00078 \pm 0.00005$ and $n_C a_{\text{Be}}^{*2} \approx 0.0036 \pm 0.003$, respectively. Pressure melting is a signature of Coulomb systems including the Wigner crystal of strongly correlated electrons [117], the hypothetic crystals of carbon and oxygen nuclei in the core of white dwarf stars and nuclear matter in the crust of neutron stars. Remarkable is the fact that all of the latter take place in

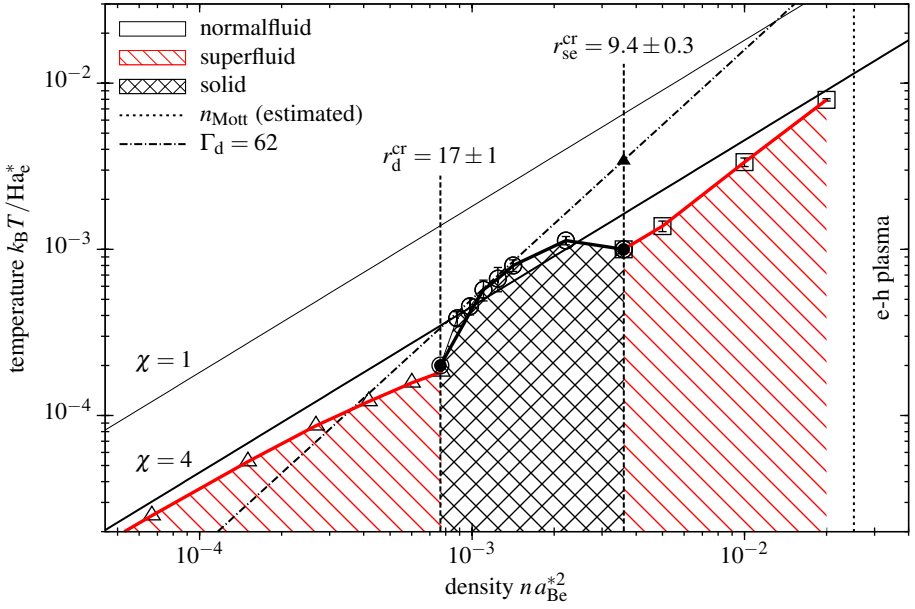


Figure 7.6 Phase diagram of 2D indirect excitons with $d = 13.3 a_{\text{Be}}^*$. Circles mark PIMC simulation results, data for triangles is taken from [70]. Vertical dashed lines indicate density induced quantum freezing (melting) transitions located at $r_d^{\text{cr}} = 17 \pm 1$ and $r_{se}^{\text{cr}} = 9.4 \pm 0.3$. Stars mark the two triple points. The normal fluid–superfluid phase boundary is marked by the red line and is below the ideal estimate $T_{KT,max}$ according to Eq. (7.9), cf. thick solid line labeled $\chi = 4$. Line T_{dip} marks the freezing transition of a classical 2D dipole system. Vertical dotted line is an estimate for the exciton pressure ionization n_{Mott} (Mott effect).

charged systems while neutral matter, in general, crystallizes upon compression. As neutral particles, excitons show the characteristics of a dipole system at low densities while “remembering” the Coulomb origin of their components when brought close at higher densities.

It stems from the peculiar form of the exciton-exciton interaction V_{XX} . This is readily explained if one considers distances in proximity to the average inter-particle distance defined by the density as the effective range of the potential. Vertical dashed lines mark the average inter-particle distance at the quantum transitions in Fig. 7.1. One observes that the slope of the potential at r_d^{cr} essentially resembles the classical dipole potential while at r_{se}^{cr} , it shares strong similarities with the softer Coulomb potential.

The quantum melting lines end in the triple points to high-temperatures denoted by black dots in Fig. 7.6. The line connecting the triple points marks the melting line bounding the solid phase. The nature of this transition is discussed in Sec. 7.2.1. The potentially adjacent hexatic phase to the high temperature side is not explicitly marked – within the resolution of Fig. 7.6 it would squeeze in a

thin strip above the melting line. The melting transition can be compared to the that of classical 2D dipoles. For the latter, Kalia *et al.* [59] showed the existence of a universal first-order melting transition at $\Gamma_d^{\text{cr}} = 62 \pm 4$. This limit is denoted as dash-dotted line in Fig. 7.6. In a study of quantum dipoles [61], this estimate is shown to be valid only in the limiting case of strong coupling, $r_d \gg r_d^{\text{cr}}$. The same trend is observed for the present system, but here the validity holds only up to intermediate densities. At higher densities, deviations of V_{XX} from the classical dipole potential V_D become important.

Usually, the quantum degeneracy parameter χ serves as an estimate of the importance of quantum effects for given external parameters. For a two-dimensional system, it is defined as

$$\chi = n \Lambda^2, \quad \Lambda = \frac{2\pi\hbar}{\sqrt{2\pi M_X k_B T}}, \quad (7.12)$$

where Λ is the free particle thermal wave-length. Values smaller than unity, i.e. $\chi < 1$, lead to expect classical behavior while $\chi > 1$ suggests quantum behavior. The parameter space is divided into these two regimes by the $\chi = 1$ line [cf. Fig. 7.6]. The validity of the classical melting transition Γ_d^{cr} at intermediate densities suggests that this transition is not governed by quantum effects. As all phase boundaries fall in the $\chi > 1$ regime, this conclusion comes as some surprise.

Quantum effects are clearly important for the normalfluid-superfluid transition which is marked with red lines in Fig. 7.6 curving outward from the triple points. The transition is governed by the Berezinskii-Kosterlitz-Thouless (KT) scenario discussed in Sec. 7.2.2. The universal condition for the critical point (7.9) has a straightforward upper limit when one replaces the exact superfluid density with the full density. The physical picture is a hypothetical jump of the superfluid fraction γ_s to unity at the transition point. Inserting Eq. (7.9) into the definition (7.12) of the quantum degeneracy parameter χ , one sees that this upper bound corresponds to the condition $\chi = 4$.

Due to the universality of Eq. (7.9), the deviation of the actual transition from this upper bound is directly proportional to $1 - \gamma_s$ at the critical point. As seen in Fig. 7.6, the $\gamma_s = 1$ limit is approached when moving away from the triple points. However, this limit is never reached. At high densities, the system ionizes at the Mott density. Since unbound electrons and hole are naturally fermions, the superfluid phase ceases to exist. At very low densities, the system can be described as a dilute 2D quantum Bose gas. In this case, an analytical approximation for the critical temperature and superfluid fraction was derived and tested in [134, 135]. A recent study by Filinov *et al.* [70] discusses the connection up to the onset of crystallization for dipole systems. PIMC data marked by triangles in Fig. 7.6 is taken from this reference.

All results obtained up to this point have been computed for the fixed dipole moment $d = 13.3 a_{\text{Be}}^*$. According to the relation (7.4), the solid phase stabilizes

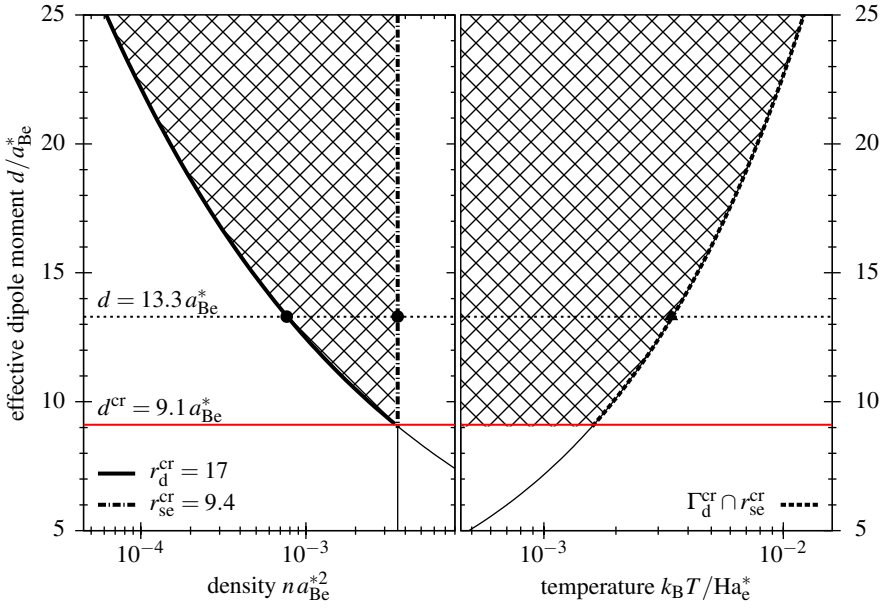


Figure 7.7 The left panel shows the density range of solid phase vs. dipole moment d . The lower limit is given by $r_d^{\text{cr}} = 17 \pm 1$ whilst the upper limit is set by $r_{\text{se}}^{\text{cr}} = 9.4 \pm 0.3$. A solid phase does not exist below a critical dipole moment $d^{\text{cr}} = 9.1 \pm 0.3 a_{\text{Be}}^*$ (red line). In the right panel, the curve labeled $\Gamma_d^{\text{cr}} \cap r_{\text{se}}^{\text{cr}}$ marks an estimate for the maximum temperature of the solid phase.

with increasing d . Together with the critical coupling parameters $r_{\text{se}}^{\text{cr}}$ and r_d^{cr} , one can easily extrapolate the low-temperature phase boundaries to other values of d which is depicted in the left panel of Fig. 7.7. In the chosen system of units, only r_d depends on d [cf. Eq. (7.3)]. Hence, an increase of d only reduces the low-density boundary of the crystal phase. The $r_{\text{se}}^{\text{cr}}$ boundary is unaffected which has been confirmed in other simulations [114].

The most interesting aspect is the existence of a critical dipole moment d^{cr} . With Eq. (7.4), its value can be determined to $d^{\text{cr}} = 9.1 \pm 0.3 a_{\text{Be}}^*$. Below this point a solid exciton phase does not exist (see red line in Fig. 7.7). Moving in the opposite direction to very large dipole moments, the system will dissociate into separate electron and hole layers at some point. Since the model treats excitons as unbreakable entities, it cannot show this effect.

The thermal boundary of the solid can be estimated from the classical dipole melting transition at $\Gamma_d^{\text{cr}} = 62$. A rough estimate is obtained when using its crossing point with the quantum melting line at $r_{\text{se}}^{\text{cr}} = 9.4$ (black triangle in Fig. 7.6). One obtains a quadratic scaling law of the maximum temperature with d which is shown in right panel of Fig. 7.7.

Conclusion

The main focus of the present work was the study of correlation effects in a low-temperature gas of indirect excitons. As motivated in the introduction, indirect excitons offer a number of attractive features: a strong dipole-type interaction, the suppression of biexciton or trion formation [66, 67], the comparatively long radiative life time [49] and the external controllability of the density and dipole moment [33, 50, 51].

Experiments have confirmed the existence of spontaneous onset of quantum coherence [32, 33] and superfluidity [31] in systems of indirect excitons. The possibility of exciton crystallization has been considered [64, 65], but experimental evidence is still missing [51]. For this work, numerical and analytical methods have been employed to compute an effective interaction for indirect excitons. Subsequently, extensive numerical simulations were performed to compute the full phase diagram of a system of indirect excitons. The main findings are summarized in the following sections.

8.1 An Effective Interaction for Indirect Excitons

In Chapter 6, it has been demonstrated how an electron-hole bilayer system can be mapped onto a two-dimensional system of excitons. The effective exciton interaction $V_{XX}(R)$ hides the complexity of the out-of-plane confinement and the internal fluctuations of the exciton themselves. The interaction shows a dipole-like asymptotic decay, but differs dramatically at small distances. The classical approximation of the exciton interaction $V_{XX}^{\text{cl}}(R)$ already shows this, it converges to a Coulomb-like potential for $R \lesssim d$. The improved model includes an additional smoothing as the particles are not point-like. The result is an effective potential which converges to a fixed value at $R = 0$.

The comparison of a full numerical computation to analytical approxima-

tions shows that $V_{XX}(R)$ depends parametrically on two quantities, the dipole moment d and the in-plane effective mass ratio $m_h^||/m_e$. While d is certainly influenced by other out-of-plane parameters like the out-of-plane mass ratio or the electric field strength, neither of the latter influences $V_{XX}(R)$ directly – under the condition that d is sufficiently strong, i.e. $d \gg \epsilon \hbar^2 / (e^2 \mu_X)$ where μ_X is the reduced mass of the exciton. In this case, an analytical expression for $V_{XX}(R)$ is given by Eq. (6.60) when evaluated with the classical inter-particle interactions Eqs. (6.22) and (6.23).

One must only consider the out-of-plane problem to determine the parameters necessary to realize a specific dipole moment d . The dependence of d on the parameter space for a mass symmetric electron-hole pair is summarized in Fig. 6.6 from which the mass asymmetric case can be constructed graphically.

An interesting consequence is that the validity of $V_{XX}(R)$ naturally generalizes to any experimental realization of indirect excitons yielding the desired dipole moment d . The only condition is a reasonably strong electron-hole separation. So instead of the single wide quantum well one could use the alternative double quantum well setup [33]. The latter has the advantage that the temperature condition (6.34) for achieving the necessary localization does not apply, or, more specifically, applies to both quantum wells independently. So, in theory, one does not need temperature as low as for the single wide quantum well setup. The disadvantage of this approach is that quantum well width fluctuations become much more important and may affect the effective exciton interaction. They are not considered here, as their influence has been found negligible for wide quantum wells [66]. In conclusion, the optimal experimental setup would try to combine the positive aspects of both setups: two reasonable wide quantum wells with an external electric field.

8.2 Conditions for the Crystallization of Indirect Excitons

Based on first principle PIMC simulations [Ch. 5] and an effective composite boson model [Ch. 6], the complete phase diagram of a system of indirect exciton has been computed. Above a critical dipole moment, $d^{\text{cr}} \approx 9.1 a_B^*$, the system exhibits a crystal phase with a unique property: The solid features two quantum melting transitions – a low-density boundary at $r_d^{\text{cr}} \approx 17$ and a high-density boundary at $r_{\text{se}}^{\text{cr}} \approx 9.4$ – which persist at zero temperature. The driving force behind this behavior is the non-trivial form of the effective exciton interaction potential V_{XX} .

The critical coupling parameter for the low-density quantum transition, $r_d^{\text{cr}} = 17 \pm 1$, is in agreement with studies of pure dipole systems [60–62]. In this limit, the improved model for the exciton interaction adds little, since the indirect excitons are accurately approximated by polarized point-dipoles. On the other hand, the critical coupling parameter for the Coulomb-like pressure melting, $r_{\text{se}}^{\text{cr}} = 9.4 \pm 0.3$,

deviates strongly from the melting point of electron Wigner crystals at $r_{se}^{cr} \approx 37$ [117].

For the melting transition to high temperatures, the critical classical dipole melting parameter $\Gamma_d^{cr} \approx 62$ [59] applies to the present case where the dipole approximation of the potential holds. Otherwise, Γ_d^{cr} overestimates the critical temperature. Nevertheless, it provides a reasonable guideline for an experimental realization.

The results presented in Ch. 7 have been computed with a potential V_{XX} specifically designed for the in-plane mass ratio of ZnSe semiconductors [Fig. 7.1]. However, the difference between potentials with other in-plane mass ratios is close to negligible in the density range relevant for the crystal phase [cf. Fig. 6.14]. Hence, the results from Figs. 7.6 and 7.7 can be adapted to generic materials inserting the appropriate expressions for the dimensionless units.

Figure 7.6 presents the results for an effective dipole moment of $d = 13.3 a_{Be}^*$. Using the values from Tab. 6.1, one can estimate the quantum well width necessary to achieve this dipole moment. One obtains $L \approx 148$ nm for a GaAs quantum well and $L \approx 50$ nm for a ZnSe quantum well, both at an electric field strength of $E = 20$ kV/cm. At the very least, one must use well widths of $L_{min} \approx 35$ nm in ZnSe and $L_{min} \approx 114$ nm in GaAs to accommodate the critical dipole moment where it is assumed that the dipole moment can achieve 80 % of the total width. Alternatively, one can use a multi-well setup with the appropriate inter-well spacing.

Using the values from Tab. 7.1 and $d = 13.3 a_{Be}^*$, the solid exciton phase spans the density interval $1.3 \times 10^9 \text{ cm}^{-2} \dots 3.6 \times 10^9 \text{ cm}^{-2}$ in a GaAs QW and $8.2 \times 10^9 \text{ cm}^{-2} \dots 3.8 \times 10^{10} \text{ cm}^{-2}$ in a ZnSe QW. The maximum temperature where the crystal can exist is around $T = 0.15$ K (GaAs) and $T = 0.78$ K (ZnSe). This makes ZnSe the more favorable material. It has been suggested to employ Bragg scattering methods [51] for an experimental observation of the crystal phase.

In conclusion, the results emphasize the role of the coupling parameter for phase transitions. For quantum phase transitions, in particular, the scaling of the coupling parameter with density is important. The existence of two transitions here can be linked to the positive scaling at low densities and the negative scaling at high-densities. The coupling can be made sufficiently strong in intermediate densities enabling the system to crystallize. For systems of indirect excitons, the peculiar effective interaction potential V_{XX} – a dipole-like interaction at low densities and a Coulomb-like interaction at high densities – triggers this behavior. However, a crystal phase bounded by two quantum phase transitions must not be restricted to excitonic matter. Any other potential which shares the outlined essential features can be expected to exhibit similar behavior.

Appendices

Generic Reduced Units

Numerical simulations almost always work on with set of units which circumvent the need to calculate energy terms with explicitly defined particle properties. Deriving such units is done by taking universalities of the Hamiltonian into account. This reduces the number of input different input parameters and identifies the actual free parameters needed to specify the system. For example, the Hamiltonian may only depend on the ratio of mass and charge of a particle. Thus, only this ratio is needed as input parameter but not mass and charge separately. Typically, this has the additional benefit to normalize variable values (i.e. small values, e.g., 1...100).

How does one derive an appropriate set of reduced units? It turns out that in almost all cases, one can follow a quite general procedure. Consider the Hamiltonian

$$\hat{H} = \hat{T} + \hat{V} + \hat{W} , \quad (\text{A.1})$$

where the *kinetic energy* \hat{T} , *external potential energy* \hat{V} and *pair-interaction energy* \hat{W} are defined as

$$\hat{T} = \sum_{i=1}^N \left[-\lambda \nabla_{\mathbf{r}_i}^2 \right] , \quad \hat{V} = \sum_{i=1}^N v(\mathbf{r}_i) , \quad \hat{W} = \sum_{i<j}^N w(|\mathbf{r}_i - \mathbf{r}_j|) , \quad (\text{A.2})$$

where $\lambda = \hbar^2/(2m)$ is the quantumness and \mathbf{r}_i denotes the position of the i^{th} particle of a total of N .

Now, one chooses a length scale ξ in which all distances shall be expressed. With the transformation

$$\mathbf{r} \rightarrow \xi \mathbf{r}' , \quad E \rightarrow \frac{2\lambda}{\xi^2} E' \equiv \eta E' , \quad (\text{A.3})$$

one obtains the following general expression for the reduced Hamiltonian:

$$\hat{H}' = \sum_{i=1}^N \left[-\frac{1}{2} \nabla_{\mathbf{r}'_i}^2 + \frac{v(\xi \mathbf{r}'_i)}{\eta} \right] + \sum_{i<j}^N \frac{w(\xi \mathbf{r}'_{ij})}{\eta}. \quad (\text{A.4})$$

While this general procedure does not specify what length scale ξ is exactly, any choice simultaneously determines the unit of energy η according to Eq. (A.3).

There are several options how to chose a specific length scale. The natural choice is the length scale imposed by the interaction. For the Coulomb pair potential

$$w_C(r) = \frac{e^2}{\epsilon} \frac{1}{r}, \quad (\text{A.5})$$

it is given by *effective atomic Bohr radius* a_B yielding the transformation

$$a_B = \frac{\hbar^2 \epsilon}{mq^2} = 2\lambda \frac{\epsilon}{e^2}, \quad \text{Ha} = \frac{2\lambda}{a_B^2} = \frac{e^2}{\epsilon a_B}, \quad (\text{A.6})$$

which defines the *effective Hartree energy* Ha from the electron charge e the effective mass m and the material dielectric constant ϵ . Without external confinement, the Hamiltonian in effective atomic units then reads

$$\hat{H}' = \sum_{i=1}^N \left[-\frac{1}{2} \nabla_{\mathbf{r}'_i}^2 \right] + \sum_{i<j}^N \frac{1}{r'_{ij}}. \quad (\text{A.7})$$

Similarly, for the harmonic potential

$$v_{\text{harm}}(\mathbf{r}) = \frac{1}{2} m\omega^2 \mathbf{r}^2, \quad (\text{A.8})$$

it is given by *harmonic oscillator length* l_0 yielding the transformation

$$l_0 = \sqrt{\frac{\hbar}{m\omega}}, \quad E_0 = \frac{2\lambda}{l_0^2} = \hbar\omega, \quad (\text{A.9})$$

where ω denotes the trapping frequency. The ideal Hamiltonian in harmonic oscillator units reads

$$\hat{H}' = \sum_{i=1}^N \left[-\frac{1}{2} \nabla_{\mathbf{r}'_i}^2 + \frac{1}{2} \mathbf{r}'_i{}^2 \right]. \quad (\text{A.10})$$

If the Hamiltonian in question implies more than one natural length scale, one can chose either for ξ and has each other defined by a *coupling parameter* ν .

For example, a trapped system of Coulomb interacting systems reads in effective atomic units

$$\hat{H}' = \sum_{i=1}^N \left[-\frac{1}{2} \nabla_{\mathbf{r}'_i}^2 + \frac{1}{2\nu^4} \mathbf{r}'_i{}^2 \right] + \sum_{i<j}^N \frac{1}{r'_{ij}}, \quad (\text{A.11})$$

and in harmonic oscillator units

$$\hat{H}' = \sum_{i=1}^N \left[-\frac{1}{2} \nabla_{\mathbf{r}'_i}^2 + \frac{1}{2} \mathbf{r}'_i{}^2 \right] + \sum_{i<j}^N \frac{\nu}{r'_{ij}}, \quad (\text{A.12})$$

where the coupling parameter ν is defined as $\nu = l_0/a_B$.

Coupling parameters also appear if one chooses an externally imposed length scale for ξ . The prime example occurs in numerical simulations of macroscopic systems which are considered at a specific density n . The latter defines a *mean inter-particle spacing* $\bar{r} \propto n^{-d}$, where d is the dimensionality of the system. The *Brueckner parameter* $r_s = \bar{r}/a_B$, for example, appears in systems with Coulomb interaction [cf. Eq. (7.3)].

Dielectric Response and Susceptibility of the 2D Coulomb Gas

In electrostatics, the dielectric function $\epsilon(k)$ is related to the charge density distribution. Here, one can define $\epsilon(k)$ in the same vein as [80]

$$\frac{1}{\epsilon(k)} = 1 - \frac{2\pi}{k^2} \frac{1}{T} \langle n(\mathbf{k})n(-\mathbf{k}) \rangle, \quad (\text{B.1})$$

where $n(\mathbf{k})$ is the Fourier transform of the vortex density $n(\mathbf{r})$,

$$n(\mathbf{r}) = \frac{1}{L^2} \sum_{i=1}^N q_i f_{r_c}(\mathbf{r} - \mathbf{r}_i), \quad \lim_{r_c \rightarrow 0} f_{r_c}(\mathbf{r}) = \delta(\mathbf{r}). \quad (\text{B.2})$$

The unknown nature of the vortex interaction within the core radius r_c (or at large k) is reflected in the modified distribution function f_{r_c} . f_{r_c} replaces the Dirac- δ function in the Poisson equation defining the Coulomb interaction

$$\nabla^2 V_0(\mathbf{r}) = -2\pi f_{r_c}(\mathbf{r}). \quad (\text{B.3})$$

However, this poses a minor problem to a theory for phase transitions, as critical phenomena manifest themselves in the change of long-range correlations. The potential converges to the usual $V_0(r) \propto \ln(r)$ result at large distances. For small k , a Fourier transform of (B.3) yields $V_0(k) = 2\pi/k^2$.

The dielectric function modifies the Fourier transform of the bare Coulomb interaction $V_0(k) = 2\pi/k^2$ in the following way

$$V(k) = \frac{V_0(k)}{\epsilon(k)} = \frac{2\pi}{k^2 \epsilon(k)}. \quad (\text{B.4})$$

On the insulating, low-temperature side of the KT transition, there are no free vortices so the leading contribution to $\epsilon(k)$ for small k stems from polarization of vortex pairs. In this case, the impact of the dielectric reduces to a constant ϵ_0 , i.e. the interaction (B.4) becomes

$$V(k) \xrightarrow{k \rightarrow 0} \frac{1}{\epsilon_0} \frac{2\pi}{k^2}, \quad \epsilon_0 \equiv \lim_{k \rightarrow 0} \epsilon(k). \quad (\text{B.5})$$

On the conducting, high-temperature side, the interaction is also screened by free vortices. In the small k limit, the interaction reads

$$V(k) \xrightarrow{k \rightarrow 0} \frac{1}{\epsilon_p} \frac{1}{k^2 + \lambda^{-2}}, \quad (\text{B.6})$$

where λ is the screening length and ϵ_p is a constant describing the polarization. The low-temperature result is recovered if assuming an infinite screening length. With the definition (B.4), it follows that

$$\frac{1}{\epsilon(k)} = \frac{1}{2\pi\epsilon_p} \frac{k^2}{k^2 + \lambda^{-2}} \xrightarrow{k \rightarrow 0} \begin{cases} \epsilon_0^{-1}, & \text{for } T < T_{\text{cr}}, \\ 0, & \text{for } T > T_{\text{cr}}. \end{cases} \quad (\text{B.7})$$

At the critical point, there is a discontinuous jump from a finite $\epsilon_{\text{cr}}^{-1} \equiv \epsilon_0^{-1}(T_{\text{cr}})$ to zero. Or in other words, the vortex unbinding occurs where the dielectric constant diverges.

Since $1/\epsilon(k)$ is finite the limit $k \rightarrow 0$, the correlation term in the definition (B.1) is also and the following identity holds

$$\lim_{k \rightarrow 0} \frac{1}{k^2} \langle n(k)n(-k) \rangle = \frac{1}{2} \left. \frac{\partial^2}{\partial k^2} \langle n(k)n(-k) \rangle \right|_{k=0}. \quad (\text{B.8})$$

Thus, a Fourier transform and some algebra then yields

$$\frac{1}{\epsilon_0} = 1 + \frac{\pi^2}{T} \int_0^\infty dr r^3 \langle n(r)n(0) \rangle, \quad (\text{B.9})$$

which links the dielectric constant to the vortex density correlation. In intuitive picture of the KT theory, the low-temperature phase consists of vortex dipoles. When assuming independent vortex dipoles, equation (B.9) can be physically interpreted by defining a susceptibility χ_0 as

$$\chi_0 = \frac{1}{L^2} \int d^2r \alpha(r)n_d(r) = -\frac{\pi}{2T} \int_0^\infty dr r^3 \langle n(r)n(0) \rangle, \quad (\text{B.10})$$

where $\alpha(r) = r^2/(2T)$ is the polarizability of a single vortex dipole [80] with separation r and where $n_d(r)$ is the corresponding vortex dipole density. It is

defined as

$$n_d(r) = -\frac{1}{2} \int d^2r' d^2r'' \langle n_+(\mathbf{r}') n_-(\mathbf{r}'') \rangle \delta((\mathbf{r}' - \mathbf{r}'') - \mathbf{r}) \quad (\text{B.11})$$

$$= -\frac{L^2}{2} \langle n(r) n(0) \rangle, \quad (\text{B.12})$$

where the index + (−) denotes the density of vortices with a positive (negative) vorticity (cf. Eq. (B.2)). With Eq. (B.10), the dielectric constant can be written as

$$\frac{1}{\epsilon_0} = 1 - 2\pi\chi_0. \quad (\text{B.13})$$

In electrostatics, the usual electric susceptibility χ is given by $\epsilon_0 = 1 + 2\pi\chi$ and hence

$$\chi = \frac{\chi_0}{1 - 2\pi\chi_0}. \quad (\text{B.14})$$

With the previously derived condition (B.7) for the critical point, one identifies $\chi_0 < \frac{1}{2\pi}$ for $T < T_{\text{cr}}$ and $\chi_0 = \frac{1}{2\pi}$ for $T > T_{\text{cr}}$. In latter case, the susceptibility χ diverges. The essential point of the above interpretation of (B.9) is that one may understand ϵ_0 in the low-temperature phase as being caused by vortex dipoles of all length scales [80].

Notes on the Pair Density Matrix

C.1 Inter-Action Derivatives With respect to β and λ

Consider the following definitions:

$$\tilde{\rho} = \tilde{\rho} \frac{d}{d\beta} \ln \tilde{\rho} \equiv -\tilde{\rho} \tilde{u} \qquad v^\beta(r, r'; \beta) \equiv \beta \tilde{u}(r, r'; \beta) \quad (\text{C.1})$$

$$\tilde{\rho}^* = \tilde{\rho} \frac{d}{d\lambda} \ln \tilde{\rho} \equiv -\tilde{\rho} \tilde{u}^* \qquad v^\lambda(r, r'; \beta) \equiv \lambda \tilde{u}^*(r, r'; \beta) \quad (\text{C.2})$$

All following relations can be derived by taking the derivative with respect to β from above equations. From Eq. (4.26):

$$v_l^{\beta, \text{semi}}(r, r'; \beta) = \frac{d-1}{2} + \mathcal{J}_l \left(\frac{rr'}{2\lambda\beta} \right) + \frac{\beta}{r-r'} \int_r^{r'} dr'' W(r''), \quad (\text{C.3})$$

$$v_l^{\lambda, \text{semi}}(r, r'; \beta) = \frac{d-1}{2} + \mathcal{J}_l \left(\frac{rr'}{2\lambda\beta} \right), \quad (\text{C.4})$$

$$\frac{d-1}{2} + \mathcal{J}_l(x) = x \frac{d}{dx} \ln \mathcal{I}_l(x) = \frac{d-1}{2} + \begin{cases} 0, & \text{1D} \\ l + x \left[\frac{\mathcal{I}_{l+1}(x)}{\mathcal{I}_l(x)} - 1 \right], & \text{else} \end{cases}, \quad (\text{C.5})$$

from Eq. (4.27), for either $v_l = v_l^\beta$ or $v_l = v_l^\lambda$:

$$v_l(r, r'; 2\beta) = \frac{1}{2} + \frac{1}{\sqrt{\pi}} \int_{-\frac{q}{\sigma}}^{\infty} dx e^{-x^2} \frac{\tilde{\rho}_l(r, q + \sigma x; \beta) \tilde{\rho}_l(q + \sigma x, r'; \beta)}{\tilde{\rho}_l(r, r'; 2\beta)} \times \left[v_l(r, q + \sigma x; \beta) + v_l(q + \sigma x, r'; \beta) - x^2 \right], \quad (\text{C.6})$$

and from Eq. (5.12), for either $V = \beta\dot{U}$ or $V = \lambda U^*$:

$$-V(\mathbf{r}, \mathbf{r}'; \beta) = \frac{d-1}{2} + \frac{rr'}{2\lambda\beta}(\cos\theta - 1) - \frac{\sum_{l=0}^{\infty} c_l \tilde{\rho}_l(r, r'; \beta) v_l(r, r'; \beta) F_l(\cos\theta)}{\sum_{l=0}^{\infty} c_l \tilde{\rho}_l(r, r'; \beta) F_l(\cos\theta)}, \quad (\text{C.7})$$

C.2 Sum of States for the Coulomb Potential

The density matrix for a particle in the Coulomb potential may be derived from an explicit sum over energy eigenfunctions since closed forms for both bound states and continuum states exist [97]. These read:

$$R_{nl}^{\text{bound}}(r) = C_{nl} e^{-\frac{\epsilon_n r}{2}} r^l L_{n-l-1}^{2l+1+2\delta}(\epsilon_n r), \quad (\text{C.8a})$$

$$R_{nl}^{\text{cont}}(k, r) = \sqrt{\frac{2}{\pi}} r^{-\delta-1} F_{l+\delta}\left(\frac{Z}{2k}, kr\right), \quad (\text{C.8b})$$

with the dimensional reduction $2\delta = d - 3$ and the effective charge number $Z = Z_1 Z_2 / \lambda$. For the bound-state wave functions, the L_n^a denote the *associated Laguerre polynomials* [93, Ch. 22] and the energy eigenvalues, E_n , and normalization constants, C_{nl} , read

$$E_n = -\frac{\lambda}{4} \epsilon_n^2 = -\frac{\lambda}{4} \left(\frac{|Z|}{n + \delta} \right)^2, \quad (\text{C.9})$$

$$C_{nl} = \frac{\epsilon_n^{l+\frac{d}{2}}}{\sqrt{2n+2\delta}} \sqrt{\frac{(n-l-1)!}{(n+l+2\delta)!}}, \quad (\text{C.10})$$

For the continuum wave functions, the $F_L(\eta, \rho)$ are the usual *regular Coulomb wave functions* [93, Ch. 14] defined as

$$F_L(\eta, \rho) = C_L(\eta) \rho^{L+1} e^{-i\rho} {}_1F_1(L+1-i\eta; 2L+2; 2i\rho), \quad (\text{C.11})$$

$$C_L(\eta) = 2^L e^{-\pi\eta/2} \frac{|\Gamma(L+1+i\eta)|}{\Gamma(2L+2)}, \quad (\text{C.12})$$

where ${}_1F_1(a; b; z)$ is the *Kummer's function* or *confluent hypergeometric function* [93, Ch. 13] and $\Gamma(x)$ the *Gamma function* [93, Ch. 6]. The GSL library provides routines for the direct computation of the regular Coulomb wave functions (C.11).

Both, bound state and continuum state wave functions are real-valued. Thus, the radial density matrix in terms of these eigenfunctions is

$$\rho_l(r, r'; \beta) = (rr')^{\delta+1} \left[\sum_{n=l+1}^{\infty} e^{-\beta E_n} R_{nl}^{\text{bound}}(r) R_{nl}^{\text{bound}}(r') + \int_0^{\infty} dk e^{-\beta \lambda k^2} R_l^{\text{cont}}(k, r) R_l^{\text{cont}}(k, r') \right], \quad (\text{C.13})$$

which gives after insertion of the expressions (C.8):

$$\rho_l^{\text{bound}}(r, r'; \beta) = (rr')^{l+\delta+1} \sum_{n=l+1}^{\infty} C_{nl}^2 \exp \left[\frac{\lambda\beta}{4} \epsilon_n - \frac{r+r'}{2} \epsilon_n \right] \times L_{n-l-1}^{2l+1+2\delta}(\epsilon_n r) L_{n-l-1}^{2l+1+2\delta}(\epsilon_n r'), \quad (\text{C.14})$$

$$\rho_l^{\text{cont}}(r, r'; \beta) = \frac{2}{\pi} \int_0^{\infty} dk e^{-\lambda\beta k^2} F_{l+\delta} \left(\frac{Z}{2k}, kr \right) F_{l+\delta} \left(\frac{Z}{2k}, kr' \right). \quad (\text{C.15})$$

The sum and the integral must be evaluated numerically with an appropriate method [96].

The analytical expressions for the density matrix of the Coulomb potential can be used to test the Matrix Squaring method. When using the pair density matrix with Path-Integral Monte-Carlo simulations, one should rewrite the partial-wave expansion to the faster converging power-series expansion Eq. (5.14). A special property of the Coulomb potential is that the pair density matrix depends only on two spatial variables, e.g. q and s [Eq. (5.13)] [97]. This simplifies the power series expansion significantly as one has $u_{kj} = 0$ for $j > 0$.

Notes on Monte-Carlo Sampling

D.1 Asymmetric Kinetic Energy Links

The most fundamental type of sampling in path-integral Monte-Carlo is the movement of a bead on an arbitrary slice. The free kinetic energy its neighboring beads can be treated exactly, even if the connecting links are asymmetric.

Suppose we wish to sample a new bead \mathbf{r}' on a slice spaced by $P_1\tau$ and $P_2\tau$ from its neighbors. The slice indices of the latter we set to 0 and $P = P_1 + P_2$, respectively. The sampling distribution then reads

$$T(s, s') = \frac{\rho_0(\mathbf{r}_0, \mathbf{r}'; P_1\tau) \rho_0(\mathbf{r}'; \mathbf{r}_P, P_2\tau)}{\rho_0(\mathbf{r}_0, \mathbf{r}_P; P\tau)} \quad (\text{D.1})$$

$$= \left(\frac{1}{2\pi\nu\tau} \right)^{d/2} e^{-\frac{(\mathbf{r}_0 - \mathbf{r}')^2}{2P_1\tau}} e^{-\frac{(\mathbf{r}' - \mathbf{r}_P)^2}{2P_2\tau}} e^{\frac{(\mathbf{r}_0 - \mathbf{r}_P)^2}{2P\tau}} \quad (\text{D.2})$$

$$= \left(\frac{1}{2\pi\nu\tau} \right)^{d/2} e^{-\frac{(\mathbf{r}_m - \mathbf{r}')^2}{2\nu\tau}}, \quad (\text{D.3})$$

with the reduced temperature $\nu\tau = P_1P_2/P\tau$ and the weighted midpoint $\mathbf{r}_m = P_2\mathbf{r}_0 + P_1\mathbf{r}_P/P$. Since Eq. (D.3) is Gaussian, the coordinates of the new bead can be computed as

$$\mathbf{r}' = \mathbf{r}_m + \sqrt{\nu\tau} \mathbf{n}, \quad (\text{D.4})$$

where \mathbf{n} is a random vector sampled from the normal distribution $\mathcal{G}_d(0, 1)$.

D.2 Multilevel Sampling

Suppose that one wishes to sample a new configuration not at once but in a sequence of steps which can be interrupted and rejected at any point. Let the full configuration s be partitioned into $l + 1$ groups (levels) of coordinates $s = \{\tilde{s}_0, \tilde{s}_1, \dots, \tilde{s}_l\}$, where \tilde{s}_0 are the coordinates left unchanged, \tilde{s}_1 the coordinates sampled in the first step and so on.

For each level one devises a *level sampling distribution* $T_k(s_k, s'_k)$ and a *level acceptance probability* $A_k(s_k, s'_k)$ which both shall only depend on the coordinates $s_k \equiv \{\tilde{s}_0, \tilde{s}_1, \dots, \tilde{s}_k\}$ sampled up to this point. Any choices are valid as long as the total transition probability

$$P(s, s') = \prod_{k=1}^l T_k(s_k, s'_k) A_k(s_k, s'_k), \quad (\text{D.5})$$

satisfies detailed balance (5.24). For the *level distribution of states* $\pi_k(s)$ any approximation is valid, except on the last level, on which

$$\pi_l(s) = \pi(s), \quad (\text{D.6})$$

must obviously hold. Note that $\pi_k(s)$ may depend only on already sampled coordinates, i.e. $\pi_k(s) = \pi_k(s_k)$.

Similar to Eq. (5.26), the acceptance probability can be fixed to

$$A_k(s_k, s'_k) = \min \left[1, \frac{T_k(s'_k, s_k) \pi_k(s'_k) \pi_{k-1}(s_{k-1})}{T_k(s_k, s'_k) \pi_k(s_k) \pi_{k-1}(s'_{k-1})} \right] \quad (\text{D.7})$$

which ensures that $T_k(s_k, s'_k) A_k(s_k, s'_k)$ satisfies detailed balance on each level, i.e.

$$\frac{\pi_k(s_k)}{\pi_{k-1}(s_{k-1})} T_k(s_k, s'_k) A_k(s_k, s'_k) = \frac{\pi_k(s'_k)}{\pi_{k-1}(s'_{k-1})} T_k(s'_k, s_k) A_k(s'_k, s_k). \quad (\text{D.8})$$

Due to $s_0 = s'_0$, the distribution of states on the lowest level π_0 cancels in both equations above and, thus, can be set to unity. Taking $\prod_{k=1}^l \dots$ on both sides of Eq. (D.8) proves that the whole attempt [Eq. (D.5)] satisfies the detailed balance for any level sampling distribution $T_k(s_k, s'_k)$ one desires.

Since the distribution of states on the k^{th} level should not depend on any coordinates of higher levels, the optimal choice of $\pi_k(s_k)$ is given if all these higher level coordinates are integrated out, i.e.

$$\pi_k^{\text{opt}}(s_k) = \int d\tilde{s}_{k+1} \dots d\tilde{s}_l \pi(s). \quad (\text{D.9})$$

The optimal transition probability is given by the heat bath rule

$$T_k^{\text{opt}}(s_k, s'_k) = \frac{\pi_k^{\text{opt}}(s_k)}{\int \mathrm{d}\tilde{s}_k \pi_k^{\text{opt}}(s_k)} = \frac{\pi_k^{\text{opt}}(s_k)}{\pi_{k-1}^{\text{opt}}(s_{k-1})}, \quad (\text{D.10})$$

where the r.h.s holds if and only if $\pi_k^{\text{opt}}(s_k)$ is defined as in Eq. (D.9).

Bibliography

- [1] S. N. Bose, *Z. Phys.* **26**, 178 (1924).
- [2] A. Einstein, “Quantentheorie des Einatomigen Idealen Gases,” *Sitzber. Kgl. Preuss. Akad. Wiss.*, 261(1924); A. Einstein, “Zweite Abhandlung,” *Sitzber. Kgl. Preuss. Akad. Wiss.*, 3(1925).
- [3] I. Bloch, T. W. Hansch, and T. Esslinger, “Measurement of the spatial coherence of a trapped bose gas at the phase transition,” *Nature* **403**, 166–170 (2000).
- [4] D. Snoke, “Condensed-matter physics: Coherent questions,” *Nature* **443**, 403–404 (2006).
- [5] O. Penrose and L. Onsager, “Bose-Einstein condensation and liquid helium,” *Phys. Rev.* **104**, 576 (1956).
- [6] C. N. Yang, “Concept of Off-Diagonal Long-Range order and the quantum phases of liquid he and of superconductors,” *Rev. Mod. Phys.* **34**, 694 (1962).
- [7] For a review, see, e.g., A. J. Leggett, “The ubiquity of superconductivity,” *Ann. Rev. Cond. Mat. Phys.* **2**, 11–30 (2011).
- [8] For a review, see, e.g., A. J. Leggett, “Superfluidity,” *Rev. Mod. Phys.* **71**, S318 (1999).
- [9] P. Kapitza, “Viscosity of liquid helium below the λ -point,” *Nature* **141**, 74 (1938).
- [10] J. F. Allen and A. D. Misener, “Flow of liquid helium II,” *Nature* **141**, 75 (1938).
- [11] N. N. Bogoliubov, *Phys. Abh. Sow.* **6**, 113, 229 (1962).

- [12] M. H. Anderson, J. R. Ensher, M. R. Matthews, C. E. Wieman, and E. A. Cornell, "Observation of Bose-Einstein condensation in a dilute atomic vapor," *Science* **269**, 198–201 (1995).
- [13] K. B. Davis, *et al.*, "Bose-Einstein condensation in a gas of sodium atoms," *Phys. Rev. Lett.* **75**, 3969 (1995).
- [14] C. C. Bradley, C. A. Sackett, and R. G. Hulet, "Bose-Einstein condensation of lithium: Observation of limited condensate number," *Phys. Rev. Lett.* **78**, 985 (1997).
- [15] For an overview, see A. J. Leggett, "Bose-Einstein condensation in the alkali gases: Some fundamental concepts," *Rev. Mod. Phys.* **73**, 307 (2001); A. J. Leggett, "Erratum," *Rev. Mod. Phys.* **75**, 1083 (2003).
- [16] A. Griesmaier, J. Werner, S. Hensler, J. Stuhler, and T. Pfau, "Bose-Einstein condensation of chromium," *Phys. Rev. Lett.* **94**, 160401 (2005); J. Stuhler, *et al.*, "Observation of Dipole-Dipole interaction in a degenerate quantum gas," *Phys. Rev. Lett.* **95**, 150406 (2005).
- [17] For a review, see T. Lahaye, C. Menotti, L. Santos, M. Lewenstein, and T. Pfau, "The physics of dipolar bosonic quantum gases," *Rep. Prog. Phys.* **72**, 126401 (2009).
- [18] H. Miesner, *et al.*, "Observation of metastable states in spinor Bose-Einstein condensates," *Phys. Rev. Lett.* **82**, 2228 (1999).
- [19] F. P. D. Santos, *et al.*, "Bose-Einstein condensation of metastable helium," *Phys. Rev. Lett.* **86**, 3459 (2001).
- [20] M. Greiner, O. Mandel, T. Esslinger, T. W. Hansch, and I. Bloch, "Quantum phase transition from a superfluid to a mott insulator in a gas of ultracold atoms," *Nature* **415**, 39–44 (2002).
- [21] D. L. Kovrizhin, G. V. Pai, and S. Sinha, "Density wave and supersolid phases of correlated bosons in an optical lattice," *Eur. Phys. Lett.* **72**, 162–168 (2005).
- [22] K. Góral, L. Santos, and M. Lewenstein, "Quantum phases of dipolar bosons in optical lattices," *Phys. Rev. Lett.* **88**, 170406 (2002).
- [23] S. L. Cornish, N. R. Claussen, J. L. Roberts, E. A. Cornell, and C. E. Wieman, "Stable ^{85}Rb Bose-Einstein condensates with widely tunable interactions," *Phys. Rev. Lett.* **85**, 1795 (2000).
- [24] C. Ruegg, *et al.*, "Bose-Einstein condensation of the triplet states in the magnetic insulator TlCuCl_3 ," *Nature* **423**, 62–65 (2003).

-
- [25] For a theoretical review, see F. Dalfovo, S. Giorgini, L. P. Pitaevskii, and S. Stringari, “Theory of Bose-Einstein condensation in trapped gases,” *Rev. Mod. Phys.* **71**, 463 (1999).
- [26] For an introduction, see e. g., C. F. Klingshirn, *Semiconductor Optics*, 2nd ed. (Springer-Verlag GmbH, 2005) ISBN 3540213287.
- [27] L. V. Butov, C. W. Lai, A. L. Ivanov, A. C. Gossard, and D. S. Chemla, “Towards Bose-Einstein condensation of excitons in potential traps,” *Nature* **417**, 47–52 (2002).
- [28] D. Snoke, “Spontaneous bose coherence of excitons and polaritons,” *Science* **298**, 1368–1372 (2002).
- [29] D. W. Snoke, “When should we say we have observed bose condensation of excitons?,” *phys. stat. sol. (b)* **238**, 389–396 (2003).
- [30] A. H. MacDonald and E. H. Rezayi, “Fractional quantum hall effect in a two-dimensional electron-hole fluid,” *Phys. Rev. B* **42**, 3224 (1990).
- [31] L. Tiemann, W. Dietsche, M. Hauser, and K. von Klitzing, “Critical tunneling currents in the regime of bilayer excitons,” *New J. Phys.* **10**, 045018 (2008).
- [32] J. P. Eisenstein and A. H. MacDonald, “Bose-Einstein condensation of excitons in bilayer electron systems,” *Nature* **432**, 691–694 (2004).
- [33] V. B. Timofeev and A. V. Gorbunov, “Collective state of the bose gas of interacting dipolar excitons,” *J. Appl. Phys.* **101**, 081708 (2007).
- [34] H. Deng, G. Weihs, C. Santori, J. Bloch, and Y. Yamamoto, “Condensation of semiconductor microcavity exciton polaritons,” *Science* **298**, 199–202 (2002).
- [35] J. Kasprzak, *et al.*, “Bose-Einstein condensation of exciton polaritons,” *Nature* **443**, 409–414 (2006).
- [36] R. Balili, V. Hartwell, D. Snoke, L. Pfeiffer, and K. West, “Bose-Einstein condensation of microcavity polaritons in a trap,” *Science* **316**, 1007–1010 (2007).
- [37] S. O. Demokritov, *et al.*, “Bose-Einstein condensation of quasi-equilibrium magnons at room temperature under pumping,” *Nature* **443**, 430–433 (2006).
- [38] O. V. Misochko, M. Hase, K. Ishioka, and M. Kitajima, “Transient Bose-Einstein condensation of phonons,” *Phys. Lett. A* **321**, 381–387 (2004).

- [39] J. Klaers, J. Schmitt, F. Vewinger, and M. Weitz, “Bose-Einstein condensation of photons in an optical microcavity,” *Nature* **468**, 545–548 (2010).
- [40] R. Onofrio, *et al.*, “Observation of superfluid flow in a Bose-Einstein condensed gas,” *Phys. Rev. Lett.* **85**, 2228 (2000).
- [41] C. Raman, *et al.*, “Evidence for a critical velocity in a Bose-Einstein condensed gas,” *Phys. Rev. Lett.* **83**, 2502 (1999).
- [42] A. Amo, *et al.*, “Superfluidity of polaritons in semiconductor microcavities,” *Nat. Phys.* **5**, 805–810 (2009).
- [43] A. Amo, *et al.*, “Collective fluid dynamics of a polariton condensate in a semiconductor microcavity,” *Nature* **457**, 291–295 (2009).
- [44] M. H. Szymańska, J. Keeling, and P. B. Littlewood, “Nonequilibrium quantum condensation in an incoherently pumped dissipative system,” *Phys. Rev. Lett.* **96**, 230602 (2006).
- [45] H. Fröhlich, “Bose condensation of strongly excited longitudinal electric modes,” *Phys. Lett. A* **26**, 402–403 (1968).
- [46] D. W. Snoke and J. P. Wolfe, “Population dynamics of a bose gas near saturation,” *Phys. Rev. B* **39**, 4030 (1989).
- [47] H. T. C. Stoof, “Nucleation of Bose-Einstein condensation,” *Phys. Rev. A* **45**, 8398 (1992).
- [48] L. Butov, “Exciton condensation in coupled quantum wells,” *Solid State Commun.* **127**, 89–98 (2003).
- [49] Y. E. Lozovik and V. I. Yudson, *Zh. Éksp. i Teor. Fiz.* **71**, 738–753 (1976) [Y. E. Lozovik and V. I. Yudson, “New mechanism for superconductivity: pairing between spatially separated electrons and holes,” *Sov. Phys. JETP* **44**, 389–397 (1976)].
- [50] P. Ludwig, A. V. Filinov, M. Bonitz, and H. Stolz, “Quantum stark confined strongly correlated indirect excitons in quantum wells,” *phys. stat. sol. (b)* **243**, 2363–2366 (2006).
- [51] K. Sperlich, *et al.*, “Electric field-induced exciton localization in quantum wells,” *phys. stat. sol. (c)* **6**, 551–555 (2009).
- [52] D. Snoke, S. Denev, Y. Liu, L. Pfeiffer, and K. West, “Long-range transport in excitonic dark states in coupled quantum wells,” *Nature* **418**, 754–757 (2002).

- [53] N. D. Mermin and H. Wagner, “Absence of ferromagnetism or antiferromagnetism in one- or Two-Dimensional isotropic heisenberg models,” *Phys. Rev. Lett.* **17**, 1133 (1966); N. D. Mermin and H. Wagner, “Absence of ferromagnetism or antiferromagnetism in one- or Two-Dimensional isotropic heisenberg models,” *Phys. Rev. Lett.* **17**, 1307 (1966).
- [54] For a review, see A. Gelfert and W. Nolting, “The absence of finite-temperature phase transitions in low-dimensional many-body models: a survey and new results,” *J. Phys.: Condens. Matter* **13**, R505 (2001).
- [55] V. L. Berezinskii, *Zh. Éksp. i Teor. Fiz.* **61**, 1144 (1971) [V. L. Berezinskii, *Sov. Phys. JETP* **34**, 610 (1972)].
- [56] J. M. Kosterlitz and D. J. Thouless, “Ordering, metastability and phase transitions in two-dimensional systems,” *J. Phys. C* **6**, 1181 (1973); J. Kosterlitz and D. Thouless, *Prog. Low. Temp Phys.* **7B**, 371 (1978).
- [57] D. J. Bishop and J. D. Reppy, “Study of the superfluid transition in Two-Dimensional ^4He films,” *Phys. Rev. Lett.* **40**, 1727 (1978).
- [58] *Introduction to Complex Plasmas*, 1st ed., edited by M. Bonitz, N. Horing, and P. Ludwig (Springer, Berlin, 2010) ISBN 9783642105913.
- [59] R. K. Kalia and P. Vashishta, “Interfacial colloidal crystals and melting transition,” *J. Phys. C* **14**, L643 (1981).
- [60] G. E. Astrakharchik, J. Boronat, I. L. Kurbakov, and Y. E. Lozovik, “Quantum phase transition in a Two-Dimensional system of dipoles,” *Phys. Rev. Lett.* **98**, 060405 (2007).
- [61] H. P. Büchler, *et al.*, “Strongly correlated 2D quantum phases with cold polar molecules: Controlling the shape of the interaction potential,” *Phys. Rev. Lett.* **98**, 060404 (2007).
- [62] C. Mora, O. Parcollet, and X. Waintal, “Quantum melting of a crystal of dipolar bosons,” *Phys. Rev. B* **76**, 064511 (2007).
- [63] X. Zhu, P. B. Littlewood, M. S. Hybertsen, and T. M. Rice, “Exciton condensate in semiconductor quantum well structures,” *Phys. Rev. Lett.* **74**, 1633 (1995).
- [64] Y. E. Lozovik and O. L. Berman, “Phase transitions in a system of spatially separated electrons and holes,” *J. Exp. Theor. Phys.* **84**, 1027–1035 (1997).
- [65] Y. E. Lozovik and O. L. Berman, “Quantum crystallization of two-dimensional dipole systems,” *Phys. Solid State* **40**, 1228–1233 (1998).

- [66] A. V. Filinov, C. Riva, F. M. Peeters, Y. E. Lozovik, and M. Bonitz, “Influence of well-width fluctuations on the binding energy of excitons, charged excitons, and biexcitons in GaAs-based quantum wells,” *Phys. Rev. B* **70**, 035323 (2004).
- [67] S. Baskoutas, “Excitons and charged excitons in InAs nanorods,” *Chem. Phys. Lett.* **404**, 107–111 (2005).
- [68] S. D. Palo, F. Rapisarda, and G. Senatore, “Excitonic condensation in a symmetric Electron-Hole bilayer,” *Phys. Rev. Lett.* **88**, 206401 (2002).
- [69] A. V. Filinov, M. Bonitz, and Y. E. Lozovik, “Excitonic clusters in coupled quantum dots,” *J. Phys. A* **36**, 5899–5904 (2003).
- [70] A. Filinov, N. V. Prokof’ev, and M. Bonitz, “Berezinskii-Kosterlitz-Thouless transition in Two-Dimensional dipole systems,” *Phys. Rev. Lett.* **105**, 070401 (2010).
- [71] M. Bonitz, *et al.*, “Classical and quantum coulomb crystals,” *Phys. Plasmas* **15**, 055704 (2008).
- [72] R. P. Feynman, *Statistical Mechanics: A Set Of Lectures*, 2nd ed. (Westview Press, 1998) ISBN 0201360764.
- [73] F. Schwabl, *Statistical Mechanics*, 1st ed. (Springer, 2002) ISBN 3540431632.
- [74] H. Kleinert, *Path Integrals in Quantum Mechanics, Statistics, Polymer Physics, and Financial Markets*, 5th ed. (World Scientific Pub Co, 2009) ISBN 9789814273565.
- [75] For a review, see M. V. Berry and K. E. Mount, “Semiclassical approximations in wave mechanics,” *Rep. Prog. Phys.* **35**, 315–397 (1972).
- [76] N. N. Bogoliubov, “On some problems of the theory of superconductivity,” *Physica* **26**, S1–S16 (1960).
- [77] H. Wagner, “Long-wavelength excitations and the goldstone theorem in many-particle systems with “broken symmetries,”” *Z. Phys.* **195**, 273–299 (1966).
- [78] P. C. Hohenberg, “Existence of Long-Range order in one and two dimensions,” *Phys. Rev.* **158**, 383 (1967).
- [79] For a review, see K. J. Strandburg, “Two-dimensional melting,” *Rev. Mod. Phys.* **60**, 161 (1988).

-
- [80] P. Minnhagen, “New renormalization equations for the Kosterlitz-Thouless transition,” *Phys. Rev. B* **32**, 3088 (1985).
- [81] J. M. Thijssen and H. J. F. Knops, “Analysis of a new set of renormalization equations for the Kosterlitz-Thouless transition,” *Phys. Rev. B* **38**, 9080 (1988).
- [82] D. R. Nelson and J. M. Kosterlitz, “Universal jump in the superfluid density of Two-Dimensional superfluids,” *Phys. Rev. Lett.* **39**, 1201 (1977).
- [83] J. F. Fernández, M. F. Ferreira, and J. Stankiewicz, “Critical behavior of the two-dimensional XY model: A monte carlo simulation,” *Phys. Rev. B* **34**, 292 (1986).
- [84] B. I. Halperin and D. R. Nelson, “Theory of Two-Dimensional melting,” *Phys. Rev. Lett.* **41**, 121 (1978).
- [85] D. R. Nelson and B. I. Halperin, “Dislocation-mediated melting in two dimensions,” *Phys. Rev. B* **19**, 2457 (1979).
- [86] A. P. Young, “Melting and the vector coulomb gas in two dimensions,” *Phys. Rev. B* **19**, 1855 (1979).
- [87] R. G. Storer, “Path-Integral calculation of the Quantum-Statistical density matrix for attractive coulomb forces,” *J. Math. Phys.* **9**, 964–970 (1968).
- [88] A. D. Klemm and R. G. Storer, “The structure of quantum fluids: helium and neon,” *Aus. J. Phys.* **26**, 43 (1973).
- [89] D. M. Ceperley, “Path integrals in the theory of condensed helium,” *Rev. Mod. Phys.* **67**, 279 (1995).
- [90] See, e.g., C. Müller, *Spherical Harmonics*, 1st ed. (Springer, 1966) ISBN 3540036008.
- [91] C. W. Clenshaw, “A note on the summation of Chebyshev series,” *Math. Tab. Wash.* **9**, 118–120 (1955).
- [92] For a review, see R. Barrio, B. Melendo, and S. Serrano, “On the numerical evaluation of linear recurrences,” *J. Comp. Appl. Math.* **150**, 71–86 (2003).
- [93] I. A. Stegun and M. Abramowitz, *Handbook of Mathematical Functions with Formulas, Graphs, and Mathematical Table*, new ed. (Dover Pubn Inc, 1965) ISBN 0486612724.
- [94] V. Strassen, “Gaussian elimination is not optimal,” *Num. Math.* **13**, 354–356 (1969).

- [95] D. Coppersmith and S. Winograd, "Matrix multiplication via arithmetic progressions," *J. Symb. Comp.* **9**, 251–280 (1990).
- [96] W. H. Press, S. A. Teukolsky, W. T. Vetterling, and B. P. Flannery, *Numerical Recipes 3rd Edition: The Art of Scientific Computing*, 3rd ed. (Cambridge University Press, 2007) ISBN 0521880688.
- [97] E. L. Pollock, "Properties and computation of the coulomb pair density matrix," *Comput. Phys. Commun.* **52**, 49–60 (1988).
- [98] C. Moler and C. V. Loan, "Nineteen dubious ways to compute the exponential of a matrix, Twenty-Five years later," *SIAM Review* **45**, 3 (2003).
- [99] *Introduction to Computational Methods in Many Body Physics*, edited by M. Bonitz and D. Semkat (Rinton Press, 2006) ISBN 1589490096.
- [100] D. P. Landau and K. Binder, *A Guide to Monte Carlo Simulations in Statistical Physics*, 3rd ed. (Cambridge University Press, 2009) ISBN 0521768489.
- [101] H. F. Trotter, "On the product of semi-groups of operators," *Proc. Amer. Math. Soc.* **10**, 545–551 (1959).
- [102] J. A. Barker, "A quantum-statistical monte carlo method; path integrals with boundary conditions," *J. Chem. Phys.* **70**, 2914 (1979).
- [103] N. Metropolis, A. W. Rosenbluth, M. N. Rosenbluth, A. H. Teller, and E. Teller, "Equation of state calculations by fast computing machines," *J. Chem. Phys.* **21**, 1087 (1953).
- [104] A. J. Kinderman and J. F. Monahan, "Computer generation of random variables using the ratio of uniform deviates," *Trans. Math. Soft.* **3**, 257–260 (1977), ACM ID: 355750.
- [105] J. L. Leva, "A fast normal random number generator," *Trans. Math. Soft.* **18**, 449–453 (1992), ACM ID: 138364.
- [106] M. Boninsegni, N. Prokof'ev, and B. Svistunov, "Worm algorithm for Continuous-Space path integral Monte Carlo simulations," *Phys. Rev. Lett.* **96**, 070601–4 (2006).
- [107] M. Boninsegni, N. V. Prokof'ev, and B. V. Svistunov, "Worm algorithm and diagrammatic Monte Carlo: a new approach to continuous-space path integral Monte Carlo simulations," *Phys. Rev. E* **74**, 036701–16 (2006).
- [108] M. F. Herman, "On path integral Monte Carlo simulations," *J. Chem. Phys.* **76**, 5150 (1982).

-
- [109] E. Andronikashvili, *J. Phys. USSR* **10**, 201 (1946).
- [110] Y. Shi, “Superfluidity or supersolidity as a consequence of off-diagonal long-range order,” *Phys. Rev. B* **72**, 014533 (2005); Y. Shi, “Erratum,” *Phys. Rev. B* **74**, 029901 (2006).
- [111] E. L. Pollock and D. M. Ceperley, “Path-integral computation of superfluid densities,” *Phys. Rev. B* **36**, 8343 (1987).
- [112] A. Filinov, J. Böning, M. Bonitz, and Y. E. Lozovik, “Controlling the spatial distribution of superfluidity in radially ordered coulomb clusters,” *Phys. Rev. B* **77**, 214527–5 (2008).
- [113] M. Troyer and U. Wiese, “Computational complexity and fundamental limitations to fermionic quantum monte carlo simulations,” *Phys. Rev. Lett.* **94**, 170201 (2005).
- [114] A. Filinov, P. Ludwig, M. Bonitz, and Y. E. Lozovik, “Effective interaction potential and superfluid–solid transition of spatially indirect excitons,” *J. Phys. A* **42**, 214016 (2009).
- [115] A. Filinov, P. Ludwig, Y. E. Lozovik, M. Bonitz, and H. Stolz, “Strongly correlated indirect excitons in quantum wells in high electric fields,” *J. Phys.: Conf. Ser.* **35**, 197–208 (2006).
- [116] M. Bonitz, V. S. Filinov, V. E. Fortov, P. R. Levashov, and H. Fehske, “Crystallization in Two-Component coulomb systems,” *Phys. Rev. Lett.* **95**, 235006 (2005).
- [117] A. V. Filinov, M. Bonitz, and Y. E. Lozovik, “Wigner crystallization in mesoscopic 2D electron systems,” *Phys. Rev. Lett.* **86**, 3851 (2001).
- [118] L. V. Keldysh and Z. N. Kozlov, *Zh. Éksp. i Teor. Fiz. Pisma* **5**, 238 (1967) [L. V. Keldysh and Z. N. Kozlov, *Sov. Phys. JETP Lett.* **5**, 190 (1967)].
- [119] L. V. Keldysh, Z. N. Kozlov, and A. N. Kozlov, *Zh. Éksp. i Teor. Fiz.* **54**, 978 (1968) [L. V. Keldysh, Z. N. Kozlov, and A. N. Kozlov, *Sov. Phys. JETP* **27**, 521 (1968)].
- [120] For a review, see A. Klein and E. R. Marshalek, “Boson realizations of lie algebras with applications to nuclear physics,” *Rev. Mod. Phys.* **63**, 375 (1991).
- [121] M. Combescot and O. Betbeder-Matibet, “Interacting excitons described by an infinite series of composite-exciton operators,” *Phys. Rev. B* **78**, 125206 (2008).

- [122] M. Combescot and D. W. Snoke, “Stability of a Bose-Einstein condensate revisited for composite bosons,” *Phys. Rev. B* **78**, 144303 (2008).
- [123] B. K. Clark, M. Casula, and D. M. Ceperley, “Hexatic and mesoscopic phases in a 2D quantum coulomb system,” *Phys. Rev. Lett.* **103**, 055701 (2009).
- [124] Y. E. Lozovik and V. M. Farztdinov, “Oscillation spectra and phase diagram of two-dimensional electron crystal: ”New” (3+4)-self-consistent approximation,” *Solid State Commun.* **54**, 725–728 (1985).
- [125] P. Hartmann, *et al.*, “Crystallization dynamics of a single layer complex plasma,” *Phys. Rev. Lett.* **105**, 115004 (2010).
- [126] J. M. Kosterlitz, “The critical properties of the two-dimensional xy model,” *J. Phys. C* **7**, 1046–1060 (1974).
- [127] N. F. Mott, “The basis of the electron theory of metals, with special reference to the transition metals,” *Proc. Phys. Soc. A* **62**, 416–422 (1949).
- [128] R. Bonnett and N. F. Mott, *Metal-Insulator Transitions*, 2nd ed. (Taylor & Francis Ltd, 1990) ISBN 0850667836.
- [129] F. Gebhard, *The Mott Metal-Insulator Transition: Models and Methods*, 1st ed. (Springer, Berlin, 1997) ISBN 9783540614814.
- [130] A. Filinov, M. Bonitz, P. Ludwig, and Y. E. Lozovik, “Path integral monte carlo results for bose condensation of mesoscopic indirect excitons,” *phys. stat. sol. (c)* **3**, 2457–2460 (2006).
- [131] S. B. de-Leon and B. Laikhtman, “Mott transition, biexciton crossover, and spin ordering in the exciton gas in quantum wells,” *Phys. Rev. B* **67**, 235315 (2003).
- [132] M. Stern, V. Garmider, V. Umansky, and I. Bar-Joseph, “Mott transition of excitons in coupled quantum wells,” *Phys. Rev. Lett.* **100**, 256402 (2008); A. L. Ivanov, E. A. Muljarov, L. Mouchliadis, and R. Zimmermann, “Comment,” *Phys. Rev. Lett.* **104**, 179701 (2010); M. Stern, *et al.*, “Reply,” *Phys. Rev. Lett.* **104**, 179702 (2010).
- [133] P. Ludwig, A. Filinov, Y. E. Lozovik, H. Stolz, and M. Bonitz, “Crystallization in Mass-Asymmetric Electron-Hole bilayers,” *Contrib. to Plasma Phys.* **47**, 335–344 (2007).
- [134] D. S. Fisher and P. C. Hohenberg, “Dilute bose gas in two dimensions,” *Phys. Rev. B* **37**, 4936 (1988).

- [135] N. Prokof'ev, O. Ruebenacker, and B. Svistunov, "Critical point of a weakly interacting Two-Dimensional bose gas," *Phys. Rev. Lett.* **87**, 270402 (2001).

List of own publications

Publications in Peer Reviewed Journals and Book Chapters

- J. Böning, A. Filinov, P. Ludwig, H. Baumgartner, M. Bonitz and Yu. E. Lozovik, “Melting of Trapped Few-Particle Systems,” *Physical Review Letters* **100**, 11, 113401–4 (2008).
- A. Filinov, J. Böning, M. Bonitz and Yu. E. Lozovik, “Controlling the spatial distribution of superfluidity in radially ordered Coulomb clusters”, *Phys. Rev. B* **77**, 21, 214527–5 (2008).
- A. Filinov, J. Böning, and M. Bonitz, “Path Integral Monte Carlo Simulations of Charged Particles in Traps”, chapter in H. Fehske, R. Schneider und A. Weiße (Eds.), *Computational Many-Particle Physics*, Springer Lecture Notes in Physics, Volume 739 (Springer, 2008) ISBN 978-3-540-74685-0.
- M. Bonitz, A. Filinov, J. Böning and J. W. Dufty, “Introduction to Quantum Plasmas,” chapter in M. Bonitz, N. Horing, and P. Ludwig (Eds.), *Introduction to Complex Plasmas*, Springer Series on Atomic, Optical, and Plasma Physics, Volume 59 (Springer, 2010) ISBN 978-3-642-10591-3.
- J. Böning, A. Filinov and M. Bonitz, “Crystallization of an Exciton Superfluid,” submitted to *Phys. Rev. B*, arXiv:1101.1757 (2011).

Selected Contributions to International Conferences

- J. Böning, T. Ott and M. Bonitz, “Shortcomings of Lindemann-like melting criteria in finite systems, Poster at *DPG spring meeting*, Hannover, March 8–12, *Verhandl. DPG A* 8.2 (2010)
- H. Thomsen, J. Böning and M. Bonitz, “Melting in small size Yukawa clusters”, Poster at *DPG spring meeting*, Hannover, March 8–12, *Verhandl. DPG P* 7.3 (2010)

- J. Böning, A. Filinov, P. Ludwig and M. Bonitz, “Phase diagram of spatially indirect excitons with an effective interaction potential”, Poster at *DPG spring meeting*, Hannover, March 8–12, Verhandl. DPG A 23.24 (2010)
- J. Böning, A. Filinov, M. Bonitz and Yu. E. Lozovik, “Local superfluidity in finite Coulomb and neutral systems”, Poster at *International Workshop on Laser Physics*, Barcelona, Spain, July 13–17 (2009)
- J. Böning, A. Filinov and M. Bonitz, “Local superfluidity in finite 2D helium systems”, Poster at *DPG spring meeting*, Hamburg, March 2–6, Verhandl. DPG A 15.32 (2009)
- J. Böning, “Bose-Einstein condensation and superfluidity of charged and neutral particles”, Lecture at *Summer Institute “Complex Plasmas”*, Hoboken, NJ, July 30 – August 8 (2008)

Curriculum Vitae

Name	Jens Böning
Anschrift	Samwerstr. 5 24118 Kiel
e-Mail	jens.b20@gmail.com
Telefon	0176 61617855

Persönliche Daten

Geburtsdatum	17. März 1981
Geburtsort	Kiel
Familienstand	Ledig
Staatsangehörigkeit	Deutsch

Ausbildung

April 2007 – Heute	Dissertation zum Thema „Superfluidity and Correlations in Systems of Indirect Excitons“
Oktober 2001 – Februar 2007	Physikstudium an der Christian-Albrechts- Universität zu Kiel Abschluss: Diplom-Physiker (mit Auszeich- nung) Diplomvorprüfung (Note: sehr gut)
Thema der Diplomarbeit	Superfluidity of charged bosons (Note: sehr gut)
August 1991 – Juni 2000	Gymnasium Max-Planck-Schule in Kiel Abschluss: Allgemeine Hochschulreife (Note 1,8)
April 1993 – September 1993	Burbank Junior Highschool in Boulder, Colo- rado, USA

Zivildienst

Juli 2000 – Mai 2001	Werkstatt am Drachensee, Arbeiten und Wohnen für Behinderte
Aufgabenbereich	Einzelbetreuung beim Arbeiten

Berufserfahrung

Wissenschaftlicher Mitarbeiter

April 2007 – März 2011	Institut für Theoretische Physik und Astrophysik, Christian-Albrechts-Universität zu Kiel, AG Prof. Bonitz Forschungsvorhaben: s. Dissertation Finanzierung: DFG FI 1252/1-1
------------------------	--

Studentische Hilfskraft

2003 – 2006	Übungsgruppenleitung (5 Semester) Praktikumsbetreuung (2 Semester)
-------------	---

Praktika

Februar 2007 – März 2007	Schott Solar GmbH, Widerstandsmessungen an Frontkontakten von Solarzellen
--------------------------	--

Auszeichnungen

Juni 2005	Teilnahme an der Nobelpreisträgertagung in Lindau
März 2004	Nominierung für Stipendium der Studienstiftung des Deutschen Volkes
Juni 2000	DPG-Buchpreis für hervorragende Leistungen im Fach Physik

Danksagung

Der gegenseitige Austausch von Erfahrungen und Ergebnissen gehört zu den zentralen Aspekten des Forschens. Eine Arbeit wie diese entsteht niemals im leeren Raum.

An erster Stelle möchte ich mich bei Prof. Dr. Michael Bonitz bedanken, in dessen Arbeitsgruppe ich nun schon seit Ende 2006 tätig bin und der diese Arbeit damit überhaupt erst ermöglicht hat. Ohne seine Ideen und seine Kritik wäre das Forschungsprojekt niemals soweit gekommen.

Einen besonderer Dank möchte ich an Dr. Alexei Filinov richten, durch dessen Fachwissen und Betreuung die zentralen Ergebnisse dieser Arbeit entstanden sind. Ohne seine Expertise mit Pfad-Integral Monte-Carlo Simulationen wäre die Einarbeitung and Nutzung derselben sicherlich weitaus komplexer gewesen.

Hervorzuheben sind weiterhin Dr. Patrick Ludwig, David Hochstuhl, Torben Ott, Hanno Köhlert, Kenji Fujioka, Karsten Balzer, Sebastian Bauch, Lasse Rosenthal, Tim Schoof und Hauke Thomsen, die bei der Durchsicht der Arbeit geholfen haben.

Allen jetzigen und ehemaligen Mitgliedern der Arbeitsgruppe von Prof. Bonitz möchte ich herzlich für die lebhaften Diskussionen, aber auch die gemeinsamen Aktivitäten danken. Meine Zeit in der Arbeitsgruppe war sicher nie langweilig.

Des Weiteren möchte ich mich bei meinen Eltern bedanken, die mir mein Studium überhaupt erst ermöglichten.

Selbständigkeitserklärung

Hiermit versichere ich, dass ich die vorliegende Abhandlung – abgesehen von der Beratung durch den Betreuer – nach Inhalt und Form die eigene Arbeit ist.

Weiterhin versichere ich, dass die Arbeit unter Einhaltung der Regeln guter wissenschaftlicher Praxis der Deutschen Forschungsgemeinschaft entstanden ist.

Ich versichere, dass die vorliegende Arbeit weder ganz noch zum Teil schon einer anderen Stelle im Rahmen eines Prüfungsverfahrens vorgelegen hat, sowie in dieser Form weder veröffentlicht worden ist noch zur Veröffentlichung eingereicht wurde. Die in Rahmen der Arbeit entstandenen Publikationen in wissenschaftlichen Fachzeitschriften sind auf Seite 141 vermerkt.

Kiel,

